Cape Peninsula University of Technology

Performance of selected biomass solid catalysts for biodiesel production from vegetable oil in a continuous reactor system

By

MIRIAM JOCELINE LISBOA DE ALMEIDA

Dissertation submitted in fulfilment of the requirements for the degree

Master of Engineering: Chemical Engineering

In the Faculty of Engineering and Built Environment

At the Cape Peninsula University of Technology

Supervisor: Prof. Tunde Ojumu

Co-Supervisor: Prof. Oluwaseun Oyekola

Bellville

September 2021

DECLARATION

I, **Miriam Joceline Lisboa de Almeida**, declare that the contents of this dissertation/thesis represent my own unaided work, and that the dissertation/thesis has not previously been submitted for academic examination towards any qualification. Furthermore, it represents my own opinions and not necessarily those of the Cape Peninsula University of Technology.

Signed **Date**

ABSTRACT

The energy security issues and environmental concerns emerging from fossil fuel depletion and increased greenhouse gases emission have led to increased research towards alternative energy sources. Over the last two decades, the interest in biodiesel has grown significantly owing to its eco-friendly characteristic quality properties over fossil fuels. Biodiesel is a combination of mono-alkyl esters of lengthy-chain fatty acids. Biodiesel is viewed as a promising alternative fuel to petroleum diesel, because it exhibits similar properties to petro-diesel. Nonetheless, the cost of production of biodiesel is considerably higher than that of petro-diesel. To address the shortfalls of biodiesel production, the utilization of heterogeneous catalysts derived from biomass wastes represents a pathway. These catalysts have several advantages including renewability, high catalytic activity, non-toxicity, reusability, etc. This study is aimed at investigating the performance of selected solid base catalysts derived from biomass wastes for biodiesel production from vegetable oil in a designed continuous reactor system. The vegetable oil used in this study as feedstock source of triglyceride is waste sunflower oil (WSFO). The experimental approach in this study is divided into two phases. The phase 1 involved the synthesis of four selected biomass-derived solid base catalysts and the investigation of their performance in a batch reactor system for biodiesel production. The phase 2 involved developing an appropriate continuous reactor system to produce biodiesel and studying the kinetics of continuous biodiesel production using the best catalyst identified in phase 1 of the study. A batch reactor system was used for investigating the performance of the biomass-derived solid base catalysts (CBPA [Calcined Banana Peels Ash], CCESP [Calcined Chicken Eggshells Powder], CCPHA [Calcined Cocoa Pod Husks Ash] and CECPHA [Calcined Enterolobium Cyclocarpum Pod Husks Ash]). The set of operating reaction conditions used for the assays were as follows: 4 wt. % catalyst loading; 0.8 (v/v) methanol to oil ratio; 65 °C reaction temperature and 65 minutes reaction time. The best performance catalyst was found to be CECPHA (biodiesel yield= 77.90 wt. % ± 2.43). A supported catalyst was prepared having CECPHA as the active catalytic phase and pumice as the catalyst support. Upon impregnation, a significant reduction in surface area was observed in CECPHA. Nonetheless, the prepared CECPHA-Pumice catalyst was found to be effective in converting WSFO to WSFME (Waste Sunflower Methyl Esters) in the design packed bed reactor (PBR) at the chosen operating reaction conditions. The set of operating reaction conditions for the transesterifications in the PBR were as follows: 253 g catalyst amount corresponding to a catalytic bed height of 8.4 cm; 0.9 (v/v) methanol to oil ratio and 0.5 (w/w) co-solvent (n-hexane) to oil ratio. The continuous reactor system was used for studying the kinetics of the transesterification of WSFO (Waste Sunflower Oil) in the presence

of CECPHA-Pumice catalyst. Kinetic experiments to determine the initial rates of reaction were performed at the following volumetric feed flow rates 1.6 mL/min, 2.1 mL/min, 3 mL/min and 4 mL/min while the temperature was maintained constant at 55 °C. The highest conversion (77.90 %) was achieved at 1.6 mL/min feed flow rate. This feed flow rate was used to carry out experiments to estimate the model parameters [reaction rate constant (k), reaction equilibrium constant (K), methanol adsorption equilibrium constant (K_M) and glycerol adsorption equilibrium constant (K_G)] as well as the activation energy (E_a) which were investigated in the following temperatures 40 °C, 50 °C, 55 °C and 60 °C. The Arrhenius rate law of the reaction was expressed as $k = 0.149\ e^{-23.25/RT}$, where the activation energy (E_a) was found to be 23.25 kJ/mol. The regression coefficient (R^2) of the Arrhenius plot graph in this study was found to be 0.988, indicating that the experimental data fitted the Arrhenius model in the investigated temperatures. Overall the objectives of this study were accomplished. More insight into the kinetics of the transesterification of WSFO in a packed bed reactor in the presence of supported biomass-derived solid base catalyst was provided. The renewability, attractive catalytic qualities and relatively low cost of the supported biomass-derived solid base catalyst (CECPHA-Pumice) developed in this study and used in a continuous reactor arrangement demonstrate its potential for upscaling and possible commercialization.

ACKNOWLEDGEMENTS

Firstly, I would like to thank the Almighty God and King of my heart, my dear Lord and Saviour Jesus Christ, for the strength, perseverance, enlightenment, wisdom and knowledge, He has bestowed on me during this journey.

My utmost and heartfelt gratitude goes to Prof. Tunde Ojumu, who so brilliantly supervised me throughout the entire project, ensuring I would persist and achieve the desired outcome in this research.

My heartfelt appreciation goes to Prof. Oluwaseun Oyekola, who so wisely co-supervised me throughout the entire project, ensuring I would be attentive to details and thrive in the writing of this dissertation and achieve the desired outcome in this research.

To my parents, Venceslau de Almeida Sobrinho and Rosa de Almeida, I thank you for your words of motivation, encouragement and financial support. You made this journey much easier and enjoyable. I love you.

To my husband, Takunda Gwanzura, I thank you for your love, patience, motivation and support offered throughout the times.

To my brother, Mauro de Almeida, I thank you for the persistence you showed me in life professionally and academically, which was definitely an inspiration for me.

To my dearly beloved friend/sister Marinela Gomes, I thank you for your friendship, for all the prayers, encouraging and faith-filled words throughout this journey.

A special thank you goes to Ms Hannelene Small, who for various occasions went out of her way to ensure I was properly assisted and equipped with the necessary tools I needed to make progress in my laboratory work.

A special thank you goes to Dr Olushola Adeniyi for the academic insight and advice given at different occasions.

Last but not least, I would like to express my heartfelt gratefulness to Cape Peninsula University of Technology for providing the platform and resources for this project to come to fruition.

May God so lavishly bless you all.

DEDICATION

This dissertation is dedicated to my family, the Lisboa de Almeida family.

Table of Contents

LIST OF FIGURES

LIST OF TABLES

GLOSSARY

Acronyms/Abbreviations	Definition/Explanation
AOAC	Association of Official Analytical Chemists
API	American Petroleum Index
ASTM	American Society for Testing and Materials
BET	Brunauer−Emmett− Teller
BJH	Barrett-Joyner-Halenda
BP	Banana Peels
CBPA	Calcined Banana Peels Ash
CCESP	Calcined Chicken Eggshells Powder
CCPHA	Calcined Cocoa Pod Husks Ash
CECPHA	Calcined Enterolobium Cyclocarpum Pod Husks Ash
CES	Chicken Eggshells
CPH	Cocoa Pod Husks
CSTR	Continuous Stirred Tank Reactor
DG	Diglyceride
ECPH	Enterolobium Cyclocarpum Pod Husks
EDS	Energy Dispersive x-ray Spectroscopy
EN	European Standards
EWSFO	Esterified Waste Sunflower Oil
FA	Fatty Acid
FAAE	Fatty Acid Alkyl Esters
FAME	Fatty Acid Methyl Esters
FFA	Free Fatty Acids
FTIR	Fourier Transform Infrared spectroscopy
GC-FID	Gas Chromatography-Flame Ionization Detector

JCPDS	Joint Committee on Powder Diffraction Standards
MG	Monoglyceride
MeOH	Methanol
PBR	Packed Bed Reactor
PFR	Plug Flow Reactor
RPM	Rotation per minute
SEM	Scanning Electron Microscopy
TG(s)	Triacylglyceride (s), Triglyceride or Triacylglycerol
WSFME	Waste Sunflower Methyl Esters
WSFO	Waste Sunflower Oil
XRD	X-Ray Diffraction

PREFACE

Dissertation overview

This dissertation focuses on the design of a continuous reactor system for production of biodiesel from vegetable oil making use of heterogeneous catalysts derived from selected biomass materials. The outline of the dissertation chapters are reported herein.

- **Chapter 1: Introduction**

This chapter provides the background of the research, highlights the research problem statement, and clearly states the aim and specific objectives as well as the scope of the study.

- **Chapter 2: Literature Review**

This chapter reviews the existing literature related to the research topic. A brief outlook on the global energy consumption is provided and a more detailed look on the various feedstock sources for biodiesel production, reaction path in biodiesel production (with emphasis on transesterification mechanism), and the catalytic performance of some solid biomass catalysts is also given amongst other content.

- **Chapter 3: Materials and Methods**

This chapter describes the approach taken to achieve the specific objectives of the study and explains in detail the materials and procedures used in the study. The techniques for characterization of the WSFO, biomass derived solid base catalysts, biodiesel (WSFME); the kinetic experiments are also described.

- **Chapter 4: Results and Discussion of Biodiesel Production**

This chapter presents and discusses the results of the characterization of the selected biomass derived solid base catalysts as well as their performance in a batch reactor system. The results of the characterization of the prepared supported biomass derived solid base catalyst and the quality results of the biodiesel (WSFME) produced using this are also presented and discussed in this chapter.

- **Chapter 5: Kinetic Studies of Continuous Biodiesel Production**

This chapter presents in an organized manner an overview on kinetics of heterogeneous catalyzed transesterification reaction, and reviews the most applied reaction mechanisms for heterogeneous transesterification. The steps to derive the rate equation from the intrinsic kinetic model of the transesterification of WSFO with methanol using the synthesized supported biomass derived solid base catalyst as well as the relevant kinetic parameters are also presented in this chapter.

- **Chapter 6: Conclusion and Recommendations**

This chapter summarizes the overall conclusions and the main findings of this study as per the set objectives and reveals whether the specified objectives were accomplished. It also suggests recommendations for further investigation in light of the achieved results and challenges encountered.

CHAPTER 1
INTRODUCTION

1.1 Background

In recent years, there has been a growing need to explore unconventional energy sources that could serve as replacement to fossil fuels. This is due to the instabilities in the price of crude oil, the depletion in the reserves of fossil fuel, unabated ecological impacts of climatic changes specifically due to increased greenhouse gas emissions (Marinkovic et al., 2016; Xu et al., 2016). Owing to the aforementioned global concerns, biodiesel serves as a viable substitute to fossil fuels (Marinkovic et al., 2016). Biodiesel offers competitive advantages including being an environmentally friendly source of energy.

Biodiesel or chemically identified as fatty acid methyl esters (FAME) is a combination of mono-alkyl esters of long-chain fatty acids (Marinkovic et al., 2016). Biodiesel can be produced via a catalyzed or non-catalyzed reaction process known as transesterification (Abdullah et al., 2017). The reaction route includes starting feedstocks such as a biological resource containing triacylglycerols (TGs), which can be vegetable oils, animal fats, alga oils and microbes (Marinkovic et al., 2016; Abdullah et al., 2017).

There have been identified properties of biodiesel; renewability, lubricity, nontoxicity, and miscibility with petroleum diesel (Abdullah et al., 2017). Furthermore, biodiesel exhibits good oil characteristics such as low viscosity, high flash point, high cetane number, high combustion efficiency, and lower carbon monoxide emission as well as better emission profiles compared to traditional fossil based fuels (Xu et al., 2016; Abdullah et al., 2017). Despite its advantages, the production cost of biodiesel is still considerably elevated compared to the production cost of petro-diesel (Sani et al., 2014; Betiku et al., 2017).

To address one of the shortfalls associated with production of biodiesel; cost of feedstock, the use of waste or non-expensive feedstock, such as waste oil and non-edible oil, represent a pathway.

The commercial viability of biodiesel using various synthesis techniques has been reported in a previous study (Aransiola et al., 2014). For instance, there are several options to explore commercial viability of biodiesel. These include the utilization of low-grade feedstock (waste oils, animal grease and non-edible oils), feed combination optimization, integration of

processes, improvement of novel processes as well as the application of heterogeneous catalysts derived from natural resources and biomass wastes (Aransiola et al., 2014).

Biomass-derived catalysts offer numerous advantages including high catalytic activity, non-toxicity, reusability, renewability as well as the fact that they are more suitable for continuous mode operation, are easily separated from products and have lower capital and operating costs (Abdullah et al., 2017; Tang et al., 2018). In addition, they are stable under both acidic and basic conditions and have high water resilience properties, depending on the quantity and strength of active acid or basic sites (Abdullah et al., 2017). The application of these eco-friendly solid catalysts from biomass waste can act as a viable solution to overcome the challenges associated with homogeneous alkali-catalyzed biodiesel production as well as serve as a good substitute to the traditional heterogeneous catalyst of chemical origin (Tang et al., 2018).

1.2 Research Problem Statement

In the last decade, there has been an increase in the number of reported studies on the development of solid base catalysts for biodiesel production derived from biomass wastes such as eggshells, banana peels, and cocoa pod husks amongst other wastes as means to reduce overall biodiesel production costs. From literature studies, these type of biomass materials were proven to be both eco-friendly and cost-effective in deriving solid base catalysts which have been efficiently used to convert triglycerides from different vegetable oil sources to biodiesel, achieving yields up to 98%. Nonetheless in most of the reported literature, the assays of such biomass-derived solid base catalysts were conducted in batch reactors at laboratory scale. Therefore, it is essential to determine the effectiveness of some of these biomass-derived solid base catalysts for potential large-scale production by investigating their performance in a continuous reactor system with a view on commercial viability of biodiesel.

1.3 Aim and Objectives of study

The aim of this study is to investigate the performance of selected solid base catalysts derived from biomass wastes for biodiesel production from vegetable oil in a designed continuous reactor system.

The specific objectives of the study are as follows:

a) To synthesize and characterize physicochemical properties of the selected biomass-derived solid base catalysts.

b) To design a continuous reactor system appropriate for biodiesel production from vegetable oil.

c) To analyze the performance of the selected biomass-derived solid base catalysts under the same set of operating process conditions in a batch system with a view to identify the best catalyst.
d) To study the kinetics of the transesterification reaction in the designed continuous reactor using the best performance biomass-derived solid base catalyst.

1.4 Research Question

a) Which kinetic model appropriately defines the continuous transesterification of vegetable oil (WSFO) in the presence of biomass-derived solid base catalyst in this study?

1.5 Scope of Research

There are different processes that can be employed to produce biodiesel, however this study focuses solely on the catalyzed transesterification reactions of vegetable oil, specifically waste sunflower oil (WSFO), with methanol. Biomass solid base catalysts can be derived from a diverse range of biomass and biomass wastes, this study however focuses on four biomass wastes namely: banana peels, chicken eggshells, cocoa pod husks and enterolobium cyclocarpum pod husks.

This study does not cover the following:

- Determination of the variation of FFA content in waste sunflower oil during storage.
- Optimization and kinetics studies for the pre-treatment of WSFO (esterification process).
- Optimization and kinetic studies for the first phase of the experiments (batch system).
- Optimization of second phase of experiments (continuous system)
- Recycling of the glycerol (by-product).

CHAPTER 2
LITERATURE REVIEW

2.1 Introduction

The world's total energy demand is increasing owing to economic as well as population growth. The International Energy Outlook (IEO, 2016) has predicted that the global consumption of energy will increase between 2010 and 2040 by approximately 56%. IEO (2016) further highlighted that the total global energy consumption has increased annually at a rate of 1.52%. This is a relatively faster rate compared to the total population growth which has increased annually at a rate of 1.14% as reported by World Bank (n.d). Figure 2.1 illustrates the global total energy consumption from different sources.

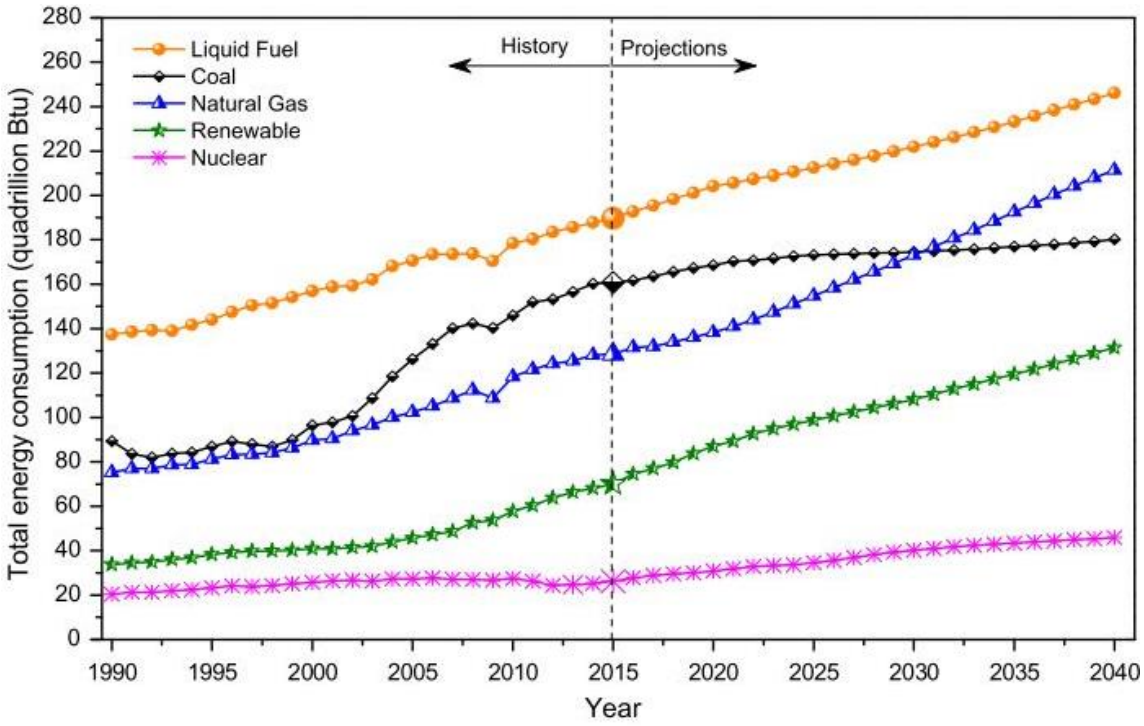

Figure 2.1: Global total energy consumption from various energy sources (IEO, 2016)

The vast majority of the global energy supply is generated by non-renewable sources, i.e. fossil-based fuels including petroleum, natural gas and coal (Patade et al., 2018). Literature studies have revealed that based on the current energy consumption of fossil fuel reserves, petroleum, natural gas and coal may keep going for a further 40, 70 and 200 years, correspondingly (Shafiee & Topal, 2009 ; Marwaha et al., 2018). Renewable sources account for over 13% of the global energy generated, with combustible renewables and renewable

municipal waste accounting for 10.6% and hydro, geothermal, solar, wind, tidal and wave sources accounting for the remainder (FAO, 2008).

Amongst the energy consuming sectors, the transportation sector consumes approximately 30% of the primary energy with its average global energy consumption rate increasing by 1.1% per year (Patade et al., 2018). This sector comprises of around 67% road transport, 23% shipping and 4% rail with the remainder in aviation transport (Azad et al., 2019). Furthermore, it has been predicted that the transport sector will have 63% portion in the step up of total global liquid fuel depletion from the year of 2010– 2040 (Mahmudul et al., 2017). The worldwide growth of the motorization industry has caused the rise in emission of harmful pollutants, which are vastly accountable for the air quality deterioration (Mahmudul et al., 2017; Patade et al., 2018).

Renewable and liquid ecofuel (biofuels) can serve as an alternative transport fuel to meet rising energy demands in the transport sector (Azad et al., 2019).The use of ecofuel involves bioethanol for light passenger vehicles worldwide and biodiesel for the road, rail, and marine (Azad et al., 2019). As of late, ecofuel has become an emerging market, including its utilization in the aviation sector as aviation biofuel (REN21, 2016). For instance, 10% of the total world energy is consumed by the aviation sector thus accounting for 2% of total CO_2 emissions globally as reported by Chiaramonti et al. (2014). The IEA (2018) has predicted that in 2023, the production of biofuels is expected to increase by 15% to 165 billion litres, which two-thirds of biofuel production growth is attributed to bioethanol while the remainder is attributed to biodiesel and hydro treated vegetable oil (HVO). Furthermore, biofuels are expected to hold a share in the transport sector of almost 90% of the total renewables in 2023 as predicted by IEA (2018).

2.2 Brief biodiesel history

The diesel engine was developed in 1893 by famous German engineer Dr. Rudolph Diesel (1858-1913) (Demirbas, 2008). From the start, the diesel engine had a benefit over its petrol counterpart in that it could be powered by fuels derived from various sources, including vegetable oil (Knothe, 2016). In fact, the first record of a diesel engine powered by vegetable oil, specifically peanut oil, was exhibited at the Paris World Exposition of 1900 (Demirbas, 2008; Knothe, 2016).

Owing to the widespread accessibility and low petroleum diesel fuel cost, vegetable oil-based fuels gained little interest (Pacific Biodiesel, 2019). World War II and the 1970s energy crises,

then rekindled transient interest in alternative fuels, among them vegetable oil-based fuels (Knothe, 2016). However, vegetables oils could not be directly used to power the new diesel engine designs due to their viscosity being much higher than the viscosity of petroleum diesel fuels (Pacific Biodiesel, 2019). Thus, it became imperative to find a way to effectively reduce the viscosity of vegetable oils so they could be suitably utilized as fuels to run the new diesel engine. Different techniques have been recommended to accomplish this task, including vegetable oil blending with solvents, pyrolysis and even emulsification of the vegetable oils with alcohols or water, none of which have served as an appropriate solution (Pacific Biodiesel, 2019). It was in 1937 that a Belgian inventor by the name Charles George Chavanne firstly proposed a process, nowadays known as transesterification, to extract ethyl ester from palm oil and used the product as a replacement for diesel fuel (Pacific Biodiesel, 2019; Rental center crete, n.d). The product created from the process developed by Chavanne was closely akin to modern biodiesel (Pacific Biodiesel, 2019; Rental center crete, n.d).

In the early 1990s, innovative work in Europe and South Africa by scientists such as Martin Mittelbach contributed to the expansion of the biodiesel industry, with U.S market for biodiesel growing much slower at the time (Rental center crete, n.d). By mid to late 1990s, a number of legislative and regulatory incentives in several countries worldwide helped bringing biodiesel to the market, accelerating a couple of years later (Demirbas, 2008; Pacific Biodiesel, 2019). Nowadays, for the most part biodiesel is used in blends with petro-diesel (Knothe, 2016). These blends often being termed “BXX”, in which “XX’ symbolizes the percentage level of biodiesel blended with the petro-diesel (Knothe, 2016). The successful commercialization of biodiesel in different nations worldwide has been complemented by the implementation of standards to guarantee a product of high quality and instil consumer confidence (Knothe, 2016).

2.3 Reaction path in biodiesel production

There are three well-known techniques for producing biodiesel that have been studied by Ma and Hanna (1999), viz. micro-emulsion, thermal cracking and transesterification. The transesterification being the most common and preferred method for biodiesel production will be discussed in detail.

2.3.1 Biodiesel production via transesterification reaction

Transesterification, is defined as a catalyzed or non-catalyzed chemical reaction between a triglyceride and an alcohol resulting in the formation of fatty acid alkyl esters (FAAE), i.e. biodiesel, and glycerol (Wang et al., 2007; Aransiola et al., 2014; Marinkovic et al., 2016). In the case of the catalyzed transesterification reaction, the use of primary or secondary monohydric aliphatic alcohols having 1-8 carbon atoms is recommended as these types of alcohols facilitate the reaction (Aransiola et al., 2014). The transesterification reaction is represented by three control stages: mass transfer, kinetic and equilibrium controlled (Musa, 2016). The mass transfer stage is the slowest one due to immiscibility of triglycerides and methanol (Musa, 2016).

During the transesterification of triglycerides to FAAE, three reversible reactions occur sequentially and one mole of ester is released at each step (Eckey, 1956). The triglycerides, which are esters of long-chain carboxylic acids linked to a glycerol molecule, are transformed stepwise to diglycerides (intermediate product) and lastly to monoglycerides and glycerol as the final products (Ma & Hanna, 1999; Demirbas, 2009). The stoichiometric alcohol to oil molar ratio is 3:1. In order to shift the reaction equilibrium forward to yield more methyl esters as the desired product, the equilibrium reaction requires huge amounts of alcohol (Aransiola et al., 2014; Baskar & Aiswarya, 2016). Figure 2.2 represents the transesterification reaction mechanism.

(a)

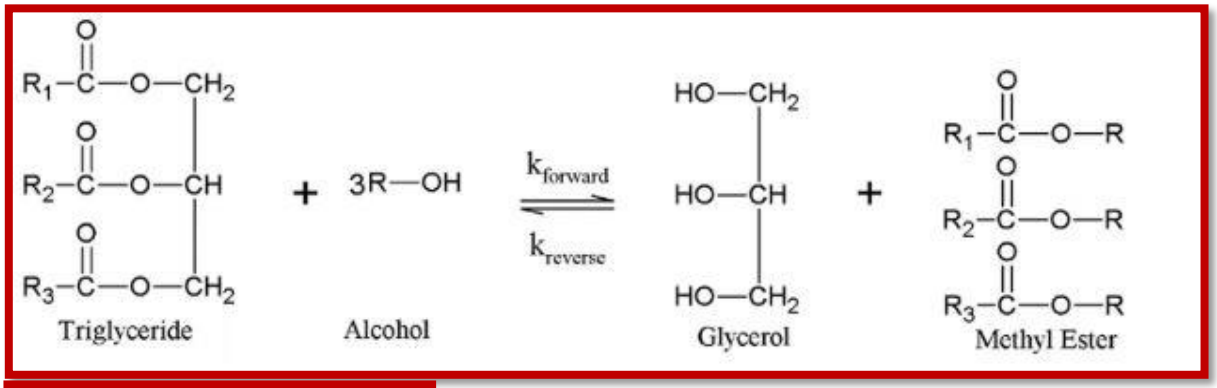

k- Reaction rate constant

(b)

Step 1

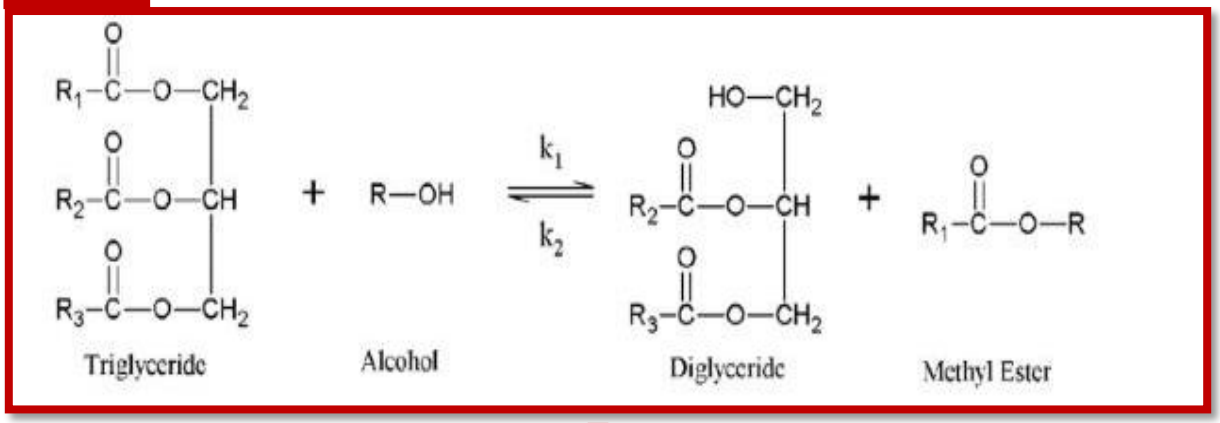

Step 2

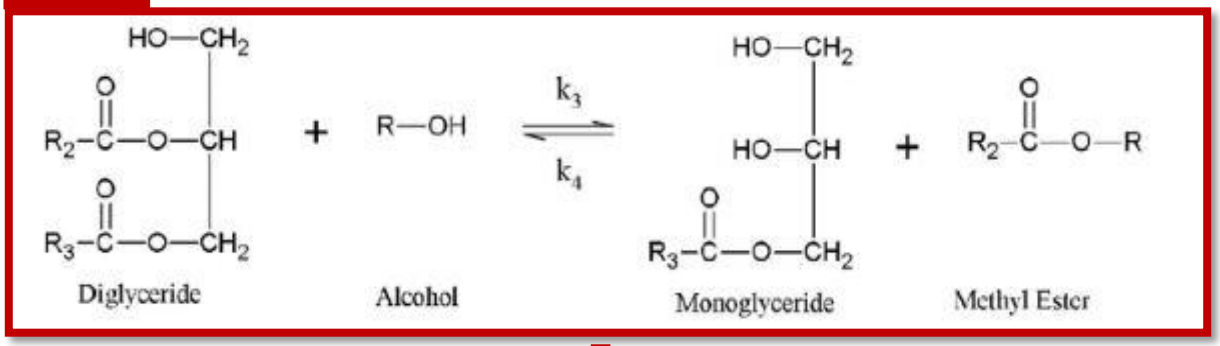

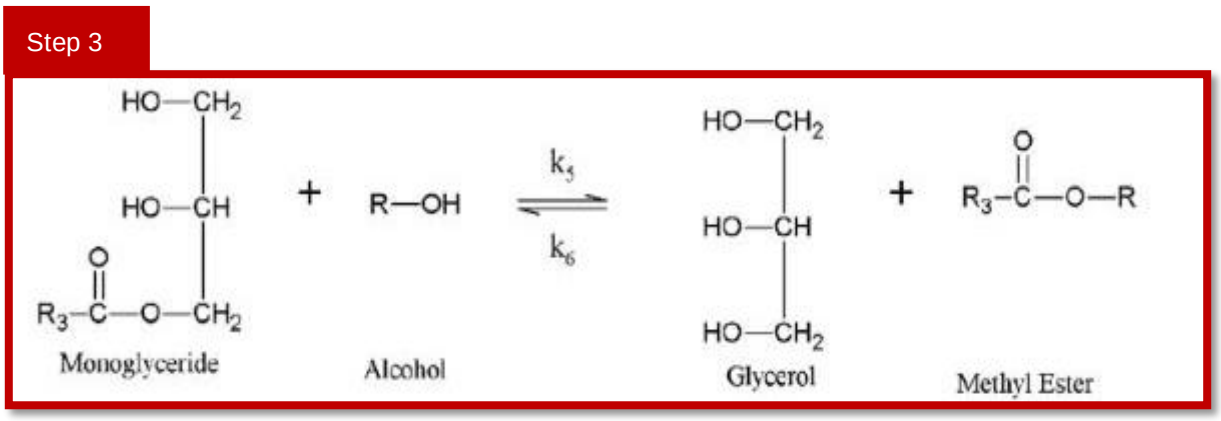

Figure 2.2: Transesterification reaction path (a) overall reaction and (b) step by step reaction (Tang et al., 2018)

2.3.2 Reaction parameters affecting the yield of biodiesel

The key parameters affecting the transesterification reaction are alcohol to oil molar ratio, reaction temperature and pressure, reaction time, catalyst type and content, water content and free fatty acid (FFA) content (Demirbas et al., 2016).

2.3.2.1 Alcohol to oil molar ratio

The alcohol to oil molar ratio is one of the most significant variables affecting the yield of alkyl esters (Demirbas et al., 2016). The transesterification reaction is reversible thus, higher molar ratios are required to enhance the solubility and to increase the contact between the triglyceride and alcohol molecules (Noureddini et al., 1998; Ma & Hanna, 1999; Musa, 2016). In addition, the higher molar ratios of alcohol/oil during transesterification reaction result in higher purity, greater conversion and shorter reaction time to yield alkyl ester (Ma & Hanna, 1999; Musa, 2016). An alcohol to oil molar ratio range of 6:1 – 40:1 is often used for the transesterification of vegetable oils under catalytic and supercritical alcohol conditions (Demirbas, 2006).

For an alkali-catalyzed transesterification, the optimum molar ratio of methanol to oil is approximately 6:1 (Musa, 2016). This molar ratio produces a biodiesel yield of more than 98% (w/w) (Musa, 2016). A methanol to oil molar ratio of 6:1 is employed so that there is sufficient alcohol to break the fatty acid-glycerol bonds (Ma & Hanna, 1999). Molar ratios greater than 6:1 do not increase the ester yield, but instead could hinder the separation process (Musa, 2016).

For an acid-catalyzed transesterification, considerably high alcohol/oil molar ratios are required to achieve products with good yield within reasonable reaction times (Musa, 2016). However, the yield of esters do not proportionately increase with an increase in alcohol/oil molar ratio (Demirbas et al., 2016). An alcohol/oil molar ratio of 6:1 during acid transesterification and 9:1 molar ratio during alkali transesterification were reported by Ramadhas et al. (2004) and Sahoo et al. (2007) to be the optimal molar ratios for biodiesel produced from high FFA content rubber seed oil and polanga seed oil respectively.

2.3.2.2 Reaction temperature and reaction time

Transesterification reaction can take place at various temperatures depending on the type of oil used (Demirbas et al., 2016). In the alkali-transesterification process, the reaction temperature during different steps ranges between 318 and 338 K (Demirbas et al., 2016). Raising the temperature to supercritical condition has been reported to have a positive effect on the yield of methyl esters (Demirbas et al., 2016). On the contrary, raising the reaction temperature above 323 K has been reported to have a negative effect on the yield of methyl esters from neat oil, but a positive effect when waste oils with higher viscosities were used (Leung & Guo, 2006).

Vyas et al. (2011) reported an optimal yield of methyl esters of 93.5 wt. % obtained at a temperature of 323 K and at 45 min of reaction time, when studying the effect of these two parameters on the conversion of Jatropha curcas oil. The conversion rate of methyl esters increases with the reaction time as stated by Ma and Hanna (1999). Different reaction times for the transesterification reaction have been reported (Demirbas et al., 2016). Freedman et al. (1984) investigated the transesterification reaction of four oils namely peanut, cotton-seed, sunflower and soybean oils under the following conditions: methanol to oil ratio of 6:1, 0.5% sodium methoxide catalyst and 60°C. A yield of approximately 80% was achieved just after 1 min for soybean and sunflower oils. After 1 hour, the conversions were nearly the same for all four oils approximately 93±98%.

2.3.2.3 Water and Free fatty acid (FFA) contents

Water and FFA contents are principal parameters for deciding the viability of the vegetable oil transesterification process (Demirbas et al., 2016). The mandatory requirement of feedstock for alkali-transesterification of glycerides have been pre-determined from various studies (Wright et al., 1944; Canakci & Van Gerpen, 1999; Ma & Hanna, 1999). For instance, the FFA content of vegetable oil must be less than 1% and all raw materials must be considerably anhydrous (Ma & Hanna, 1999). If FFA content is greater than 1%, more alkali catalyst (NaOH or KOH) is required to neutralize the FFAs (Ma & Hanna, 1999). FFAs react with the alkaline catalyst to yield soaps that hinder the separation of the ester, glycerine, and wash water (Canakcı & Van Gerpen, 1999). Moreover FFAs may speed up the alkali catalyst deactivation (Borges & Díaz, 2012)

Water content is a significant factor in the traditional catalytic transesterification of vegetable oil (Ma & Hanna, 1999). Water can cause formation of soap, gels and froths which can result in increased viscosity and hinder product separation (Ma & Hanna, 1999). Moreover the presence of water consumes the catalyst and decreases its efficiency resulting in a low conversion in biodiesel production (Ghadge & Raheman, 2005). Thus the presence of FFAs and water always produce negative effects when dealing with alkaline catalysts (Demirbas et al., 2016).

The effects of free fatty acids and water on the transesterification of beef tallow catalyzed by NaOH with methanol were investigated (Ma et al., 1998). The water content and FFA content of beef tallow must be below 0.06% (w/w) and 0.5% (w/w) respectively (Ma et al., 1998). However, in relation to the study of Madras et al. (2004), the presence of water had an insignificant impact on the conversion of triglycerides to biodiesel while utilizing lipase as a catalyst.

2.3.2.4 Catalyst content and type

Several studies have investigated the effects of catalyst content and type in transesterification of triglycerides (Ma & Hanna, 1998; May, 2004; Stavarache et al., 2005; Meneghetti et al., 2006). Catalysts used for the transesterification of triglycerides are categorised as alkali, acid and enzyme catalysts (Ma & Hanna, 1999). In general, catalysts are favourable to other associated parameters to increase the yield of alkyl esters (biodiesel). For instance, alkali-based catalysts have been used at room temperature compared to acid-based catalysts used

at higher temperatures (Meneghetti et al., 2006). The yield of alkyl esters using alkali catalysts have been reported to range between 68.9 wt. % and 71.2 wt.% for KOH and NaOH respectively (Hossain & Mazen, 2010). Also, the concentration of catalyst at 1.0% as in the case of NaOH was reported to produce the highest yield compared to 0.5% and 1.5% concentrations of NaOH (Hossain & Mazen, 2010).

2.4 Sources of feedstock for biodiesel production

The direct utilization of vegetable oils and its blends as fuel in diesel motors had been viewed as unsustainable, because of their inherent characteristics such as high viscosity, high FFA content, acid composition and gum development (Aransiola et al., 2014). The gum development occurs as a result of oxidation and polymerization during combustion and storage (Aransiola et al., 2014). Two of the more evident issues with using vegetable oils and its blends directly as fuels in diesel engines are the thickening of the lubricating oil and the carbon deposits (Aransiola et al., 2014). Due to these problems, efforts have been made to transform these vegetable oils to appropriate and sustainable biodiesel fuels.

2.4.1 Categories of feedstock sources

A wide range of feedstocks have been studied for producing biodiesel and can be classified into different categories, namely: edible oils, non-edible oils, waste oils, animal fats, and algal lipids (Avhad & Marchetti, 2015). Table 2.1 illustrates, the distinctive types of plant oils, animal fats, and other sources utilized for biodiesel production.

Table 2.1: Example of feedstocks used for biodiesel production (Avhad & Marchetti, 2015)

Edible Oils	Non-edible oils	Animal fats	Other resources
Coconut	Castor	Beef tallow	Algae
Corn	Cottonseed	Chicken fats	Cooking oil
Hemp seed	Desert date	Fish fats	Pomace oil
Mustard seed	Jatropha	Porklard	Soapstocks
Olive	Jojoba	Waste salmon	Tail oil
Palm	Karanja		
Peanut	Linseed		
Pumpkin seed	Mahua		
Rapeseed	Moringa		
Rice bran	Neem		
Safflower seed	Polonga		
Sesame seed	Rubber seed		
Soybean	Tobacco seed		
Sunflower	Tung		
Canola			

2.4.1.1 Edible oils

In the last few decades the demand for edible plant oils has increased drastically for two main industrial reasons: food, and their use as a biodiesel feedstock (Avhad & Marchetti, 2015).

Edible oils , also known as first generation oils, are usually obtained from vegetable oils such as soybean oil, corn oil, sunflower oil, olive oil, palm oil, coconut oil, rapeseed oil, mustard oil, castor oil and food crops like rice, wheat, potato wastes, sugarcane, etc (Verma et al., 2016). These oils are commonly used for biodiesel production in countries like U.S.A, Brazil, Argentina, Malaysia, Indonesia and some Europe (Avhad & Marchetti, 2015).

Currently about 95% of the world total biodiesel is produced from approximately 84% rapeseed oil, 13% sunflower oil, and 3% palm oil (Avhad & Marchetti, 2015). However, in the long run the use of these oils for biodiesel production may lead to socio-economic and environmental implication of biodiesel feedstock such as rise in the food prices, increase starvation, deforestation, and use of arable land for cultivating only oil-bearing plants, which makes these oils unlikely to be sustainable (Avhad & Marchetti, 2015; Verma et al., 2016).

2.4.1.2 Non-edible oils

Non-edible vegetable oils are those oils that are not suitable for human ingestion as they contain some toxic components in their composition (Atabani et al., 2013)**.** The examples of non-edible oils include jatropha seed oil, karanja oil, castor oil, jojoba oil, mahua oil, linseed oil, cottonseed oil, amongst others (Avhad & Marchetti, 2015; Mardhiah et al., 2017).

In recent years, the potential of non-edible oils as feedstock for biodiesel production has been explored (Atabani et al., 2013). For instance, non-edible oils exhibit advantages such as high oil content, easy availability, adaptability to arid and semi-arid conditions and lower cost of cultivation compared to edible oils (Avhad & Marchetti, 2015). In addition, non-edible oil crops could be grown in empty territories or in lands not suitable for agriculture. Also, since these plant oils do not compete with the food industry, the remaining seed cake after oil extraction may be used as fertilizers for soil enhancement (Atabani et al., 2013; Avhad & Marchetti, 2015). Therefore, non-edible oils should be regarded as sustainable feedstocks for biodiesel production as well as other alternative fuels as these oils can overcome the problems of food vs. fuel, environmental and economic issues associated with edible vegetable oils (Atabani et al., 2013)**.**

2.4.1.3 Other feedstock sources

Other feedstock sources that can be used to produce biodiesel include waste cooking oil, fish oil, microalgae biomass (spirulina platensis algae, etc.), animal fats amongst others (Verma et al., 2016).

Waste cooking oil (WCO) is defined as the leftover oil obtained after cooking, this oil is often disposed of with no further application (Avhad & Marchetti, 2015). Over the last few years, waste cooking oil has been proposed as an environmentally benign and low cost feedstock for biodiesel production (Gan et al., 2010). However, WCO is very impure comprising mostly of high FFA, which constitute about 0.5-15% of its content (Anuar & Abdullah, 2016). WCO can be divided in two groups in light of its FFA content: the yellow grease (FFA<15%), and the brown grease (FFA>15%) (Anuar & Abdullah, 2016). An oil with a low FFA content, i.e. no more than 1%, is a pre-requisite for an alkali-catalyzed transesterification to take place successfully and avoid soap formation which impedes the final separation process of FAME from glycerol and reduces the yield of FAME (Patil et al., 2010). Thus, prior to using WCO in the transesterification reaction it is necessary to encompass filtration and purification processes to make it suitable for biodiesel production (Patil et al., 2010; Avhad & Marchetti, 2015).

Animal fats constitute another unconventional feedstock for biodiesel production. The examples of animal fats which have been investigated as feedstock for biodiesel production include chicken fat, fish fats, beef tallow, duck tallow amongst others (Avhad & Marchetti, 2015). Animal fats produce biodiesel fuels with high cetane number (Verma et al., 2016). However, the fuel derived from animal fat tend to be less resistant to oxidation due to the absence of natural antioxidants (Verma et al., 2016). In addition, the fuel derived from animal fat has high cold filter plugging point because of the substantial content of saturated fatty acids present in fats (Avhad & Marchetti, 2015).

Microalgae exhibit some prominent advantages over other biodiesel feedstocks such as renewability and eco-friendliness, low cost culturing, rapid growth, adaptability to different environment, i.e. land and water (saline or brackish water) (Raslavičius et al., 2014; Verma et al.,2016). In addition, microalgae have the best yield to give oil per unit area of land compared to other traditional feedstocks (Verma et al., 2016). One of the requirements for efficient conversion and economical use of microalgae is a high level of biomass content (Verma et al., 2016). The most commonly used indicator of algal biomass is phytoplankton chlorophyll a

concentration. The lipids proportion in microalgae constitutes essentially more than 30% of its total content (Verma et al., 2016).

2.4.2 Composition of feedstock sources

All vegetable oils and animal fats are predominantly composed of triglycerides (Johnson et al., 2009). Triglycerides encompass in their molecule, three fatty acid chains (acyl group) that are attached to a glycerol backbone (glycerol group), when they are not attached to other molecules they are called free fatty acids (FFAs) (Johnson et al., 2009). The structures of the triglyceride molecule and fatty acids in their free state, are shown in Figure 2.3(a) and (b) respectively.

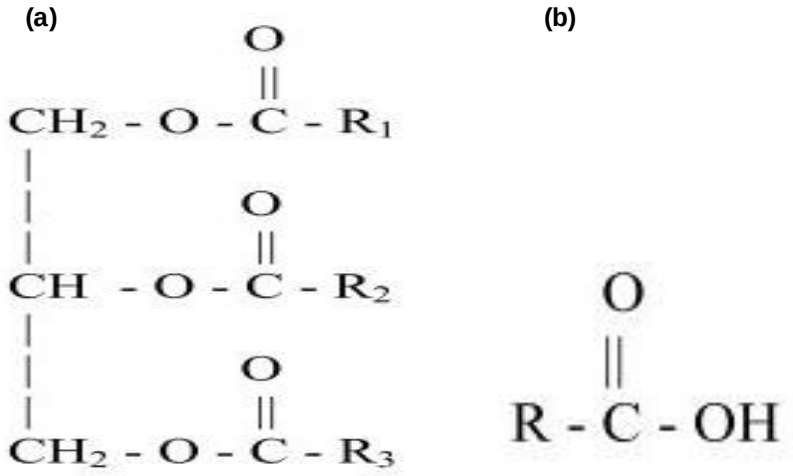

Figure 2.3: (a) Triglyceride molecule and (b) Fatty acid in free form (Gerpen et al., 2004)

Where the hydrocarbon chains of the fatty alkyl groups of the triglyceride are represented by R1, R2, and R3. A hydrocarbon chain ≥10 carbon atoms is represented by R (Gerpen et al., 2004).

Fatty acids (FAs) are hydrocarbon chains of different lengths and degrees of unsaturation that end with carboxylic acid groups (Berg et al., 2002). The length of the carbon chains generally falls in the range of 10 – 24 carbons (Berg et al., 2002). FAs may be categorized into saturated fatty acids (SFAs) or unsaturated fatty acids (USFAs) based on the nature of carbon-to-carbon bonds (Selvan & Nagarajan, 2013). SFAs are carboxylic acids which have between 12 to 24 single carbon-to-carbon bonds along its chain and are chemically less reactive (Selvan & Nagarajan, 2013). On the contrary, USFAs, can either have at least one carbon-to-carbon double bond along its chain and be known as monounsaturated fatty acids (MUFAs) or have multiple carbon-to-carbon double bonds along its chain and be known as polyunsaturated fatty

acids (PUFAs) (Selvan & Nagarajan, 2013). The more the number of double bonds a PUFA has the more chemically reactive it is. USFAs exist in a cis-configuration as well as in a trans-configuration. Most cis-configurations are present in most of the naturally occurring USFAs, whereas the trans-configuration is caused by hydrogenation and other technical methods (Johnson et al., 2009; Selvan & Nagarajan, 2013).

The type of fatty acids that makes up the triacylglycerol molecule is the significant factor between the various types of oils and fats. The fatty acid profile of a specific oil sample is defined as the quantity of the different FAs present in the sample. It can be used to predict physical properties and performance of the biodiesel product (Berg et al., 2002).

The fatty acids are commonly denoted by notations such as C16:0 or C18:2 for example, which indicate that the acid is composed of a 16 carbon chain with 0 double bonds for C16:0, whereas for C18:2 signifies that the acid is composed of a 18 carbon chain with 2 double bonds present (Selvan & Nagarajan, 2013).The first example is a SFA and the second one is a PUFA. Table 2.2 shows the common names of the fatty acids.

Table 2.2: Common names of FAs (Gerpen et al., 2004)

Fatty acid formula	Fatty acid name
C14:0	Myristic Acid (tetradecanoic acid)
C 16:0	Palmitic (hexadecanoic acid)
C18:0	Stearic Acid (octadecanoic acid)
C18:1	Oleic Acid
C18:2	Linoleic Acid
C18:3	Linolenic Acid
C20:0	Arachidic Acid (eicosanoic acid)
C22:1	Erucic Acid

2.4.3 Pre-treatment of high FFA feedstock for biodiesel (via esterification process)

An alkali-catalyzed transesterification is the preferred catalytic route for biodiesel production because it is able to achieve high purity and high yield biodiesel in a short time (30–60 min) (Wang et al., 2007). However, alkali-catalyzed transesterification is extremely sensitive to the purity of the oil (Wang et al., 2007). Alkali catalysts have been found to be inefficient for conversion of oils containing high FFA content (Aransiola et al., 2014; Ambat et al., 2018). Merely vegetable oils with FFA levels ranging from 0.5 wt. % to less than 3 wt. % of the oil can be used as feedstock in the alkali-transesterification process (Aransiola et al., 2014). Therefore, a two-step catalysis technique has been proposed to deal with high FFA feedstock for biodiesel production (Gan et al., 2010).

The two-step catalysis method consists of the acid-catalyzed esterification of the FFAs to FAME, which is carried out to lower the FFA level in the oil, followed by the alkali-catalyzed transesterification of oil to produce high yield FAME (Gan et al., 2010; Aransiola et al., 2014). In the first step of the two-step catalysis method, sulfuric acid is commonly employed due to its low cost and high conversion (Wang et al., 2007). However, there are some drawbacks associated with using sulfuric acid such as effluent disposal, loss of catalyst, high cost of equipment due to the corrosive nature of the acid (Gan et al., 2010). To overcome these drawbacks, investigations on other solid acid catalysts for the esterification process have been conducted (Wang et al., 2006; Wang et al., 2007; Gan et al., 2010). Ferric sulfate [$Fe_2(SO_4)_3$] has been proposed as a great substitute for sulfuric acid (Wang et al., 2007). In fact, ferric sulfate was found to have much higher catalytic activity compared to sulfuric acid, with maximum FFA conversion of 97.22% under the following conditions: methanol to oil ratio of 10:1, 2 wt.% catalyst loading, reaction temperature and reaction time of 95 °C for 4 h respectively (Gan et al., 2010). In another study, ferric sulfate was found to be an effective and reusable catalyst for reducing FFA content in many oils (Betiku et al., 2017).

Figure 2.4 illustrates the two step catalyzed transesterification reaction for biodiesel production. In both steps methanol is the alcohol of choice.

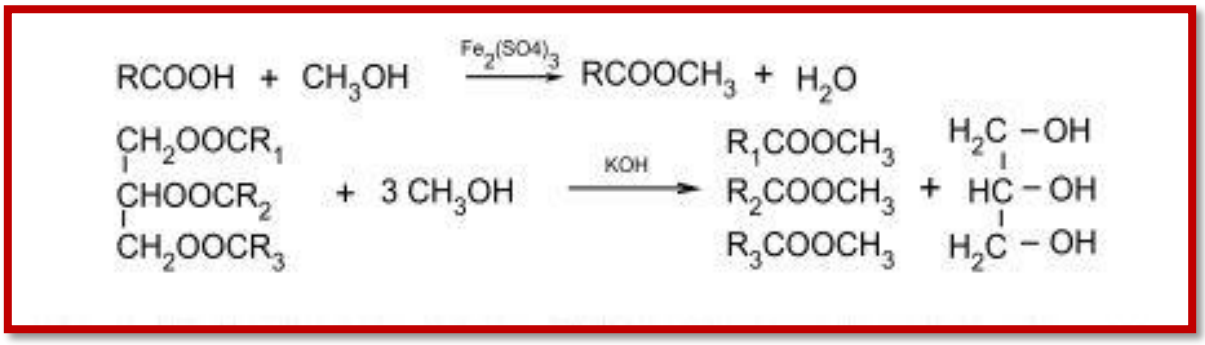

Figure 2.4: Two step catalyzed process for biodiesel production (Wang et al., 2007)

2.5 Choice of alcohol

The choice of methanol used in transesterification reaction has been attributed to several factors. These factors include: its considerably cheaper cost, availability, easier recovery of unreacted alcohol and better performance compared to other alcohols (Wang et al., 2006; Wang et al., 2007; Refaat & Refaat, 2010; Aransiola et al., 2014; Verma et al., 2016). However, since methanol is derived from fossil resources, the biodiesel produced via methanolysis cannot be considered fully renewable (Verma et al., 2016). In contrast, ethanol is less harmful

to the environment and renewable as it can be derived from agricultural products thus making it independent from fossil resources (Refaat & Refaat, 2010; Aransiola et al., 2014). Other advantages of ethanol over methanol include high heat content and cetane number. This is due to the extra carbon atom in the ethanol molecule, and the lower cloud and pour points that ethyl esters have compared to methyl esters (Refaat & Refaat, 2010).

However, ethanol has some drawbacks compared to methanol such as its slower reaction rate, complex ethyl ester formation (in the case of base-catalyzed transesterification) and the formation of stable emulsions (Refaat & Refaat, 2010). The presence of stable emulsions makes the separation and purification of esters more complicated (Refaat & Refaat, 2010).

There has been a suggestion on the need to ensure bio-based resources for biodiesel synthesis including alcohol feedstock (Verma et al., 2016). Besides ethanol, butanol and pentanol are examples of alcohols that can be derived from bio-based resources (Verma et al., 2016).

Despite the differences in the reaction kinetics when using different alcohols for the transesterification reaction, the resultant yield of esters remains more or less unaffected. Thus, making the selection of the alcohol based on cost and performance considerations (Refaat & Refaat, 2010).

2.6 Catalysts for biodiesel production

The catalysts used to produce biodiesel can be categorized into three main types namely: homogeneous catalysts, heterogeneous catalysts and biocatalysts (enzymes). The first two will be discussed in more detail. Figure 2.5 shows a breakdown of the existent type of catalysts.

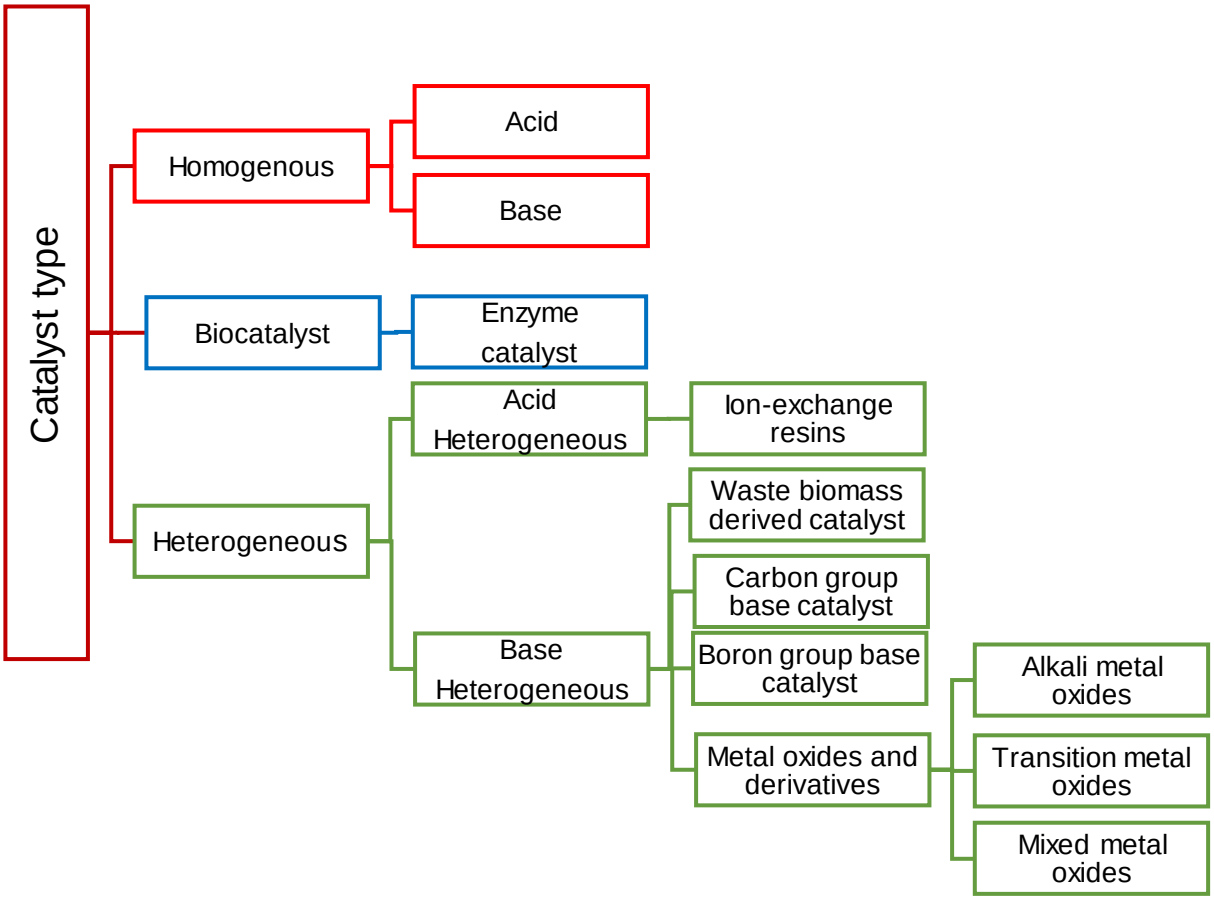

Figure 2.5: Breakdown of catalyst type (Chouhan & Sarma, 2011)

2.6.1 Homogeneous catalyzed transesterification

Homogeneous catalysts are in the same phase as the reaction medium (often liquid) and they are essentially acid and alkali catalysts (Aransiola et al., 2014). The homogeneous alkali catalysis is the most used method in the transesterification of triglycerides (TAGs) with methanol to yield FAME (Son & Kusakabe, 2011). Due to its acceptable reaction rates and product yields which can be achieved at temperatures lower than the boiling point of methanol and at normal pressure. Thus, decreasing the capital and operating costs associated with the production of biodiesel (Son & Kusakabe, 2011).

The homogeneous catalysts have major drawbacks such as equipment corrosion and a complex separation of the catalyst from the product (Marinkovic et al., 2016). These catalysts cannot be re-used nor regenerated (Son & Kusakabe, 2011). In the case of homogeneous alkali-catalyzed transesterification, purification steps of the crude biodiesel are required in order to meet biodiesel standard specifications for commercial use (Marinkovic et al., 2016). In addition, during the purification steps huge quantities of wastewater are generated. This

wastewater needs to be pre-treated before it can be discharged (Marinkovic et al., 2016). All these drawbacks result in increased production costs (Son & Kusakabe, 2011; Marinkovic et al., 2016).

2.6.2 Heterogeneous catalyzed transesterification

Heterogeneous catalysts are in a different phase as the reaction medium (often solid form) and these can have either acidic or basic characteristics or both of them (Aransiola et al., 2014; Mardhiah et al., 2017). Based on catalytic temperature, heterogeneous catalysts can be classified into two categories: high temperature catalysts and low temperature catalysts (Aransiola et al., 2014).

The use of solid catalysts in the transesterification of triglyceride has become an attractive route for biodiesel production as these can overcome certain problems associated with homogeneous catalysts (Buasri et al., 2012; Aransiola et al., 2014). Some of the advantages of solid catalysts include simple and cost-effective separation and purification steps, easy reusability and prolonged lifespan (Buasri et al., 2012; Mardhiah et al., 2017). Solid catalysts can be regenerated and they can also be manipulated to include desired catalyst properties such that the presence of FFAs or water does not interfere with transesterification reaction steps (Aransiola et al., 2014).

The main drawbacks reported for heterogeneous catalysts are the mass transfer limitations as these catalyst tend to form three phases with oil and alcohol decreasing the rate of reaction (Baskar & Aiswarya, 2016). This limitation can be resolved by using co-solvent such as n-hexane, tetrahydrofuran and ethanol, which improves the miscibility of oil and solvent (Baskar & Aiswarya, 2016). Another common issue associated with solid catalysts is their deactivation overtime due to different reasons such as poisoning, leaching and coking (Ullah et al., 2016). Thus, the development of heterogeneous catalysts with better stability, selectivity, activity at a low reaction temperature and pressure is essential (Baskar & Aiswarya, 2016; Ullah et al., 2016).

2.6.2.1 Biomass wastes for heterogeneous (solid) base catalyst development

The potential of biomass ashes as solid base catalysts for biodiesel production has been investigated in several studies (Chakraborty et al., 2010; Witoon, 2011; Buasri et al., 2013; Ahmad et al., 2015; Tan et al., 2015; Betiku et al., 2016; Falowo et al., 2019). The most common method used to prepare biomass-derived solid base catalysts is the calcination process (Abdullah et al., 2017). Calcination involves thermal treatment in the absence of air and oxygen in order to break down or decompose a compound into a smaller component (Abdullah et al., 2017). Depending on the type of biomass waste used, calcination can be performed at a wide temperature range from 300 to 1000 °C (Abdullah et al., 2017). For the purpose of this study, selected biomass wastes will be reviewed for solid base catalyst development.

2.6.2.1.1 Banana Peels (BP)

Banana is one of the major constituents of the principal food resources and the second largest produced fruit after citrus in the world (Betiku et al., 2016). It is among the world's most substantial foodstuffs after milk, rice and corn (Sharma & Mishra, 2015). From such vast production of the fruit, arise concerns regarding the waste disposal of its peels (Betiku et al., 2016).

Although banana peel is a fruit left-over, it constitutes 30-40% of the total fruit weight and consists of carbohydrates, proteins, fat and fiber in significant amounts (Sharma & Mishra, 2015). The banana peels also comprise of potassium and sodium oxides which when dissolved in water form the equivalent hydroxides (Gohain et al., 2017). They have also been utilized as sole source of carbon for producing citric acid and been investigated as biosorbent for removal of cadmium and other metals from wastewater (Betiku et al., 2016; Gohain et al., 2017).

Banana peels (Musa "Gross Michel") ash has been used as solid base catalyst in the transesterification of Bauhinia monandra seed oil (Betiku et al., 2016). An optimal biodiesel yield of 98.5 ± 0.18 wt. % has been reported by Betiku et al. (2016) under the following operating conditions: catalyst loading of 2.75 wt. % of oil, methanol/oil molar ratio of 7.6:1, reaction temperature of 65 °C and reaction time of 69.02 min. Gohain et al. (2017) reported a conversion of waste cooking oil of 100% when banana peels (Musa balbisiana Colla) ash was solid base catalyst. The reported optimum operating conditions were as follows: catalyst loading of 2 wt. %, methanol to oil ratio of 6:1, reaction temperature of 60 °C and reaction time of 3 hours (Gohain et al., 2017). In both of these studies, the transesterification reaction in the

presence of solid base biomass catalyst derived from banana peels was carried out in a batch reactor system. Therefore, it is important to investigate the performance of the solid base catalyst derived from banana peels in a continuous reactor system.

2.6.2.1.2 Chicken Eggshells (CES)

The chicken eggshell is a natural permeable bio-ceramic resulting from the consecutive deposition of various layers around the egg whites in last sections of the hen oviduct (Laca et al., 2017). It is a well-arranged structure with a polycrystalline association throughout the calcified shell (Laca et al., 2017). The composition of eggshells include a frothy layer of cuticle, a calcite or calcium carbonate layer and two shell films, with 7000-17,000 pore channels of funnel-shape which are unevenly spread on the shell surface for water and gases exchange (Laca et al., 2017).
Eggshells constitute approximately 10% of the hen egg (Laca et al., 2017). Eggs are consumed in large quantities worldwide for home and industrial purposes, resulting in eggshells as left over. The disposal of eggshells constitutes an environmental issue, as huge amounts of this residue end up in landfills without any pre-treatment being thus a source of organic pollution (Laca et al., 2017).

As stated by Buasri et al. (2013), eggshells consist of a complex of protein fibers, linked to crystals of calcium carbonate ($CaCO_3$), magnesium carbonate ($MgCO_3$) and calcium phosphate ($Ca_3(PO_4)_2$) as well as of organic substances and water. Calcium carbonate ($CaCO_3$) being the main component of the eggshell (96%), is an amorphous crystal that naturally occurs as a hexagonal crystal named calcite (Buasri et al., 2013). It can be converted to calcium oxide (CaO) through the calcination process, however the suitable calcination temperature should be above 800°C (Ahmad et al., 2015).

Different studies have revealed the potential of eggshells from different birds such as chicken, ostrich, and duck as biocatalysts for biodiesel production (Chakraborty et al., 2010; Buasri et al., 2013; Ahmad et al., 2015; Tan et al., 2015; Andherson et al., 2018). Optimum biodiesel yields of 96 wt. % and 94 wt. % using calcined ostrich-eggshell and chicken-eggshell respectively as solid base catalysts in the transesterification of waste cooking oil have been reported by Tan et al. (2015). The reported operating conditions were as follows: 1.5 wt. % catalyst loading, 12:1 molar ratio of methanol to oil, 65 °C reaction temperature, 2 hours reaction time. Andherson et al. (2018) reported a conversion of waste cooking oil into biodiesel of 81.43% using CaO derived from calcined chicken eggshells at 900 ºC with following operating conditions molar ratio of 1:6 WCO to methanol, a reaction time of 2 hours and a

reaction temperature of 65ºC. Although these studies made use of waste chicken eggshells to derive a solid base catalyst, they were conducted in batch systems. Thus, it is crucial to investigate the performance of chicken eggshells as biomass solid base catalyst in biodiesel production in a continuous system.

2.6.2.1.3 Cocoa Pod husks (CPH)

Cocoa, scientifically named theobroma cacao, of the family Sterculiaceae is one of the leading tropical crops worldwide. It is readily available and cultivated in sub-Saharan Africa (SSA). The SSA especially West Africa accounts for approximately 70% of the global production of cocoa as detailed by Betiku et al. (2017).

Cocoa pod husks (CPH) are an inevitable by-product of cocoa production. Approximately 10 tons of CPH are generated for every ton of dry cocoa bean produced (Betiku et al., 2017). This CPH generated poses an environmental concern as only a small portion of CPH is utilized to produce soap, fertilizers as well as to feed livestock in some parts of West Africa (Amos et al., 2016; Betiku et al., 2017).

As stated by Rachmat et al. (2018), high levels of lignin, cellulose and hemicellulose can be found in cocoa pod husks which can be disintegrated into carbon after calcination process. The ashes of CPH are known to contain 40-60% carbonate content whereas the dried CPH has about 3–9% carbonate content as reported by Ofori-Boateng and Lee (2013). In addition, CPH also have potassium content that can be extracted as a component of K_2CO_3 (Rachmat et al., 2018). For such reasons CPH can serve as a potential biomass solid base catalyst for biodiesel production.

Ofori-Boateng and Lee (2013) and Betiku et al. (2017) investigated the viability of CPH as biomass catalyst for biodiesel production. Ofori-Boateng & Lee (2013) reported optimal biodiesel yields of 91.4 wt. % and 98.7 wt. % using unsupported CPH and supported CPH/MgO respectively to transesterify soy-bean oil to FAME. The optimal conditions reported for these catalysts were as follows: methanol to oil molar ratio of 6:1, reaction temperature of 60 °C, catalyst loading of 1 wt.% and reaction times of 60 min (for supported CPH/MgO) and 120 min (for unsupported CPH) (Ofori-Boateng & Lee, 2013). Betiku et al. (2017) reported an optimal yield of 99.3 wt. % when CPH calcined at 700 °C for 4 h was used as solid base catalyst in the transesterification of neem seed oil (NSO). The optimum conditions reported were as follows: methanol to oil ratio of 0.73 (v/v), catalyst dosage of 0.65 wt. %, and reaction time of 57 minutes at constant temperature of 65 °C (Betiku et al., 2017). Despite the relatively high

yields obtained in both studies, it is imperative to assay the viability of CPH in a continuous reactor set-up.

2.6.2.1.4 Enterolobium cyclocarpum pod husks (ECPH)

Enterolobium cyclocarpum, of the family Fabaceae, commonly known as guanacaste, caro caro, earpod, mexican walnut or elephant's ear tree is a multipurpose and nitrogen-fixing tree (Chacko & Pillai, 1997; Vázquez Yanes et al., 1999).

Enterolobium cyclocarpum pod (ECP) is native to Central and Northern South-America in countries like Mexico, Venezuela, Trinidad, Guyana and Brazil (Chacko & Pillai, 1997; Vázquez Yanes et al., 1999). It is prevalent in tropical parts of both Americas, in the Caribbean Islands and in Florida, Hawaii and Puerto Rico. ECP was exported to many other tropical areas of the world, such as Nigeria, for example (Chacko & Pillai, 1997; Vázquez Yanes et al., 1999).

The enterolobium pods are glossy dark brown in colour, flattened, have an ear-shaped woody aspect (thus the name "ear tree" in many languages), are 7-12 cm in diameter and have a sweet flavour (Vázquez Yanes et al., 1999). They are used in Central America to feed sheep, goats, cattle or horses as well as pigs (Flores et al., 2012; Piñeiro-Vázquez et al., 2013). The pod husks contain saponins and thus are used as detergent to launder clothes (Vázquez Yanes et al., 1999).

Recently, Falowo et al. (2019) made use of ECPH calcined at 700 °C for 4 hours as biomass catalyst in the microwave-assisted transesterification of $Fe_2(SO_4)_3$ pre-treated oil blend and reported a biodiesel yield of 98.77 ± 0.16 wt. % using the following optimum conditions: methanol/oil blend molar ratio of 11.44:1, catalyst dosage of 2.96 wt. % of oil and reaction time of 5.88 min under microwave heating power of 150W. Falowo et al. (2019) study was performed in a batch reactor set-up, thus it is necessary to assess the feasibility of this catalyst in a continuous reactor system.

2.6.2.2 Supported solid base catalysts

Supports represent a pathway to minimize the mass transfer limitation associated with heterogeneous catalysts in liquid phase reactions (Zabeti et al., 2009). Supported catalysts comprise of an active phase dispersed on a carrier (Campanati et al., 2003). The active phase (active components) is responsible for the main chemical reaction because the reaction takes place at the internal surface (i.e. in the pores) of the active phase (Campanati et al., 2003;

Islam et al., 2014). Whereas the support is responsible for providing higher surface area through the existence of pores where active component can be attached (Islam et al., 2014). The support or carrier component has to be more resistant to sintering than the active phase (catalytic species) (Perego & Villa, 1997).

The choice of a catalyst support is based on it exhibiting desirable characteristics such as: inertness, stability under reaction and regeneration conditions, surface area (usually high surface area is desirable), low cost, porosity and appropriate mechanical properties (hardness, attrition resistance and compressive strength) (Perego & Villa, 1997).

Several support materials have been reported to be used in biodiesel production specifically, high performance porous zirconia, titania and alumina catalyst, have shown great promise in terms of their catalytic, thermal, and mechanical stability for long-term continuous esterification and transesterification reactions (Islam et al., 2014; Zabeti et al., 2019).

Recently the potential for pumice as catalyst support has been realized (Borges et al., 2011; Borges & Díaz, 2013). Pumice is an amorphous, permeable volcanic rock that is made of silica and alumina (Cercado et al., 2017). Its permeable structure was mostly formed by liquefied gases included into precipitated materials during the volcanic magma cooling through the air (Borges et al., 2011). Pumice material has been used in numerous applications in different industries such as cosmetic, dental, abrasives, chemical, cement, concrete, ceramic and glass industries, due to it being an inexpensive and wide-ranging geological crude material (Borges et al., 2011).

2.7 Reactor types in biodiesel production

Biodiesel production has been reported with batch and continuous reactors (Aransiola et al., 2014). Batch operations are mostly employed as they are relatively simpler compared to continuous operations (Aransiola et al., 2014). Nonetheless, batch processes require large reactor volumes, which consequently means higher capital investments (Aransiola et al., 2014; Marinkovic et al., 2016). Conversely, continuous processes can achieve a desired conversion of TG using a smaller reactor volume, thus they have a lower production cost compared to batch processes (Marinkovic et al., 2016). Additionally, continuous processes allow for a more uniform quality of the biodiesel produced and they have a higher production capacity than batch processes (Aransiola et al., 2014; Marinkovic et al., 2016). The production capacities of batch and continuous processes have been reported to be in the range of 7.26-7.5 Gg y^{-1} and 8-125 Gg y^{-1} respectively (Aransiola et al., 2014). Table 2.3 presents some types of continuous reactors employed for biodiesel production.

Table 2.3: Types of continuous reactors employed for biodiesel production

Continuous reactor type	Modus operandi	Main parameters	Advantage(s)	Disadvantage(s)	References
Continuous stirred tank reactor (CSTR)	Oil and alcohol are fed continuously and mechanically agitated till process is completed	Agitation speed In –out flowrate	Most used in industrial-scale due to deep understanding of its operation	High energy consumption due to intensive mixing	Mehboob et al., 2016 Zahan & Kano, 2019
Fixed bed reactor (FBR)	Oil and alcohol flow through a static packed catalytic bed and are converted into biodiesel	Bed height Catalyst size Feed flow rate Alcohol to oil molar ratio	No catalyst and product separation required Slow catalyst deactivation Reduced reaction time	High molar alcohol to oil ratio Requires removal process for glycerol(by-product)	Hama et al.,2013 Zahan & Kano, 2019
Microchannel reactor (MCR)	Microchannels (which could be sub-micrometer to sub-millimeter diameter channels) arrange the bulk flow into parallel streams of interchanging reagent slugs which are laminar. The resulting product stream that leaves the microchannels is a biodiesel and glycerol emulsion.	Length and number of channels Nozzle diameter Fluid junction configuration Flow motion	Short reaction time High surface area to volume ratio Effective mixing Effective mass and heat transfer at safer operating conditions	Challenges with scale-up to achieve industrial scale capacity	Sootchiewcharn et al., 2015 El Zanati et al., 2017 Madhawan et al., 2018 Zahan & Kano, 2019;
Membrane reactor (MR)	An emulsion with dispersed oil droplets is formed in the continuous alcohol-rich phase via in-situ oil and alcohol separation process	Membrane type Membrane pore size Residence time Alcohol recycle and flux	Continuous product recovery Produces high purity biodiesel Minimal wastewater generation	Limited knowledge on the unique MR characteristics Its application has small impact in the overall capital cost	Chong et al., 2013 Gumus et al., 2013 Zahan & Kano, 2019
Reactive distillation column (RDC)	Oil is fed to the top of the column and	Column size	No downstream	Complex operation	Poddar et al., 2015

	vapour alcohol is fed to the bottom while the resultant biodiesel is pumped from the bottom and water (by-product) is distilled from the top	Number of stages (reactive, rectifying, and stripping) Molar reflux ratio Reboiler duty Molar alcohol to oil ratio Feed flowrate, and location Reaction temperature and pressure	processes required Shorter reaction time No need for excess alcohol Minimal catalyst use Increased selectivity Reduced waste generation	Significant number of parameters to control	Crudo et al., 2016 Yohana et al.,2016

2.8 Important physicochemical and fuel properties for analysis of biodiesel quality

Biodiesel, which similar to petro-diesel fuel also runs in the CI engines, is characterized for its physicochemical and fuel properties (Demirbas et al., 2016). A few of these properties, which will be discussed in detail, include density, viscosity, acid value, iodine value, cetane number, flash point, cloud and pour points and higher heating value (HHV) (Demirbas et al., 2016).

2.8.1 Density and specific gravity of biodiesel

The density is an essential property of biodiesel fuel. The density of biodiesel is analyzed using ASTM standard D1298 and EN ISO 3675 test methods and it should be tested at the reference temperature of 288 K (Ashraful et al., 2014; Demirbas et al., 2016).

Specific gravity is defined as the ratio of the density of a liquid to the density of water. The biodiesel specific gravity ranges between 0.87 and 0.89 (Demirbas, 2006).

Regardless of the feedstock type, all biodiesel fuels are denser and less compressible than the diesel fuel (Alptekin & Canacki, 2008). The density and compressibility have a direct impact on the engine performance characteristics, specifically on the fuel injection system, i.e. injection timing, injection spray pattern and injection fuel amount (Wan Ghazali et al., 2015).

In addition, a change in fuel density will have an effect in the engine output power because of the different mass of injected fuel (Wan Ghazali et al., 2015).

A fuel with lower density will enhance the atomization and air–fuel mixture formation efficiency (Wan Ghazali et al., 2015). On the other hand, a higher density will cause an increase of the fuel droplets diameter (Wan Ghazali et al., 2015). This occurs because of an increase in the infiltration of the fuel droplets in the combustion chamber caused by the inertia of large fuel droplets (Wan Ghazali et al., 2015). Additionally, a high density leads to an increase in particulate matter (PM) and NOx emission in diesel engines (Szybist et al., 2007; Wan Ghazali et al., 2015).

2.8.2 Viscosity of biodiesel

The viscosity of an engine fuel is one of the most significant properties as it plays a predominant role in the fuel spray, mixture formation and incineration process (Demirbas et al., 2016). Also, viscosity influences the atomization quality, the size of fuel drop and the penetration. Thus, affecting the quality of combustion (Tate et al., 2006). The lower the viscosity of the biodiesel, the easier it is to pump and atomize and achieve finer droplets (Demirbas et al., 2016). The kinematic viscosity of biodiesel is analyzed using the ASTM D445 and EN ISO 3104 test methods (Wan Ghazali et al., 2015). The viscosity values of vegetable oils reduce significantly after transesterification. Demirbas et al. (2016) reported that the viscosity values of vegetable oils are between 27.2 and 53.6 mm^2/s, whereas those of vegetable oil methyl esters are between 3.6 and 4.6 mm^2/s.

It has become imperative to ensure that the viscosity of biodiesel is within the standard limits because low viscosity can cause leaking in the fuel system (Wan Ghazali et al., 2015). High viscosity, on the other hand, causes poor flow of fuel in the engine combustion chamber during intake stroke (Ashraful et al., 2014). This is because the duration of intake stroke is extended thus, it takes a long time for the fuel to mix with air (Ashraful et al., 2014). Also, high viscosity can cause more problems in cold weather conditions because the viscosity increases as the temperature decreases (Wan Ghazali et al., 2015). Additionally, high viscosity will lead to less accurate operation of the fuel injectors and also increase the engine deposits due to the incomplete combustion (Wan Ghazali et al., 2015; Demirbas et al., 2016).

2.8.3 Acid value and %FFA of biodiesel

The acid value constitutes an important parameter of biodiesel. The acid value content in an oil sample is the amount in mg of KOH required to neutralize 1 g of oil sample (Mahajan et al., 2006).

The acid number of biodiesel derives almost solely from the fatty acid (FA) content (Mahajan et al., 2006). This is because FA can be formed by the hydrolysis of ester bonds in both the TG feedstock and the biodiesel during its production (Mahajan et al., 2006). FA may cause engine deposits especially in fuel injectors, by catalyzing polymerization in hot recycling fuel loops (Mahajan et al., 2006).

ASTM D 664 is the reference test technique used to analyzed the acid value of biodiesel (Mahajan et al., 2006). Most of the common techniques for measuring acid number are based on titrations with standardized base, the end point being distinguished by the color change of an indicator (Mahajan et al., 2006).

As per ASTM D974, the acid value is calculated using Equation (2.1):

$$\text{Acid value (AV)} = \frac{56.1 \times \text{N} \times \text{V}}{\text{w}}$$

(Mansir et al., 2018) (2.1)

Where:
AV- Acid value (mg KOH/g).
V- Volume of potassium hydroxide (KOH) required by the oil sample (mL).
N- Normality of the titration solution.
w- Weight of the oil (g).

Hence, the percentage of free fatty acids (%FFA) is calculated using Equation (2.2).

$$\%\text{FFA} = \frac{\text{Acid value}}{1.99}$$

(Mansir et al., 2018) (2.2)

2.8.4 Iodine value of biodiesel

The iodine value (IV), measures the unsaturation of oils and fats and their fatty acid derivatives by determining the quantity of iodine in grams that can be integrated into 100 g of biodiesel under standard conditions (Bart et al., 2010; Gouveia et al., 2017).The compulsory limit as per standard EN 14214 is 120 g I_2/100 g (Gouveia et al., 2017). The IV of biodiesel from soybean and sunflower is above this specification limit (Gouveia et al., 2017).

Iodine value is utilized for determining the quality of biodiesel fuel derived from vegetable oils (Mittelbach, 1996). The IV reflects both the propensity of an oil or fat to oxidise and to polymerise and form engine deposits (Bart et al., 2010). In addition, biodiesel fuels with a low IV show lower NOx emissions (Bart et al., 2010).

Numerous alternative calculation procedures were proposed to determine the iodine value of biodiesel fuels straight from their composition, including the American Oil Chemists' Society (AOCS) method Cd 1d92 (Kyriakidis & Katsiloulis, 2000). As per EN 14214 (Annex B) to determine iodine value of biodiesel, the mass percentage of FAME is multiplied by a specific weighting factor (Kyriakidis & Katsiloulis, 2000). Theoretical iodine values calculated from the total quantity of double bonds using the fatty acid composition tend to be slightly higher (5–10%) than the iodine values determined by titration, due to the presence of unsaponifiables in the crude oils (Bart et al., 2010).

The iodine value of an oil is affected by its fatty acid molecular weight (Bart et al., 2010). However, it is mainly dependent on the percentage concentration of unsaturated fatty acid constituents and the amount of double bond(s) D present in the structure (Bart et al., 2010). Thus, determining the iodine value provides a practical quantification of unsaturation as long as the double bonds are not conjugated with each other neither with carbonyl oxygen (Bart et al., 2010). Nonetheless, various fatty acid profiles and different fatty acid structures can produce the same iodine value (Knothe, 2002).

2.8.5 Cetane number of biodiesel

The cetane number is an essential property for determining the ignition quality of biodiesel fuel (Bamgboye & Hansen, 2008). It quantifies the readiness of the fuel to auto-ignite when injected into the engine (Demirbas et al., 2016). The ignition quality is one of the properties of biodiesel that is determined by the structure of the FAME constituent (Bamgboye & Hansen, 2008).

A lower cetane number indicates longer ignition delay (Wan Ghazali et al., 2015). Long ignition delay is not adequate since it provokes diesel knocking (Wan Ghazali et al., 2015). In addition, the low cetane number will increase gaseous and particulate matter (PM) exhaust emissions because of incomplete combustion (Wan Ghazali et al., 2015).

The longer the chain is, the higher the cetane number (Wan Ghazali et al., 2015). Biodiesel has a higher cetane number compared to pure diesel due to its longer fatty acid carbon chains and the presence of saturation in molecules (Harrington, 1986; Pinzi et al., 2009). A high cetane number is viewed as a significant advantage in terms of engine performance and emissions, as it allows biodiesel-fueled engines to operate more smoothly and with less noise (Knothe et al., 2003). In contrast, an excessive high cetane number will lead to fuel ignition in a short distance to the injector and cause extreme heating of the injector (Alptekin & Canacki, 2009). Thus, potentially leading to plugging of injector nozzle by cooked fuel particles inside the injector (Alptekin & Canacki, 2009).

2.8.6 Flash point of biodiesel

Flash point of a fuel is defined as the lowest temperature at which the fuel will naturally ignite without the presence of a flame or spark (Demirbas et al., 2016). At this lowest temperature, vapor stops burning if the ignition source is removed (Demirbas et al., 2016). Although the flash point does not have a direct influence on the combustion, it is relevant when considering fuel handling, transportation and storage (Wan Ghazali et al., 2015).

The flash point of biodiesel is analyzed using ASTMD93 and EN ISO 3697 test methods (Wan Ghazali et al., 2015). Canacki and Van Gerpen (1999) stated that the flash point of biodiesel will be much higher than that of diesel fuel irrespective of the feedstock grade used for biodiesel production, reflecting the not so volatile nature of the fuel. There are a number of factors that influence the change in biodiesel flash point, with residual alcohol content being one of them (Wan Ghazali et al., 2015). Moreover, the flash point is also affected by the chemical compositions of the biodiesel; including the number of double bonds, number of carbon atoms, etc (Carareto et al., 2012).

2.8.7 Cloud and pour points of biodiesel

Cloud and pour points are two essential parameters for low-temperature applications of a fuel (Kinast, 2003). The cloud point is defined as the temperature at which wax initially becomes visible once the fuel is cooled (Lee et al., 1995). The pour point is the temperature at which the quantity of wax from a solution is enough to gel the fuel (Kinast, 2003). Thus, it is the lowest temperature at which the fuel can flow and can still be pumped before it becomes a cloud of wax crystals once cooled (Kinast, 2003). Operational complications may arise from the formation of these crystals due to the plugging of fuel lines and filters (Kinast, 2003).

Contrary to traditional diesel fuel, all biodiesel irrespective of its source have higher cloud and pour points due to the higher amount of saturated fatty acids present in biodiesel (Wan Ghazali et al., 2015).The cloud and pour point of vegetable oil methyl esters are 15–25K higher than those of diesel fuels (Demirbas et al., 2016). However, biodiesel from vegetable oil has lower cloud and pour point than that of biodiesel from fats and greases (Wan Ghazali et al., 2015).

The higher pour and cloud point property constitutes one of the main hindrances against biodiesel widespread usage, particularly in cold weather conditions (Wan Ghazali et al., 2015). An alternative to overcome this low-temperature related issue is to blend biodiesel with the diesel fuel (Demirbas et al., 2016).

2.8.8 High heating value of biodiesel

High heating value (HHV) is another key parameter in the choice of a fuel. Biodiesel has a slightly lower HHV (39–41 MJ/kg) compared to that of gasoline (46 MJ/kg), petro-diesel (43 MJ/kg), or petroleum (42 MJ/kg) due to their higher oxygen content (Demirbas et al., 2016).
The high heating value is directly affected by two other parameters, specifically the ash and extractive contents (Demirbas et al., 2016). High ash content of an oil reduces its attractiveness as a fuel, while high extractive content increases its desirability as a fuel (Demirbas et al., 2016).

2.9 Biodiesel standards

Biodiesel has distinctive physicochemical properties compared with diesel fuel. Different variables can influence the quality of biodiesel fuel, namely: the feedstock quality, fatty acid composition of the feedstock, type of production and refining process applied and post-production factors (Atabani et al., 2013). Thus, standards and characteristics of biodiesel fuel are required. Biodiesel standards are in place to protect both the biodiesel consumers and producers, to guarantee that only high-quality biodiesel reaches the market and to aid in the development of biodiesel industries (Atabani et al., 2013; Kassem & Camur, 2017).

The two main fuel standards are ASTM D6751 in the United States and EN 14214 (European Committee for Standardization (CEN) in the European Union (Kassem & Camur, 2017). All substitute biodiesel fuels should meet these international standard specification (Demirbas, 2016).These standards define the physicochemical characteristics of a variety of biodiesel produced from edible and non-edible oil resources (Atabani et al., 2013). Table 2.4, presents ASTM 6751 and EN 14214 specifications of biodiesel fuels for a few physicochemical properties.

In South Africa, the SANS 1935 automotive standard is the regulatory standard for biodiesel, i.e. fatty acid alkyl ester, which can only be obtained from vegetable oils (SABS, 2011). This implies that either oil-seeds or their resulting unrefined vegetable oil can be utilized for producing biodiesel (FAME) in South Africa (SABS, 2011).

Table 2.4: Biodiesel specifications (Atabani et al., 2013; Kassem & Camur, 2017 and Patade et al., 2018)

Property	Unit	Biodiesel			
		ASTM D6751		EN14214	
		Limits	Test Method	Limits	Test Method
Flash point	°C	130 min.	ASTM D93	101 min.	EN ISO 3679
Cloud point	°C	-3 to -12	ASTM 2500	---	---
Pour point	°C	-15 to -16	ASTM 97	---	---
Cold Filter plugging point (CFPP)	°C	+5 max.	ASTM D6371	---	EN14214
Distillation temperature	°C	360	ASTM D1160	---	---
Density at 15°C	kg/m^3	880	ASTM D1298	860-900	EN ISO 3675/12185
Kinematic viscosity at 40 °C	mm^2/s	1.9-6.0	ASTM D445	3.5-5.0	EN ISO 3104, ISO 3105, EN ISO 310
Moisture	wt. %	---	---	0.05 max.	EN1412
Acid number	mg KOH/g	0.5 max.	ASTM D664	0.5 max.	EN 14104

Iodine number	g I_2/ 100g	---	---	120	EN14111
Cetane number		47 min.	ASTM D613	51 min.	EN ISO 5165
Oxidation stability		---	---	3h min.	EN14112
Cold soak filtration	s	360	ASTM D6751	---	---
Ester content	% (m/m)	---	---	96.5 min.	EN 14103
Linolenic acid methyl ester	% (m/m)	---	---	12 max.	EN 14103
Polyunsaturated (≥ 4 double bonds) methyl esters	% (m/m)	---	---	1 max.	EN 14104
Monoglycerides	% (m/m)	---	---	0.8 max	EN14105
Diglycerides	% (m/m)	---	---	0.2 max	EN14105
Triglycerides	% (m/m)	---	---	0.2 max	EN14106
Free glycerine	% (m/m)	0.02 max.	ASTM D6584	0.02 max.	EN1405/14016
Total glycerin	% (m/m)	0.24	ASTM D6548	0.25	EN14015
Methanol content	% (m/m)	---	---	0.2 max.	EN14110
Group I metals (Na, K)	mg/kg	---	---	5.0 max	EN14108 EN14109 EN14538
Group II metals (Ca, Mg)	mg/kg	---	---	5.0 max.	EN14538
Phosphorous	%(m/m)	0.001 max.	ASTM D4951	0.001 max	EN14107
Carbon residue	% (m/m)	0.05 max.	ASTM D4530	0.3 max.	EN ISO10370
Total contaminants	mg/kg	24	ASTM D5452	24	EN12662

2.10 Benefits of biodiesel

2.10.1 Economic benefits

Biofuels, particularly biodiesel, are frequently more expensive than fossil fuels on an energy equivalent basis (Baskar & Aiswarya, 2016). A survey showed evidence that the biodiesel rate was above 0.5 US$/liter when compared to the petro-diesel rate of 0.35 US$/liter (Baskar & Aiswarya, 2016). In addition, the cost seems to be three times higher in developing countries (Baskar & Aiswarya, 2016).Therefore, in order to make biodiesel economically viable, immense research and development is required along with administrated policies from the government (Gheewala et al., 2013; Baskar & Aiswarya, 2016).

The cost of raw material and reaction catalyst constitutes the main biodiesel production cost (Baskar & Aiswarya, 2016). Furthermore, the predicted cost of raw material and catalyst were found to be 10 % of the total production cost in large units as opposed to 40-60 % in small-scale units (Baskar & Aiswarya, 2016). Small-scale production facilities often follow batch mode of operation, while medium to large-scale facilities follow continuous process (Baskar & Aiswarya, 2016). In order to reduce the production cost, the integrated supercritical condition is recommended to minimize the investment in production processes (Pinzi et al., 2010). The net energy storage fuel is another contributing factor towards the production cost of biodiesel.

Thus, continuous transesterification plays a major role for biodiesel production (Baskar & Aiswarya, 2016).

Contrary to petroleum diesel, biodiesel production can easily be increased and it requires less time as there is no need for drilling, transportation and refining (Mishra & Goswami, 2017). The good lubricity properties of biodiesel enhance lubrication in the fuel pump and injector units, which consequently reduces engine wear and increases the efficiency of the engine. In addition, biodiesel can be used in the diesel engine with little or no engine modification depending on the blending percentage of biodiesel with petroleum diesel (Mishra & Goswami, 2017; Gupta & Rathod, 2018). The high cetane number of biodiesel (60-65 depending on the vegetable oil used) reduces ignition delay. Its high flash point (100-170 °C), makes biodiesel safer to handle, transport, distribute, utilize and store than petroleum diesel which has a much lower flash point of 60- 80 °C (Mishra & Goswami, 2017).

Another economic benefit of biodiesel, is that it can be locally produced in any country without importation tax implications (Li et al., 2009). In essence, the production of biodiesel could be a source of foreign exchange income, investment and employment opportunity. Also, non-edible oils can be cultivated for the production of biodiesel. Production of biodiesel has the potential to help improve the availability of energy for the growing population of Africa as well as stimulate economic development in rural areas (Hassan & Ayodeji, 2019).

2.10.2 Environmental benefits

In general, biofuels are intended to be a potential source of renewable energy that could possibly substitute the traditional fossil fuels and provide sustainable fuel with less ecological problems i.e. global warming and greenhouse gas effects (Mansir et al., 2018). As per EPA (2010), although the production of biofuels results in GHG emissions at numerous phases of the process, EPA's (2010) analysis of the Renewable Fuel Standard (RFS) anticipated that a lower lifecycle of GHG emissions could be yielded from diverse types of biofuels than from gasoline over a 30-year timeline. Biodiesel is presently one of the most broadly accepted alternative renewable sources of energy option to traditional fossil fuel (Mansir et al., 2018).

Biodiesel has multiple advantages. It has 10-11% oxygen, which makes it a fuel with high combustion features (Chincholkar et al., 2005; Li et al., 2009; Balat & Balat, 2010). On a lifecycle basis, burning biodiesel produces 78% less CO_2 than its counterpart, i.e. petroleum diesel fuel. It also results in less smoke due to free soot (Chincholkar et al., 2005). Because of its renewability, biodegradability, sustainability, non-flammability, non-toxicity, eco-friendly

nature and the fact that it is free from sulphur and aromatic content, biodiesel is a perfect fuel for highly polluted cities and urban regions. In addition, biodiesel fuel generates less particulate matter in the atmosphere and hence decreases air toxicity. This fact alone contributes to a 90% reduction in cancer risks as well as neonatal defects as biodiesel combustion is less pollutant than its counterpart (Chincholkar et al., 2005; Balat & Balat, 2010).

Even though most of the current commercial biodiesel production relies fully on edible vegetables oils such as rapeseed (6.01 million ton), palm oil (6.34 million ton), soybean oil (7.08 million ton) and some non-edible oil such as Jatropha curcas oil and castor oil as major global feedstocks, the potential of waste cooking oil as second generation feedstock for commercial biodiesel production has been realized (Mansir et al., 2018). Latest studies suggested that the production cost of FAME could be halved through the use of WCO in contrast to the high grade vegetable oils (Mansir et al., 2018). Approximately 15 million tons of waste cooking oil has been disposed in water or land annually across the globe. Such amount of low-cost feedstock deserves noteworthy consideration, as it could bridge major gap in present biodiesel demands. Waste cooking oil, when properly treated will yield biodiesel with less CO_2 emission at reasonably low-cost. Thus, making biodiesel economically and socially feasible as a renewable fuel (Mansir et al., 2018).

2.11 Summary

In light of the reviews presented in this chapter, it is crucial for the biodiesel industry to continually improve on aspects that will accentuate its commercial viability. The review provides a concise synopsis of the various feedstock sources, alcohol types, types of reactors as well as catalyst types used in producing biodiesel via transesterification of plant-oils. In this research study, the main goal is to explore cost-effective ways to produce biodiesel that will strengthen its prospect as the next generation green fuel via the continuous transesterification of waste sunflower oil (WSFO) with methanol in the presence of biomass-derived solid base catalysts. Emphasis is given on the catalytic outcomes of biomass-derived solid base catalysts with a view to assess their implementation at industrial-scale. The chapter also reviewed key parameters that affect the yield of biodiesel produced via catalyzed transesterification of vegetable oil with an alcohol. Finally, the chapter reviews the economic and environmental benefits of biodiesel fuel.

CHAPTER 3
MATERIALS AND METHODS

3.1 Introduction

This chapter provides in depth description of the materials used for the experiments, the experimental procedures followed and the analytical methods used in this study. The experimental approach used in this study is explained in section 3.2 of the chapter. This chapter comprises of the three key parts which include:

(i) Sections 3.4.2 and 3.4.3 describe the experimental procedures for the determination of physicochemical and fuel properties of WSFO as well as its fatty acid profile.

(ii) Section 3.4.5 describes all the experimental procedures and analytical techniques employed in phase 1 of the study, specifically in the synthesis and characterization of the biomass-derived solid base catalysts (subsections 3.4.5.1 and 3.4.5.2), in the transesterification of WSFO to waste sunflower methyl esters (WSFME) using the biomass-derived solid base catalysts in a batch reactor (subsection 3.4.5.3) and in the determination of physicochemical and fuel properties of phase 1 produced WSFME (subsection 3.4.5.4).

(iii) Section 3.4.6 provides detailed description of the experimental procedures applied in phase 2 of the study, specifically in the preparation and characterization of the supported biomass-derived solid base catalyst (subsections 3.4.6.1, 3.4.6.2), in the experimental determination of density of the supported biomass-derived solid base catalyst (subsection 3.4.6.3), in the transesterification of WSFO to waste sunflower methyl esters (WSFME) using the supported biomass-derived solid base catalyst in a continuous reactor (subsection 3.4.6.4) and in the determination of physicochemical and fuel properties of phase 2 produced WSFME (subsection 3.4.6.5).

3.2 Experimental Approach

The experimental approach in this study is divided into two phases. The phase 1 experimental approach involved the synthesis of the four selected biomass-derived solid base catalysts and the investigation of their performance under the same set of process conditions in a batch reactor system for biodiesel production. The best performance catalyst; in terms of biodiesel yield and quality was chosen to be used in phase 2. The phase 2 experimental approach involved developing an appropriate continuous reactor system to produce biodiesel and studying the kinetics of the transesterification reaction of WSFO using the best performance biomass-derived solid base catalyst identified in phase 1 of the study.

3.3 Materials

3.3.1 Feedstock, biomass wastes and catalyst support

The list of the feedstock, biomass wastes and catalyst support used in this study is given in Table 3.1.

Table 3.1: List of feedstock, biomass wastes and catalyst support used in the study

Material	Source	Use in the study
Waste sunflower oil (WSFO)	Plumstead Fisheries (Cape Town, South Africa)	Feedstock
Banana peels	Food Lovers Market (Cape town, South Africa)	Biomass-derived solid base catalyst
Chicken eggshells	Eastern Bazaar restaurant (Cape Town, South Africa)	Biomass-derived solid base catalyst
Cocoa pod husks	Obafemi Awolowo University (Ile-Ife, Nigeria)	Biomass-derived solid base catalyst
Enterolobium cyclocarpum pod husks	Obafemi Awolowo University (Ile-Ife,Nigeria)	Biomass-derived solid base catalyst
Synthetic pumice granules (0.8- 3 mm)	Merck	Catalyst support

3.3.2 Chemicals and reagents

Table 3.2 provides the list of chemicals and reagents used in this study. These were of analytical grade.

Table 3.2: List of chemicals and reagents used in the study

Chemical/Solvent	Source	Grade/Purity
Methanol	Merck	99.9%
Ethanol	Merck	99.9%
2-Propanol	Merck	≥99.8%
Cyclohexane	Labchem	99.9%
n-hexane	Kimix Chemicals	85%
Chloroform	Merck	≥99.0%
Glacial acetic acid	Merck	99.9%
Hydrochloric acid	Merck	32%
Wij's solution	Labchem	99.0%
Hydrated ferric sulfate	Merck	97%
Potassium hydroxide pellets	Merck	≥85.0%
Potassium iodide	Labchem	≥99.0%
Phenolphthalein indicator	Merck	
Sodium sulfate	Merck	≥99.0%
Sodium thiosulfate 5hyd	Labchem	≥99.0%
Starch indicator	Labchem	

3.3.3 Glassware

The glassware used in this study included beakers, conical flasks, burette, separating funnels, pipette, volumetric flask, measuring cylinder, pycnometers (density bottles) and desiccators.

3.3.4 Equipment

The equipment used in this study comprised of retort stands, Buchner funnel and filter paper, thermometers, digital weighing balance, mortar and pestle, water bath, overhead stirrers, oven, hot plate with magnetic stirrer, sieve shaker, peristaltic pumps and furnace.

3.4 Methods

3.4.1 WSFO sample preparation

The collected WSFO used in this study was firstly filtered under vacuum using a Buchner funnel and filter paper (ø110 mm) to remove any small food particles. The filtered WSFO was stored for further analysis and subsequently pre-treated as described in section 3.4.4.

3.4.2 Physicochemical and fuel properties of WSFO

The physicochemical and fuel properties of WSFO used in this study include kinematic viscosity, specific gravity (SG), acid value (AV), percentage of free fatty acids (%FFA), saponification value (SV), iodine value (IV), peroxide value (PV), moisture content, cetane number (CN), diesel index (DI), aniline point (AP), American petroleum index (API) and high heating value (HHV).

3.4.2.1 Determination of kinematic viscosity of WSFO

The kinematic viscosity of WSFO used in this study was determined using Equation (3.1).
The dynamic viscosity of the WSFO used in this study was determined using a Hybrid rheometer (Discovery HR-1) fitted with a Peltier concentric cylinder temperature system set at a temperature of 40 °C, with a set gap of 5.9171 mm and at a shear rate of 50 s^{-1}.

$$\text{kinematic viscosity of WSFO}_{(\text{at } 40\ ^\circ\text{C})} = \frac{\text{dynamic viscosity of WSFO}_{(\text{at } 40\ ^\circ\text{C})}}{\text{density of WSFO}_{(\text{at } 40\ ^\circ\text{C})}} \quad (3.1)$$

3.4.2.2 Experimental determination of specific gravity (SG) of WSFO

The specific gravity of WSFO used in this study was experimentally determined using a Bomex pycnometer. Firstly, a 50 mL empty pycnometer was weighed and recorded. Thereafter, the pycnometer was calibrated by filling it with distilled water at the desired temperatures, 15 ^oC 25 ^oC and 40 ^oC, to estimate the exact volume occupied by the water at each temperature. The weight of the pycnometer filled with distilled water at each temperature was recorded. The pycnometer was emptied and allowed to air dry for a few minutes. The dried pycnometer was filled with a volume of WSFO (at the desired temperatures) equal to the volume of distilled water previously used for calibrations (as shown in Figure 3.1). The weight of the pycnometer filled with WSFO at each temperature was recorded. From the weight readings and knowing the exact volume occupied by the WSFO, the density of WSFO at each temperature was found. The specific gravity of the WSFO at each temperature was thus calculated using Equation (3.2).

$$\text{SG} = \frac{\text{density of WSFO}(\text{g.cm}^{-3})}{\text{density of water }(\text{g.cm}^{-3})} \quad (3.2)$$

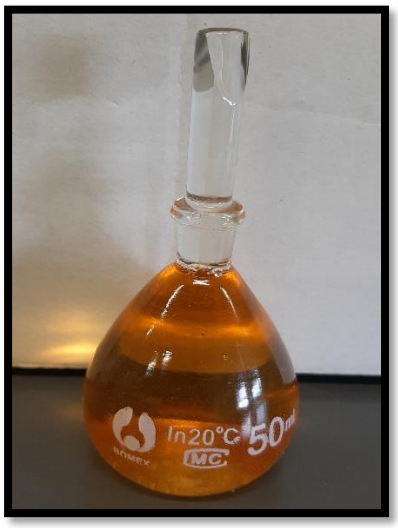

Figure 3.1: Pycnometer filled with WSFO at 25 °C

3.4.2.3 Experimental determination of acid value (AV) and percentage of free fatty acids (%FFA) of WSFO

The AV and %FFA of WSFO used in this study were experimentally determined using a standard method from the Association of Official Analytical Chemists (AOAC) (1990).

2.5 g of WSFO sample was weighed into a dry 250-mL conical flask using an analytical weighing balance. 25 mL of 2-propanol (isopropanol) was added and the flask was mechanically agitated to ensure dissolution of WSFO. The mixture of WSFO-isopropanol was heated to enhance homogenization. In sequence, 1 mL of phenolphthalein indicator was added to the mixture. The mixture of WSFO-2-propanol-phenolphthalein indicator was titrated dropwise with 0.1 N KOH solution until the light pink end-point was reached and the colour persisted for about 15 seconds. The acid value and %FFA of WSFO were estimated using Equations (2.1) and (2.2).

3.4.2.4 Experimental determination of saponification value (SV) of WSFO

The saponification value of WSFO used in this study was experimentally determined using a standard method from the Association of Official Analytical Chemists (AOAC) (1990).
2 g of WSFO sample was weighed into a dry 250-mL conical flask and 25 mL of 0.5 M ethanolic potassium hydroxide was added. The mixture of WSFO-ethanolic potassium hydroxide was agitated and allowed to boil at 70°C for 60 min, yielding a warm soapy solution. In order to achieve a uniform temperature in the flask, a reflux condenser was attached to it. Two drops of phenolphthalein indicator were added to the warm soapy solution and then titrated with 0.5 N HCl until the pink colour of the indicator disappeared indicating the end point. This procedure was also carried out without the WSFO to determine the volume of HCl required by the blank.

The saponification value (SV), which is given in mg KOH/g oil, was calculated thus:

$$\mathrm{SV} = 56.1 \times \frac{(\text{vol. of HCl required by blank} - \text{vol. of HCl required by WSFO}) \times 0.5\ \text{N HCl}}{\text{weight of WSFO sample (g)}} \tag{3.3}$$

3.4.2.5 Experimental determination of iodine value (IV) of WSFO

The iodine value of WSFO used in this study was experimentally determined using a standard method from the Association of Official Analytical Chemists (AOAC) (1990).
0.26 g of WSFO sample was weighed into a 250 mL dry conical flask. 10 mL of cyclohexane was added to the WSFO to ensure dissolution. 20 mL of Wij's solution was added to the mixture of WSFO-cyclohexane and swirled gently. The mixture was allowed to stand in the dark for 30 min at room temperature and 20 mL of 10% potassium iodide (KI) solution was added. The resulting solution was titrated with 0.1 M sodium thiosulfate ($Na_2S_2O_3$) using starch as indicator until a colourless solution was reached. This procedure was also carried out without the WSFO to determine the volume of $Na_2S_2O_3$ required by the blank.

The iodine value (IV), which is given in g of I_2/100 g oil, was calculated thus:

$$\mathrm{IV} = \frac{(\mathrm{B} - \mathrm{S}) \times \mathrm{N} \times 12.69}{\mathrm{w}} \tag{3.4}$$

Where:

B – Volume of the sodium thiosulfate required by the blank (mL).

S – Volume of the sodium thiosulfate required by the WSFO sample (mL).

N – The normality of the titration solution.

w- Weight of the WSFO sample (g).

3.4.2.6 Experimental determination of peroxide value (PV) of WSFO

The peroxide value of WSFO used in this study was experimentally determined using a standard method from the Association of Official Analytical Chemists (AOAC) (1990).

2 g of WSFO sample was weighed into a dry 250-mL conical flask. 40 mL of glacial acetic acid-chloroform mixture (2:1) and 2 g KI powder were added. The mixture of WSFO-glacial acetic acid-chloroform-KI powder was allowed to boil at 70°C in a water bath for 1 min. The boiled mixture was then poured into another flask containing 40 mL of 5% KI and was washed twice with 50 mL of distilled water. The resulting solution was titrated dropwise with 0.004 M sodium thiosulfate ($Na_2S_2O_3$) using starch as an indicator until the blue-black colour completely disappeared and a colourless solution was reached.

The peroxide value (PV), which is given in meq of O_2/kg oil, was calculated thus:

$$\mathrm{PV} = \frac{\text{Volume of } \mathrm{Na_2S_2O_3}\ (\mathrm{L}) \times \text{Normality of } \mathrm{Na_2S_2O_3}\ \left(\mathrm{meq}\frac{\mathrm{O_2}}{\mathrm{L}}\right)}{\text{weight of WSFO sample (kg)}} \tag{3.5}$$

3.4.2.7 Experimental determination of moisture content of WSFO

The moisture content of WSFO used in this study was experimentally determined using the oven-dry method.

5 g of WSFO sample was weighed into a glass petri dish of 5 cm in diameter and 2 cm deep with a tight fit-over cover. Thereafter, it was placed in the oven at a temperature of 120 °C. The weight of WSFO sample was checked at 30 min intervals until a constant weight was obtained, i.e. when no additional loss of 0.055% was observed. The final weight of the sample was recorded as the dry WSFO sample. And the moisture content was calculated using Equation (3.6).

$$\text{Moisture content}(\%) = \frac{\text{weight of wet WSFO (g)} - \text{weight of dry WSFO(g)}}{\text{weight of wet WSFO (g)}} \quad (3.6)$$

3.4.2.8 Determination of cetane number (CN) of WSFO

The cetane number (CN) of WSFO used in this study was determined using Equation (3.7) as described by Krisnangura (1986).

$$\text{CN} = 46.3 + (5458/\text{SV}) - (0.225 \times \text{IV}) \quad (3.7)$$

Where:
CN- Cetane number (dimensionless)

3.4.2.9 Determination of diesel index (DI) of WSFO

The diesel index (DI) of WSFO used in this study was determined using Equation (3.8) as described by Haldar et al. (2009).

$$\text{DI} = (\text{CN} - 10)/0.72 \quad (3.8)$$

Where:
DI – Diesel index (dimensionless)

3.4.2.10 Determination of American petroleum index (API) of WSFO

The American petroleum index (API) of WSFO used in this study was determined using Equation (3.9) as described by Haldar et al. (2009).

$$\text{API} = (141.5/\text{ SG at } 15℃) - 131.15 \quad (3.9)$$

Where:
API – American petroleum index (dimensionless)

3.4.2.11 Determination of aniline point (AP) of WSFO

The aniline point (AP) of WSFO used in this study was determined using Equation (3.10) as described by Haldar et al. (2009).

$$\mathrm{AP} = (\mathrm{DI} \times 100/\mathrm{API}) \quad (3.10)$$

Where:
AP – Aniline point (°F)

3.4.2.12 Determination of high heating value (HHV) of WSFO

The high heating value (HHV) of WSFO used in this study was determined using Equation (3.11) as described by Demirbas (1998).

$$\mathrm{HHV} = 49.43 - [0.041 \times (\mathrm{SV}) + 0.015 \times (\mathrm{IV})] \quad (3.11)$$

Where:
HHV- High heating value (MJ/kg)

3.4.3 Determination of fatty acid profile of WSFO

The fatty acid profile of WSFO used in this study was determined using gas chromatography-flame ionization detector (GC-FID (Agilent 7890A)). The column type was HP88 with the following dimensions: 100 mm length, 250 µm inner diameter and 0.25 µm film thickness. Nitrogen was used as the carrier gas for the GC analysis at a flowrate of 1.0 mL/min and at an injection volume and injection temperature of 1 µl (split; 50:1) and 250 °C respectively.

3.4.4 Pre-treatment of WSFO using ferric-sulfate [$Fe_2(SO_4)_3$] (esterification process)

The pre-treatment of WSFO using ferric-sulfate [$Fe_2(SO_4)_3$] as solid acid catalyst was necessary to lower the acid value of WSFO (5.16 ± 0.32 mg KOH/g) to less than 2 mg KOH/g before performing transesterification reactions in phase 1 and phase 2 of the experiments.

In this process, 155 mL of WSFO was dispensed into a 500 mL four neck square bottom jacketed glass reactor equipped with a reflux condenser and an overhead stirrer. The WSFO esterification process set-up can be seen in Figure 3.2 (a). Thereafter, 182 mL of methanol (MeOH) was added to the reactor and the mixture of WSFO-MeOH was allowed to mix for 5 min. The temperature of the reaction was kept at 65°C throughout the duration of the process. 4.65 g of ferric sulfate [$Fe_2(SO_4)_3$], which prior to usage was dehydrated in an oven for 2 hours at 105 °C, was added to the mixture of WSFO-MeOH as a solid acid catalyst and the reaction ended after 40 min elapsed. Separation of the resultant reaction mixture was effected using a separating funnel and then allowed to stand under gravity for 2 hrs. The resulting reaction mixture separated into two layers: MeOH/water layer (top) and esterified waste sunflower oil (EWSFO)/catalyst layer (bottom) as shown in Figure 3.2 (b). The bottom layer was decanted into a beaker and heated to remove excess methanol.

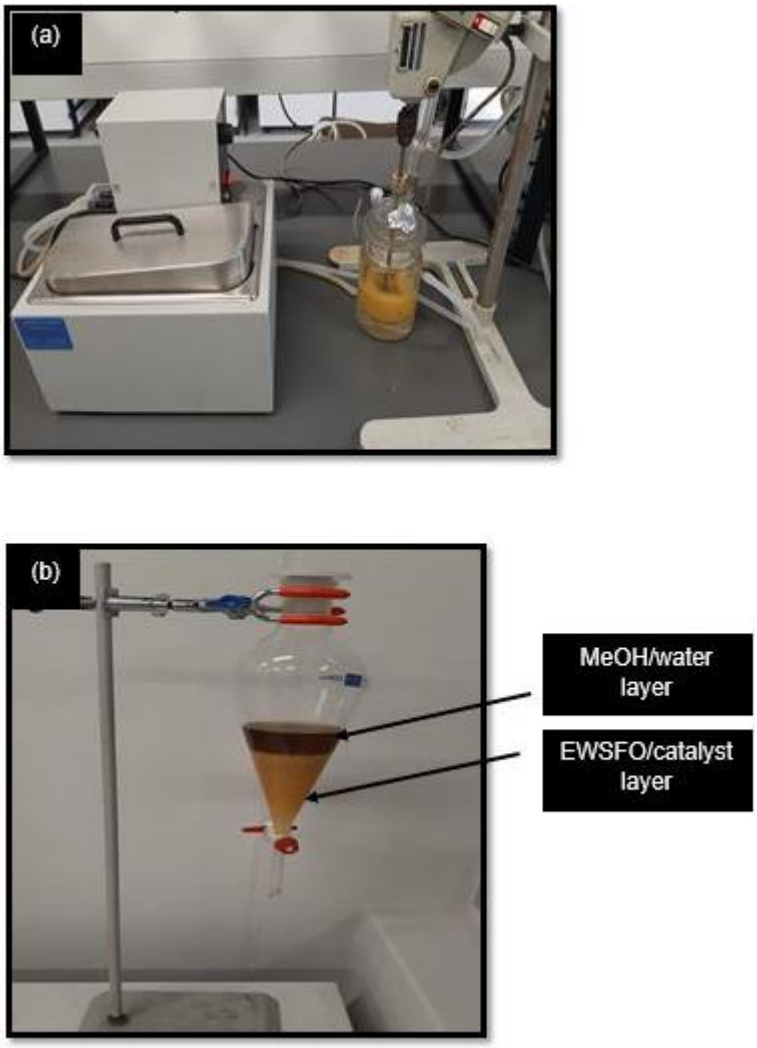

Figure 3.2: (a) Set-up of esterification of WSFO; (b) Separation step

3.4.5 Phase 1 experiments

3.4.5.1 Synthesis of biomass-derived solid base catalysts

A. Biomass catalyst derived from banana peels (BP)

The collected banana peels used in this study were washed thrice with distilled water and diced in order to speed up the drying process. The diced banana peels were dried in a hot air oven for 48 hours at 80°C. After drying, the peels were ashed through burning in open air and manually milled to powder using a porcelain mortar and pestle. The diced banana peels ash was sieved using a sieve shaker (LABOTEC) to obtain fine ash. The fine ash (size range of 150-38 µm) was calcined at different temperatures namely: 200 °C, 400 °C and 600 °C for 4 hrs in the furnace (Labofurn EMF 260). After calcination at each temperature, the obtained calcined banana peels ash (CBPA) was cooled in a desiccator and then stored in an air-tight container until further elemental composition analysis. The elemental composition of CBPA at each temperature was determined using energy dispersive x-ray spectroscopy (EDS) analysis and was used to identify the optimum calcination temperature of CBPA synthesized in this study. Thereafter, mass production of CBPA (approximately 196 g) took place at optimum calcination temperature and the synthesized CBPA was stored for further use.

B. Biomass catalyst derived from chicken eggshells (CES)

The collected chicken eggshells used in this study were firstly cleaned by removing the shell membrane (which is a clear film lining) attached to the eggshells. Then, the chicken eggshells (CES) were rinsed thoroughly with tap water followed by double rinsing with distilled water. The chicken eggshells were dried in a hot air oven for 72 hours at 70°C. The dried chicken eggshells were grinded to powder using a porcelain mortar and pestle. The chicken eggshell powder was sieved using a sieve shaker (LABOTEC) to obtain fine powder (size range of 150-38 µm). The fine chicken eggshells powder was calcined in the furnace at different temperatures namely: 200 °C, 400 °C, 600 °C, 800 °C, and 1000 °C for 4 hrs. After calcination, the calcined chicken eggshell powder (CCESP) obtained at each temperature was cooled in a desiccator and stored in an air-tight container until further analysis. The elemental composition of CCESP at each temperature was determined using energy dispersive x-ray spectroscopy (EDS) analysis and its optimum calcination temperature was identified. Thereafter, mass production of CCESP (approximately 124 g) took place at the optimum calcination temperature and the synthesized CCESP was stored for further use.

C. Biomass catalysts derived from cocoa pod husks (CPH) and enterolobium cyclocarpum pod husks (ECPH)

The collected cocoa pod husks (CPH) and enterolobium cyclocarpum pod husks (ECPH) used in this study were washed with tapped water, diced and sun-dried for 2 weeks until a fixed weight was obtained. The dried CPH and dried ECPH were separately ashed through burning in open air and milled manually to powder using a porcelain mortar and pestle. Thereafter, the CPH ash and ECPH ash were sieved one at a time using a sieve shaker (LABOTEC) to obtain fine ash (size range of 150-38 µm). The fine ash of each biomass was calcined at different temperatures namely: 200 °C, 400 °C, 600 °C, 800 °C and 1000 °C for 4 hrs in the furnace (Labofurn EMF 260). After the calcination process, the calcined ashes of each biomass, specifically calcined cocoa pod husks ash (CCPHA) and calcined enterolobium cyclocarpum pod husks ash (CECPHA), obtained at each temperature were cooled in a desiccator and stored in air-tight containers for further EDS analysis. The respective elemental composition of each calcined biomass ash was determined and their optimum calcination temperatures were identified. Thereafter, mass production (approximately 118 g of CCPHA and 100 g of CECPHA) took place for each catalyst separately at their corresponding optimum calcination temperature and the synthesized biomass catalysts were stored appropriately till further use.

3.4.5.2 Characterizations of biomass-derived solid base catalysts using SEM/EDS, FTIR and XRD

The surface morphology of the biomass-derived solid base catalysts (derived from BP, CPH and ECPH) was examined at 20 kV and at 20 000x magnification using scanning electron microscope (FEI Nova NanoSEM 230) with a field emission gun. Due to unavailability of the FEI Nova NanoSEM 230, the morphology of biomass catalyst derived from CES was examined using a different microscope. The surface morphology of the biomass catalyst derived from CES was examined at 5 kV and at 13.8 000x magnification using scanning electron microscope (MIRA3 TESCAN RISE SEM). The elemental composition analysis of the biomass-derived solid base catalysts was determined at 10 kV using energy dispersive spectroscopy (EDS) (Oxford X-Max 20mm^2 detector along with Oxford Inca Software). It ought to be noticed that an average of the triplicate data acquired at various sites on each of the samples microstructures was accounted for as their respective elemental compositions. The active functional groups existent in the raw, burnt and calcined samples of the biomass-derived solid base catalysts were determined by performing a Fourier transform infrared (FTIR) analysis using a Perkin Elmer UATR Two spectrometer in the wavenumber range in the region of 4000-400 cm^{-1}. For

identification of the crystalline phases present in the biomass-derived solid base catalysts, search and match software was used. X-ray diffraction patterns of the raw, burnt and calcined samples were recorded on a BRUKER AXS (Germany) D8 Advance X-ray diffractometer (XRD) coupled with Lynx Eye position sensitive detector (PSD) using Cu-Kα radiation tube (λ $K\alpha_1$=1.5406Å) over a 2θ range from 0.5° to 130° with an average increment of 0.034° at an average measurement time of 0.5 seconds per step.

3.4.5.3 Transesterification in the batch reactor

The batch reactor set-up used in section 3.4.4 was also used for the phase 1 transesterification reactions. 77.5 mL of esterified waste sunflower oil (EWSFO) was measured and dispensed into the 500-mL four neck square bottom jacketed glass reactor and 62 mL of methanol (MeOH) was added. Thereafter, the mixture of EWSFO-MeOH was allowed to mix for a period of 5 min. The reaction temperature was kept constant at 65°C throughout the duration of the process. 3.10 g of biomass-derived solid base catalyst (i.e. either CBPA, CCESP, CCPHA or CECPHA) was added to the mixture of EWSFO-MeOH and the reaction ended after 65 min elapsed. The various sections of the reaction product were separated by gravity using a separating funnel and allowed to stand under gravity for 24 hrs. The resulting reaction mixture separated into three layers: waste sunflower methyl esters (WSFME)/unreacted methanol layer (top), glycerol/water layer (middle) and catalyst layer (bottom) as illustrated in Figure 3.3. The middle and bottom layers of the resulting reaction mixture were decanted one at a time. The WSFME/unreacted methanol layer was decanted into a beaker and unreacted methanol was removed by heating. The cooled WSFME was poured into the separating funnel and washed thrice with distilled water at 50 °C to remove any residual catalyst, soap and glycerol. Sodium sulfate was used to further dry the purified WSFME. Equation (3.12) was used to calculate the WSFME yield.

$$\text{WSFME yield (wt.\%)} = \frac{\text{Weight of WSFME produced (g)}}{\text{Weight of EWSFO used (g)}} \text{ x } 100 \qquad (3.12)$$

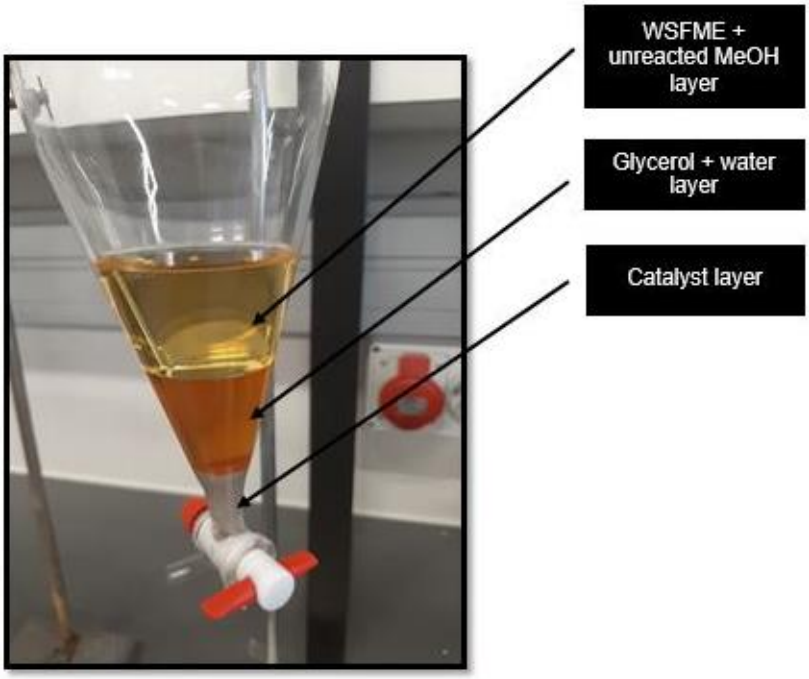

Figure 3.3: Separation by gravity of the CBPA-catalyzed transesterification reaction product

3.4.5.4 Determination of properties of WSFME produced in phase 1

The physicochemical and fuel properties of WSFME produced in phase 1 of this study, which were investigated to determine its quality include kinematic viscosity at 40°C, specific gravity (SG) at 25°C, acid value (AV) and American petroleum index (API). The WSFME produced in phase 1 of this study using the selected biomass-derived solid base catalysts are illustrated in Figure 3.4.

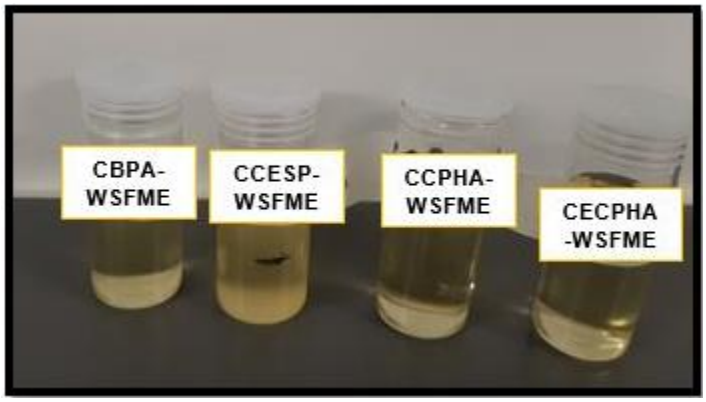

Figure 3.4: WSFME produced during phase 1 of the study

The kinematic viscosity of the WSFME produced in phase 1 of this study was determined using Equation (3.1) as described in section 3.4.2.1.

The specific gravity (SG) of the WSFME produced in phase 1 of this study was experimentally determined using a Bomex pycnometer following the same procedure described in section 3.4.2.2.

The acid value (AV) of WSFME produced in phase 1 of this study was experimentally determined using a standard AOAC method following the same procedure described in section 3.4.2.3.

The American petroleum index (API) of the WSFME produced in phase 1 of this study was determined using Equation (3.9) shown in section 3.4.2.10.

3.4.6 Phase 2 experiments

3.4.6.1 Preparation of the supported biomass-derived solid base catalyst (CECPHA-Pumice)

Firstly, pumice granules (catalyst support) were dehydrated in an oven at 120 ºC for 3 hours. Thereafter, the pumice granules were impregnated with a 1-M solution of CECPHA for 24 hours at ratio of 0.6 (w/v) in order to create CECPHA sites (basic sites) in the pumice granules. The pumice granules were dried again in an oven at 120 ºC for another 3 hours. The resulting product, CECPHA-Pumice, was then kept in a tightly sealed desiccator for analysis and further use. This procedure has been described elsewhere for KOH supported on pumice (K-pumice) (Borges & Díaz, 2013).

3.4.6.2 Characterizations of supported biomass-derived solid base catalyst (CECPHA-Pumice) and support (pumice) using SEM/EDS, FTIR, XRD and BET/BJH

The surface morphology of CECPHA-pumice and pumice samples was examined at 5 kV and at 500 x magnification using scanning electron microscope (MIRA 3 TESCAN RISE SEM). The elemental composition of CECPHA-pumice and pumice samples was obtained using EDS (FEI Nova NanoSEM 230 equipped with Oxford X-Max 20mm^2 detector) at 20 kV. The active functional groups in the CECPHA-Pumice and in the pumice were identified by FTIR (Perkin Elmer UATR Two spectrometer) in the wavenumber range of 4000-400 cm^{-1}, while the crystalline phases in the samples were determined by XRD analysis. The textural properties of CECPHA-pumice and pumice were obtained by N_2 sorption isotherms method at 77.350 K

using Micromeritics instrument ASAP 2020 V4.03 (USA). Prior to sorption measurements, the samples were degassed at 200°C overnight to eliminate moisture and atmospheric vapours. The surface area of CECPHA-pumice and pumice was determined using the BET method, while their respective pore distribution was obtained using the BJH equation.

3.4.6.3 Experimental determination of the density of CECPHA-Pumice

The density of CECPHA-pumice catalyst used in this study was experimentally determined using the buoyancy technique. The volume occupied by 1 g of CECPHA-Pumice was found by pouring a known volume (3 mL) of solvent (absolute ethanol) into a measuring cylinder and then adding 1 g of CECPHA-Pumice to it. The volume occupied by 1 g of CECPHA-Pumice was obtained by subtracting the volume of the solvent + CECPHA-Pumice by the volume of the solvent. The density of CECPHA-Pumice was calculated by Equation (3.13)

$$\text{Density of CECPHA} - \text{Pumice } (\text{g.cm}^{-3}) = \frac{\text{mass of CECPHA} - \text{Pumice (g)}}{\text{Volume of CECPHA} - \text{Pumice } (\text{cm}^3)} \quad (3.13)$$

3.4.6.4 Transesterification in the continuous reactor

The continuous transesterification reactions of phase 2 were performed in a fixed packed bed reactor (PBR) at atmospheric pressure. The fixed PBR scheme and set-up can be seen in Figures 3.5 and 3.6 respectively. The reactor was composed of a water-jacketed glass column with an inner diameter of 85 mm and a total height of 615 mm. The inside of the column had a fitted in 12 mm (inner diameter) tube which was moveable to adjust the bed height. The column was packed with 253 g of CECPHA-Pumice catalyst (which had density of 1.32 g/cm^3) corresponding to a bed height of approximately 8.4 cm. Both the bottom section of the column's inner tube and the bottom section of the column had a sinter disk of 40-100 µm that kept the catalyst from escaping the reactor. 496 mL of EWSFO, 446 mL of methanol and 339 mL of n-hexane (co-solvent) were loaded to the 1.3L feedstock tank fitted with an overhead stirrer and a condenser. The reactants were mixed at a speed of 700 rpm and pre-heated to the same temperature of the PBR, then were fed to the inlet (bottom part) of the reactor using a peristaltic pump set at the desired flowrate. The temperature of the reaction was controlled by a thermostat water bath that was kept at the constant desired temperature with an error of ± 2.0 °C. Sampling began, once the PBR reached steady-state (SS) conditions. Based on literature, the SS for the fixed PBR was assumed to be reached after three residence times. The SS was

verified by withdrawing 3 samples at different times after the three consecutive residence times elapsed. Thereafter, at every hour of reaction time, two consecutive samples of 20 mL of effluent solution from the outlet (top part) of the reactor were collected from the accumulation tank. The collected samples were analysed by GC-FID for the composition measurement. The WSFME yield in each experiment (equal to the conversion of WSFO, when selectivity of the reaction was considered to be a unit) was calculated based on its content in the effluent solution. For initial rate of reaction experiments the temperature was kept constant at 55°C while varying the feed flow rate, specifically 1.6 mL/min, 2.1 mL/min, 3 mL/min and 4 mL/min. For the kinetic parameters experiments the flow rate was kept constant at 1.6 mL/min while varying the reaction temperature, specifically 40°C, 50°C, 55°C and 60°C.

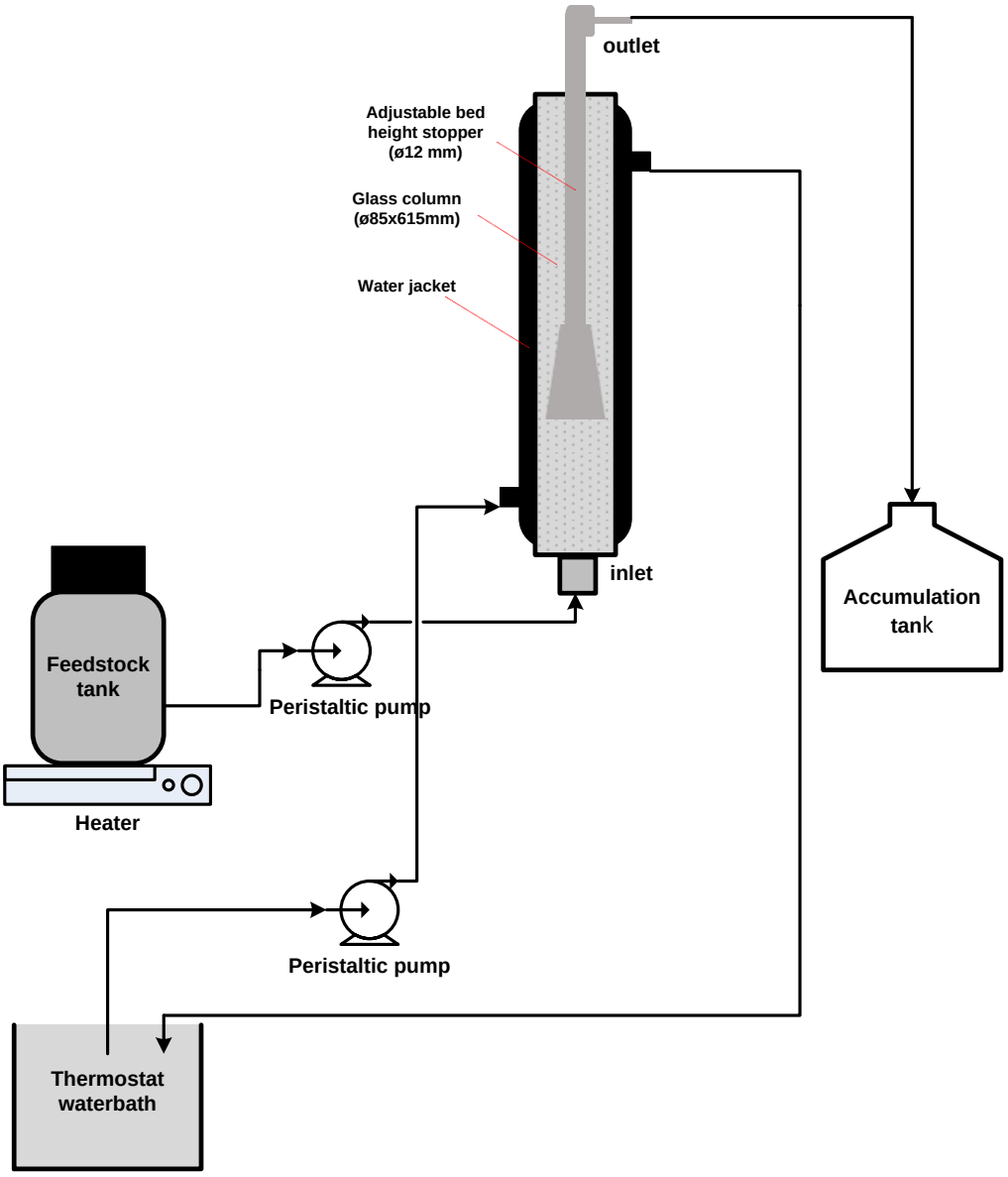

Figure 3.5: Continuous transesterification reaction scheme

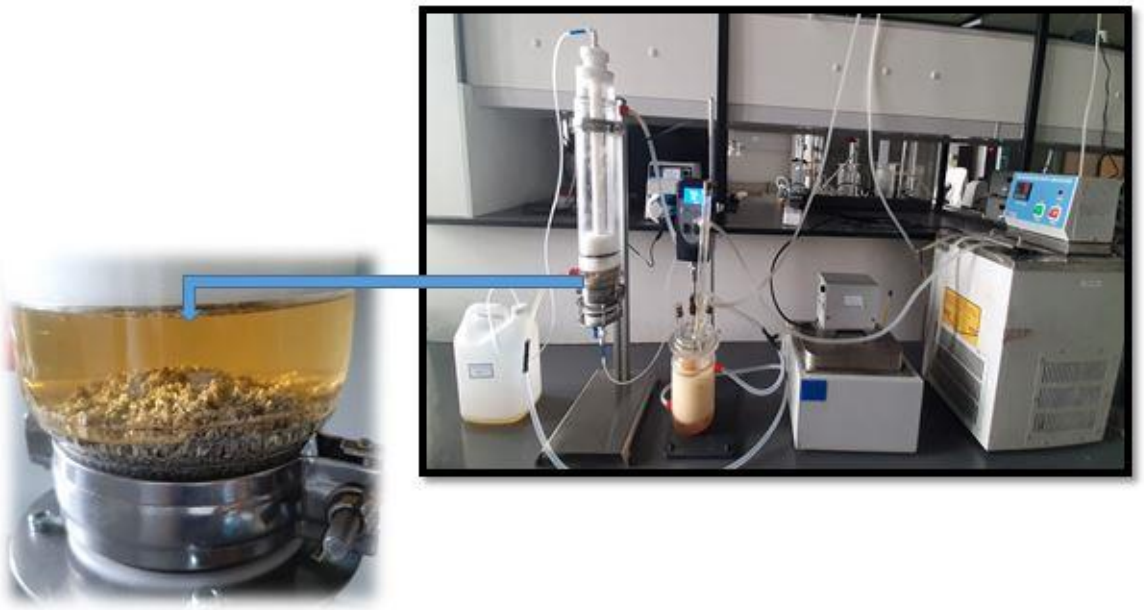

Figure 3.6: Continuous transesterification set-up used in this study

3.4.6.5 Determination of properties of WSFME produced in phase 2

The physicochemical and fuel properties of WSFME produced in phase 2 of this study, specifically kinematic viscosity at 40 °C, density at 20 °C, acid value (AV), calorific value, moisture content and sulphur content were characterized to determine its quality. The WSFME produced in phase 2 of this study using the CECPHA-Pumice as supported biomass-derived solid base catalyst is illustrated in Figure 3.7.

Figure 3.7: WSFME produced during phase 2 of the study

The WSFME produced in phase 2 of the study was analysed using standard ASTM procedures. Kinematic viscosity at 40 °C and density at 20 °C were determined using ASTM D445 and ASTM D4052 respectively. The acid value and calorific value were determined using ASTM D664 and ASTM D240 respectively. Moisture content and sulphur content were determined using ASTM D6304 and ASTM D7039 respectively.

The fatty acid composition of the WSFME produced in phase 2 of this study was analyzed using GC-FID (Agilent 7890A). The GC column dimensions as well as analysis conditions were previously described in section 3.4.3

CHAPTER 4
RESULTS AND DISCUSSION OF BIODIESEL PRODUCTION

4.1 Introduction

This chapter firstly presents the results of the investigated physicochemical and fuel properties of the feedstock (WSFO) used in this study as well as its fatty acid profile (section 4.2). The findings of the WSFO pre-treatment process are also discussed in this chapter (section 4.3). The chapter also presents the phase 1 results, which include the characterization results of the biomass-derived solid base catalysts (section 4.4.1) and the results of the performance of the biomass-derived solid base catalysts in the batch reactor (section 4.4.2). Finally, the phase 2 results which include the characterization results of the supported biomass-derived solid base catalyst (CECPHA-Pumice) (section 4.5.1) and the characterization results of the waste sunflower methyl esters (WSFME) produced during phase 2 (section 4.5.2) are also reported in this chapter. The results discussed herein stem from the experimental procedures described in chapter 3 under section 3.4.

4.2 Waste sunflower oil (WSFO) results

Table 4.1: Properties of WSFO used in this study

Properties	Value
Physical state and colour at room temperature	Liquid/Light orange
Kinematic viscosity (mm^2/s) at 40 °C	35.15
Specific gravity at 25 °C	0.921
Acid value (mg KOH/g oil)	5.16 ± 0.32
%Free fatty acid	2.59 ± 0.16
Saponification value (mg KOH/g)	156.38 ± 0.70
Iodine value (g I_2/ 100g oil)	93.96 ± 0.24
Peroxide value (meq O_2/kg oil)	0.1 ± 0.008
Moisture content (%)	0.0033 ± 0.0002
Cetane number (CN)	60.06
Diesel Index (DI)	36.04
Aniline point (AP) (°F)	160.89

American Petroleum index (API)	22.40
HHV (MJ/kg)	41.60
Fatty acid profile Fatty acids (wt. %) *Saturated FAs* Palmitic (C16:0) Stearic (C18:0) *Mono-unsaturated FAs* Palmitoleic (C16:1) Oleic (C18:1) *Poly-unsaturated FAs* Linoleic (C18:2)	 8.51 4.28 8.52 29.16 49.53

Figure 4.1: WSFO used in this study

The physicochemical and fuel properties as well as fatty acid profile of WSFO used in this study are presented in Table 4.1. The physical state and colour at room temperature of the WSFO used in this study is shown in Figure 4.1. The kinematic viscosity at 40 °C of WSFO was found to be 35.15 mm^2/s, which was relatively higher than the value of 9.5 mm^2/s reported by Hossain and Boyce (2009). The specific gravity at 25 °C of WSFO was found to be 0.921 and it was within the literature reported range of 0.91-0.92 (Udeh, 2017; Awogbemi et. al, 2019). The acid value (AV) and %FFA of the WSFO were found to be 5.16 mg KOH/g oil and 2.59% respectively. These values were marginal to the values of 2.29 mg KOH/g oil and 1.15%

reported by Awogbemi et al. (2019). The AV and % FFA values for the WSFO used in this study are beyond the acceptable limit for alkali-catalyzed transesterification. This indicates that WSFO required pre-treatment (esterification) with an acid catalyst before it could be used for biodiesel production. The HHV for WSFO was found to be 41.60 MJ/kg, a marginal value of 37.90 MJ/kg was reported by Pavani et al. (2015). The WSFO used in this study was composed of 8.51 wt. % of palmitic acid (C16:0), 8.52 wt. % of palmitoleic acid (C16:1), 4.28 wt. % of stearic acid (C18:0), 29.16 wt. % of oleic acid (C18:1) and 49.53 wt. % of linoleic acid (C18:2). Hellier et al. (2015) reported that sunflower oil contains 49-57% linoleic acid and 14-40% oleic acid.

4.3 WSFO pre-treatment results

Table 4.2: Pre-treatment results

Parameters	Values
Catalyst loading (wt. %)	3
Methanol to oil molar ratio	9:1
Reaction time (min)	40
Reaction temperature (°C)	65
Average reduction of AV (%)	81.64 ± 0.68

The results of pre-treatment with ferric sulfate [$Fe_2 (SO_4)_3$] via esterification process of WSFO used in this study are shown in Table 4.2. The operating process conditions used to pre-treat the WSFO used in this study were the optimum conditions reported by Ogaga Ighose et al. (2017) when ferric sulfate was used to pre-treat Thevetia peruviana seed oil (TPSO). After pre-treatment, the acid value of WSFO reduced by an average of 81.64 % ± 0.68, demonstrating that the set of operating process conditions chosen was appropriate for pre-treating the WSFO used in this study. Thus, this set of operating process conditions was employed throughout this study prior to phase 1 and phase 2 experiments. Different studies have reported the use

of ferric sulfate as solid acid catalyst to pre-treat other high acid value vegetable oils prior to alkali-catalyzed transesterification reaction (Gan et al., 2010; Patil et al., 2010; Betiku et al., 2016). Due to its recoverability and reusability, ferric sulfate [$Fe_2(SO_4)_3$] has been proven to be a cost-effective catalyst and to some extent less harmful to the environment compared to other homogenous acid catalysts such as sulfuric acid (H_2SO_4). For these reasons it was the preferred solid acid catalyst for this study.

4.4 Phase 1 results and discussion

4.4.1 Biomass-derived solid base catalysts

4.4.1.1 Scanning electron microscopy (SEM)

4.4.1.1.1 Biomass catalyst derived from BP

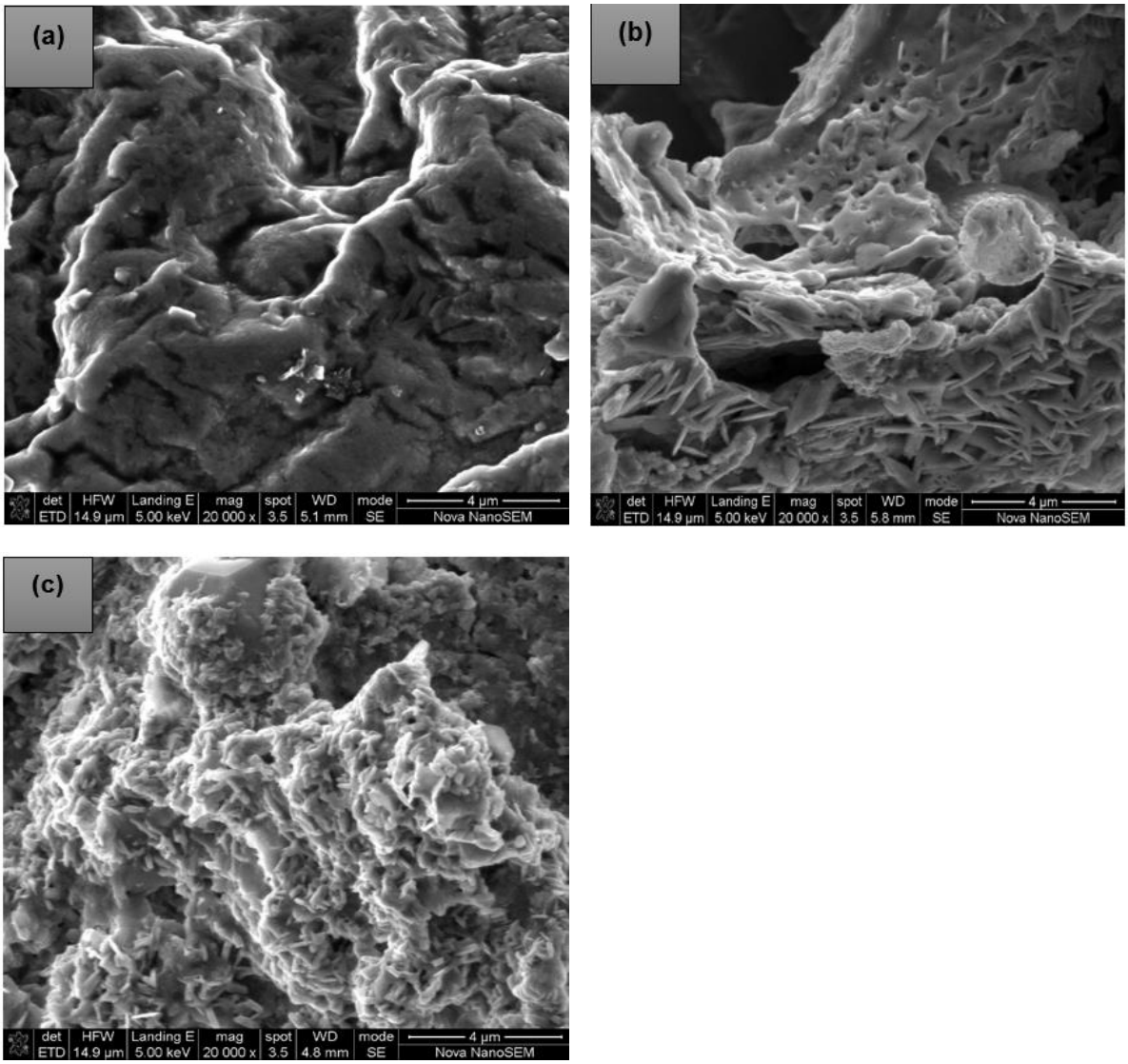

Figure 4.2: SEM images of (a) raw BP, (b) open air burnt BP and (c) CBPA at 600 °C

The morphologies of the raw BP, open air burnt BP and CBPA samples are shown in Figure 4.2. The microstructures for raw BP (Fig 4.2 (a)) and open air burnt BP (Fig 4.2(b)) showed the permeable nature of the particles in these samples. The CBPA sample (Fig 4.2(c)), on the other hand, showed an agglomerate of porous and more crystalline particles of sharp edges, indicative of a higher surface area compared to the raw and open air burnt BP. Analogous morphological observations were reported by Betiku et al. (2016).

4.4.1.1.2 Biomass catalyst derived from CES

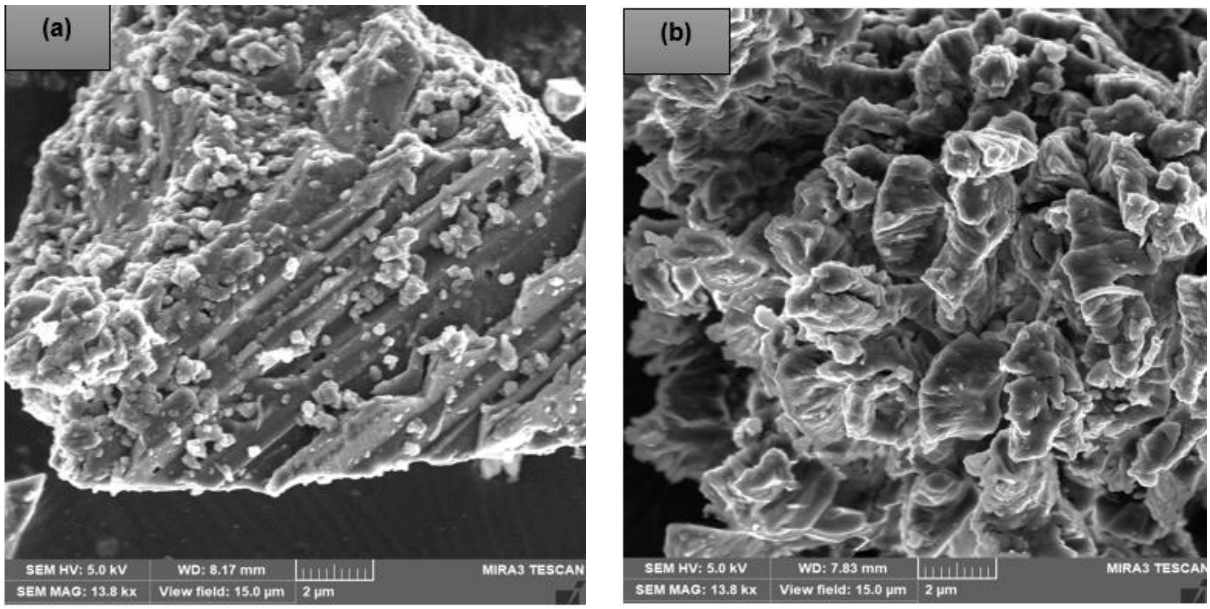

Figure 4.3: SEM images of (a) raw CES and (b) CCESP at 800 °C

The morphologies of the raw CES and CCESP at 800 °C are shown in Figure 4.3. The raw CES (Fig. 4.3 (a)), displays an irregular shape microstructure due to the different sizes and shapes of the particles in this sample. Buasri et al. (2013) reported similar morphological observations for raw chicken eggshells. On the other hand, the CCESP at 800 °C (Fig. 4.3(b)) consists of interlinked smaller size particles and aggregates, which offer higher specific surface areas, resembling a skeleton arrangement.

4.4.1.1.3 Biomass catalyst derived from CPH

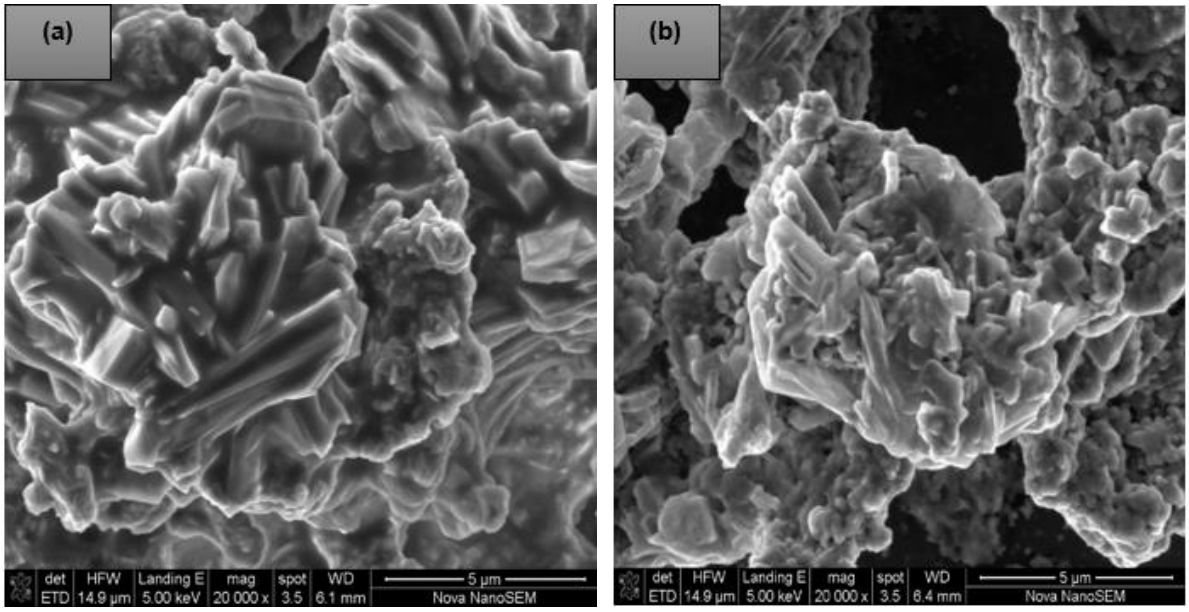

Figure 4.4: SEM images of (a) open air burnt CPH and (b) CCPHA at 600 °C

The morphologies of the open air burnt CPH and CCPHA are illustrated in Figure 4.4. The open air burnt CPH (Fig 4.4(a)) is made of small groups of microstructures displaying a silken and porous nature. Whereas the CCPHA (Fig 4.4(b)) resulted into a stringy microstructure. Despite the fact that CCPHA is porous to some extent, its stringy nature will certainly increase its surface area which consequently result in higher activity (Betiku et al., 2017).

4.4.1.1.4 Biomass catalyst derived from ECPH

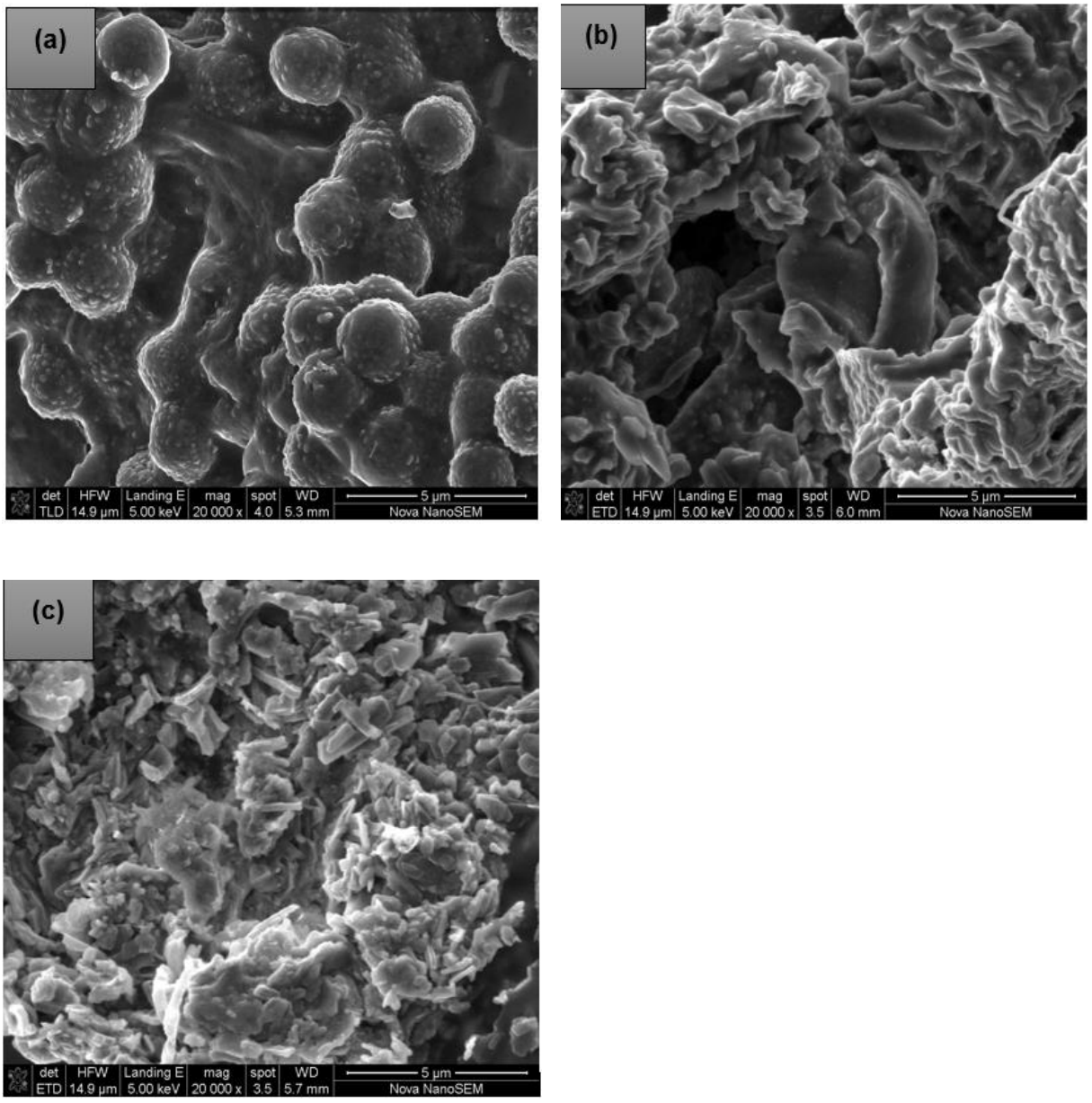

Figure 4.5: SEM images of (a) raw ECPH, (b) open air burnt ECPH and (c) CECPHA at 600 °C

The morphologies of the raw ECPH, open air burnt ECPH and CECPHA samples are shown in Figure 4.5. The raw ECPH (Fig. 4.5 (a)) is made of clumped together porous particles. The open air burnt ECPH (Fig. 4.5 (b)) is constituted by small agglomerated microstructures of silken-flat and porous nature. On the other hand, CECPHA (Fig. 4.5 (c)) reveals a stringy-like nature microstructure, porous to a certain extent, nonetheless with an increased surface area compared to the other two, resulting in a higher activity (Betiku et al., 2017).

4.4.1.2 Energy dispersive x-ray spectroscopy (EDS)

The purpose of using EDS analysis in this study was to identify key metallic elements present in each of the biomass-derived solid base catalysts. More importantly, to understand the effect of calcination temperature on the elemental composition of the biomass-derived solid base catalysts.

4.4.1.2.1 Biomass catalyst derived from BP

Table 4.3: Elemental composition of raw BP, open air burnt BP and CBPA at different temperatures

Sample	Elemental composition (wt. %)					
	K	O	Cl	Si	P	S
Raw BP	12.41 ± 1.91	86.37 ± 0.56	1.22 ± 1.72	0.00	0.00	0.00
Open air burnt BP	35.33 ± 7.18	53.71 ± 8.47	7.01 ± 4.52	2.85 ± 2.06	0.63 ± 0.89	0.47 ± 0.66
CBPA at 200 °C	39.39 ± 8.53	47.49 ± 8.99	7.43 ± 2.23	4.13 ± 1.17	1.31 ± 0.13	0.25 ± 0.36
CBPA at 400 °C	32.28 ± 5.85	53.80 ± 9.93	7.09 ± 6.41	5.23 ± 3.31	1.23 ± 0.09	0.37 ± 0.52
CBPA at 600 °C	37.60 ± 3.70	45.68 ± 1.40	13.77 ± 4.10	1.82 ± 0.26	1.13 ± 0.25	0.00

Table 4.3 presents the elemental composition of raw BP, open air burnt BP and CBPA calcined at different temperatures. The results showed that potassium (K) was the only metallic element present in the raw BP, open air burnt BP and CBPA samples. Therefore, it is plausible to suggest that it was the active component responsible for the catalytic activity in CBPA. An exponential increase in elemental composition of potassium from the raw BP, open air BP and CBPA can also be noted. Different studies have reported that the calcination treatment

impedes metal leaching (in this case K-leaching) and might also increase the catalyst reusability (Sharma et al., 2012; Betiku et al., 2017). It can be observed that the elemental composition of CBPA was greatly affected by the calcination temperature. The highest weight percentages were obtained at 200 °C and 600 °C. Thus, based on the average potassium (K) content and the standard deviation (i.e., K = 39.39 ± 8.53 wt. % at 200 °C, and K = 37.60 ± 3.70 wt. % at 600 °C), the optimum calcination temperature was found to be 600 °C. Mass production of CBPA was performed at the optimum calcination temperature.

Note: The calcination for this biomass waste did not occur at temperatures higher than 600 °C, i.e. at 800 °C and 1000 °C.

4.4.1.2.2 Biomass catalyst derived from CES

Table 4.4: Elemental composition of raw CES and CCESP at different temperatures

Sample	Elemental composition (wt. %)	
	Ca	O
Raw CES	38.82 ± 3.83	61.18 ± 3.83
CCESP at 200 °C	35.64 ± 5.03	64.36 ± 5.03
CCESP at 400 °C	32.49 ± 2.73	67.51 ± 2.73
CCESP at 600 °C	38.99 ± 3.76	61.01 ± 3.76
CCESP at 800 °C	43.35 ± 7.87	56.65 ± 7.87
CCESP at 1000 °C	36.99 ± 2.05	63.05 ± 2.05

The elemental composition of raw CES and CCESP calcined at different temperatures is presented in Table 4.4. The results showed that calcium (Ca) was the only metallic element present in the raw CES and CCESP samples. Therefore, it is plausible to suggest that it was the active component responsible for the catalytic activity in CCESP. An increase in elemental composition of calcium from the raw CES and CCESP can also be noted. The elemental composition of CCESP was significantly affected by the calcination temperature. The highest weight percentages were obtained at 600 °C and 800 °C. Thus, based on the average Ca

content and the standard deviation (i.e., Ca = 38.99 ± 3.76 wt. % at 600 °C, and Ca = 43.35 ± 7.87 wt. % at 800 °C), the optimum calcination temperature was found to be 800 °C. Mass production of CCESP was carried out at the optimum calcination temperature. However, to further validate the choice of optimum calcination temperature, both CCESP at 600 °C and CCESP at 800 °C were assessed since the content of Ca in these samples varies by a small margin.

- **Colour differences in CES samples**

This section is exceptionally displayed and discussed for the CES biomass waste material to support the choice of the optimum calcination temperature of CES used in this study.

Figure 4.6: Images of (a) raw CES, (b_1) CCESP at 600 °C and (b_2) CCESP at 800 °C

Figure 4.6 illustrates the images of raw CES (a), CCESP at 600 °C (b_1) and CCESP at 800 °C (b_2). The raw CES powder was of light pink shade, calcination of CES at 600 °C produced a dark grey powder, whereas calcination of CES at 800 °C produced a white powder. The transition in colour is indicative of changes in the composition of the samples. The change from light pink to white powder was an indication that more metal oxide, specifically CaO, was formed at a higher calcination temperature (Mohadi et al., 2016). Colour changes in raw chicken eggshells and chicken eggshells calcined at temperature range of 600 °C-1000 °C have also been reported by Mohadi et al. (2016).The colour difference between (b_1) and (b_2) further corroborates the choice of 800°C as the optimum calcination temperature for CES in this study.

4.4.1.2.3 Biomass catalyst derived from CPH

Table 4.5: Elemental composition of open air burnt CPH and CCPHA at different temperatures

Sample	Elemental composition (wt. %)							
	K	Mg	Ca	Na	O	Si	P	S
Open air burnt CPH	32.16 ± 3.15	3.85 ± 0.36	2.82 ± 3.98	0.00	61.16 ± 1.22	0.00	0.00	0.00
CCPHA at 200 °C	41.86 ± 12.19	2.70 ± 1.92	2.93 ± 0.33	0.00	51.57 ± 9.84	0.00	0.51 ± 0.41	0.42 ± 0.59
CCPHA at 400 °C	33.96 ± 8.45	2.10 ± 1.25	7.57 ± 6.50	0.00	56.37 ± 2.68	0.00	0.00	0.00
CCPHA at 600 °C	29.64 ± 3.03	3.11 ± 0.90	5.72 ± 0.98	0.00	57.94 ± 1.37	1.85 ± 2.12	1.13 ± 0.61	0.62 ± 0.01
CCPHA at 800 °C	29.64 ± 0.44	2.94 ± 0.63	3.45 ± 0.55	0.25 ± 0.19	62.15 ± 1.11	1.06 ± 0.24	0.42 ± 0.30	0.08 ± 0.11
CCPHA at 1000 °C	16.09 ± 3.60	3.50 ± 1.11	11.97 ± 3.42	1.62 ± 0.33	56.90 ± 5.05	7.62 ± 1.69	1.61 ± 0.99	0.69 ± 0.98

The elemental composition of open air burnt CPH and CCPHA calcined at different temperatures is illustrated in Table 4.5. It can be seen that there are four existing metal elements in the CCPHA, with potassium being the most predominant one. In another study the

elemental composition of CCPHA was reported to have the highest concentration of potassium (K) amongst other metals (Betiku et al., 2017). Therefore, it is plausible to assume that it is the active component responsible for catalytic activity in CCPHA. Based on the average potassium (K) content and considerably low standard deviation, the optimum calcination temperature was determined to be at 600 °C.

4.4.1.2.4 Biomass catalyst derived from ECPH

Table 4.6: Elemental composition of raw ECPH, open air burnt ECPH and CECPHA at different temperatures

Sample	Elemental composition (wt. %)							
	K	Mg	Ca	Na	O	Si	P	S
Raw ECPH	3.64 ± 0.38	0.11 ± 0.16	0.00	0.00	95.80 ± 0.87	0.14 ± 0.11	0.17 ± 0.24	0.13 ± 0.18
Open air burnt ECPH	36.17 ± 4.14	1.68 ± 2.37	0.00	0.00	59.86 ± 1.36	1.31 ± 1.85	0.98 ± 1.39	0.00
CECPHA at 200 °C	37.96 ± 5.84	2.70 ± 1.97	0.62 ± 0.87	0.00	57.27 ± 2.85	0.00	1.45 ± 1.14	0.00
CECPHA at 400 °C	32.59 ± 4.37	2.13 ± 1.53	0.99 ± 1.40	0.00	58.94 ± 3.46	1.61 ± 2.27	1.94 ± 0.23	1.80 ± 0.69
CECPHA at 600 °C	35.34 ± 3.36	2.92 ± 1.51	3.71 ± 1.50	0.00	54.00 ± 4.28	0.24 ± 0.34	2.52 ± 1.24	1.28 ± 0.51
CECPHA at 800 °C	33.50 ± 6.54	2.92 ± 2.08	2.60 ± 2.20	0.11 ± 0.16	57.84 ± 2.06	0.77 ± 0.65	1.68 ± 0.90	0.58 ± 0.82
CECPHA at 1000 °C	28.99 ± 5.81	6.28 ± 3.97	3.88 ± 1.97	1.31 ± 0.10	54.25 ± 2.31	2.74 ± 0.84	1.73 ± 0.44	0.80 ± 0.80

The elemental composition of raw ECPH, open air burnt ECPH and CECPHA calcined at different temperatures is illustrated in Table 4.6. It can be seen that there are four metallic elements present in the CCPHA, howbeit potassium is the most predominant one. Therefore, it is plausible to assume that it is the active component responsible for catalytic activity in

CECPHA. Based on the average K content and considerably low standard deviation, the optimum calcination temperature was determined to be at 600 °C.

4.4.1.3 Fourier transform infrared (FTIR) spectroscopy

4.4.1.3.1 Biomass catalyst derived from BP

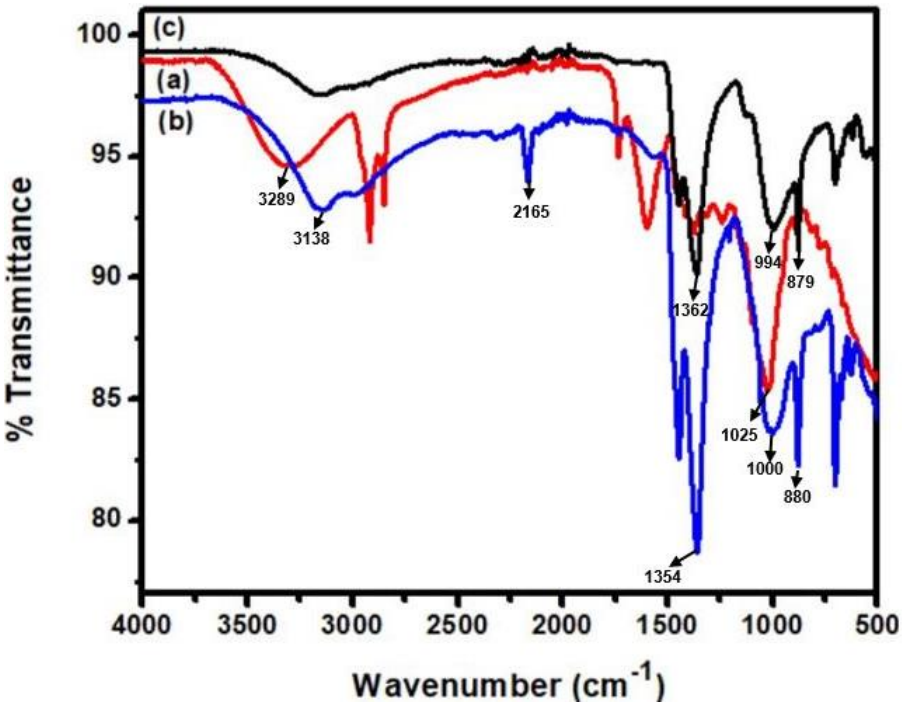

Figure 4.7: FTIR of (a) raw BP, (b) open air burnt BP and (c) CBPA at 600 °C

The FTIR spectra of raw BP, open air burnt BP and CBPA samples showed several adsorption peaks as shown in Figure 4.7. The peaks observed at around 3200-3100 cm^{-1} in raw BP and open air burnt BP samples are attributed to bending and stretching vibrations of O-H bonds due to the presence of H_2O molecules (Sharma et al., 2012). However, as expected the peak was not detected in CBPA sample due to heat treatment at 600 °C. The peak located at 2165 cm^{-1} detected in open air burnt BP sample is assigned to the stretching vibrations of M-O-K bond (where M=Si, Mg, etc.) (Gohain et al., 2017). The bands observed at 1354 cm^{-1} and 1362 cm^{-1} in open air burnt BP and CBPA samples respectively are ascribed to C-O stretching and bending vibrations, which is indicative of the existence of carbonate (CO_3) in these samples (Betiku et al., 2016). The existence of the carbonates in both the open air burnt and CBPA samples is due to the adsorption of atmospheric CO_2 onto metal oxides (Gohain et al., 2017), which may have occurred during open air burning treatment of the BP. The distinctive band at 1362 cm^{-1} prominent in CBPA is indicative of the presence of K_2CO_3 formed due to the

adsorption of atmospheric CO_2 onto K_2O (Sharma et al., 2012 and Betiku et al., 2016). The peaks observed at 1025 cm^{-1}, 1000 cm^{-1} and 994 cm^{-1} in raw BP, open air burnt BP and CBPA samples respectively are assigned to Si-O-Si stretching bands, (Genge et al., 1995; Memon et al., 2008). The Si-O-Si stretching bands were less pronounced in the CBPA compared to the other two samples because of heat treatment at 600 °C. The bands located at 880 cm^{-1} and 879 cm^{-1} observed in the open air burnt BP and CBPA samples respectively were allocated to the secluded vibration of SiO_4 in K_2MgSiO_4 perturbed by interaction with K^+ and Mg^{2+}. An analogous observation has been reported by Betiku et al. (2016), for the secluded vibration of SiO_4 in $CaMgSiO_4$.

4.4.1.3.2 Biomass catalyst derived from CES

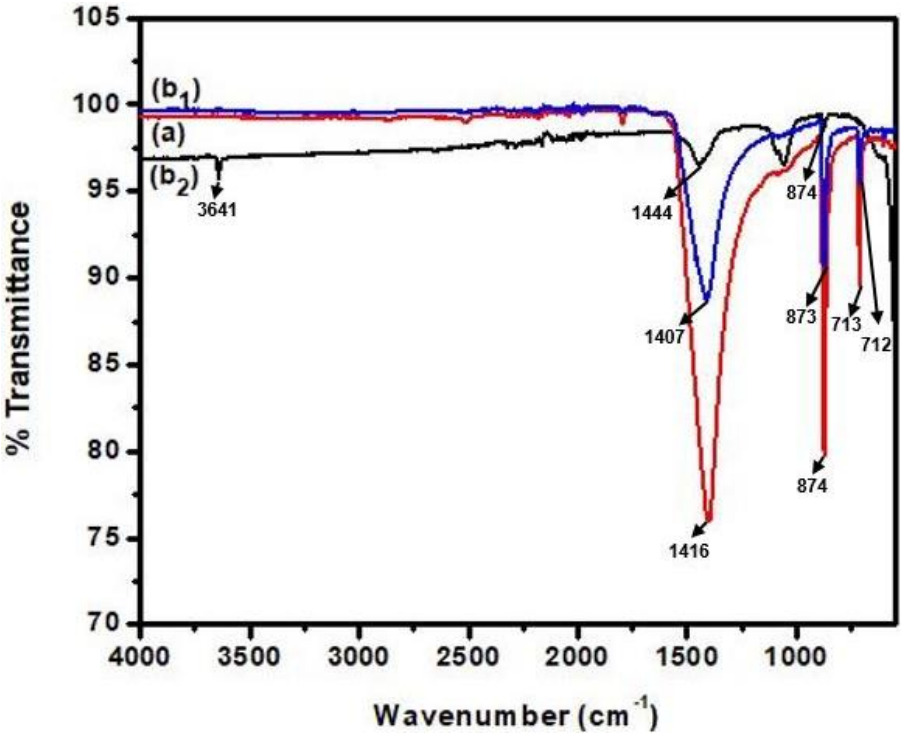

Figure 4.8: FTIR of (a) raw CES, (b_1) CCESP at 600 °C and (b_2) CCESP at 800 °C

The FTIR spectra of raw CES, CCESP at 600 °C and CCESP at 800 °C samples is illustrated in Figure 4.8. The broad stretching peaks observed at 1416 cm^{-1}, 1407 cm^{-1} and 1444 cm^{-1} in raw CES, CCESP at 600 °C and CCESP at 800 °C respectively are ascribed to the C-H bond (Ahmad et al., 2015). The intense and sharp peaks detected at 874 cm^{-1} and 873 cm^{-1} in raw CES and CCESP at 600 °C samples respectively indicate the presence of carboxylate, C-O asymmetric stretching and out- of plane bending vibration modes of CO_3^{2-} of $CaCO_3$ (Nyquist & Kagel , 1971). The peak located at 874 cm^{-1} is also observed in CCESP at 800 °C sample, howbeit at a lower intensity. The reduction in intensity of this peak in the CCESP at 800 °C is

due to loss of carbonate, as $CaCO_3$ is decomposed into CaO (Margaretha et al., 2012). In the case of CCESP at 600 °C, the reduction in intensity of $CaCO_3$ peak is not observed because the calcination temperature of 600 °C was not sufficient to break C-O bond of $CaCO_3$. The sharp peaks located at 713 cm^{-1} and 712 cm^{-1} in raw CES and CCESP at 600 °C samples respectively are attributed to Ca-O bonds (Witoon, 2011; Ahmad et al., 2015). The unique peak located at 3641 cm^{-1} detected in CCESP at 800 °C sample corresponds to O-H stretching vibration and bending of hydroxyl group and is attributed to the OH groups in calcium hydroxide $Ca(OH)_2$ (Roschat et al., 2012 ; Mohammadi et al., 2014). The formation of $Ca(OH)_2$ might have occurred during FTIR analysis as the CCESP at 800 °C sample absorbed atmospheric moisture. The appearance of this peak in CCESP at 800 °C sample agrees with the data reported by Tan et al. (2015).

4.4.1.3.3 Biomass catalyst derived from CPH

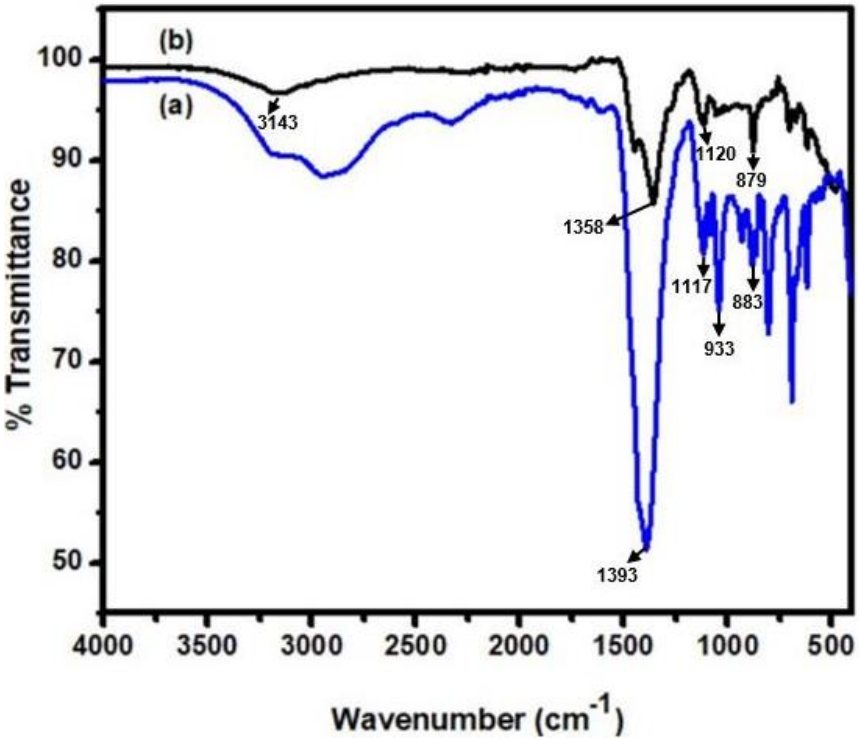

Figure 4.9: FTIR of (a) open air burnt CPH and (b) CCPHA at 600 °C

Figure 4.9 displays the FTIR spectra of open air burnt CPH and CCPHA samples, which show various absorption bands. The weak groups identified in open air burnt CPH and CCPHA at around 3200-3100 cm^{-1} are ascribed to H−OH stretch or Si−OH (Firdaus et al., 2015). The peaks observed at 1393 cm^{-1}, 1117 cm^{-1}, 1358 cm^{-1} and 1120 cm^{-1} in open air burnt CPH and CCPHA samples respectively are attributed to carbonate C−O stretching and bending

vibrations, which proposes the existence of carbonate (Sharma et al., 2012). The band located at 1393 cm^{-1} is characteristic for K_2CO_3 (Betiku et al., 2017; Rachmat et al., 2018). This band is less intense in the CCPHA sample. The decrease in intensity of the K_2CO_3 peak in CCPHA sample was due to heat treatment at 600°C, as K_2CO_3 decomposes into K_2O (Genge et al., 1995; Sharma et al., 2012; Tan et al., 2015). The band situated at 933 cm^{-1} in open air burnt CPH is ascribed to Si−O−Si asymmetric and Si−O−Si symmetric stretching vibration groups (Genge et al., 1995). This band is not detected in CCPHA sample due to heat treatment at 600°C. The peaks located at 883 cm^{-1} and 879 cm^{-1} detected in open air burnt CPH and CCPHA samples respectively were assigned to the secluded vibration of SiO_4 in $CaMgSiO_4$, generated by contact with Ca^{2+} and Mg^{2+} (Betiku et al., 2017).

4.4.1.3.4 Biomass catalyst derived from ECPH

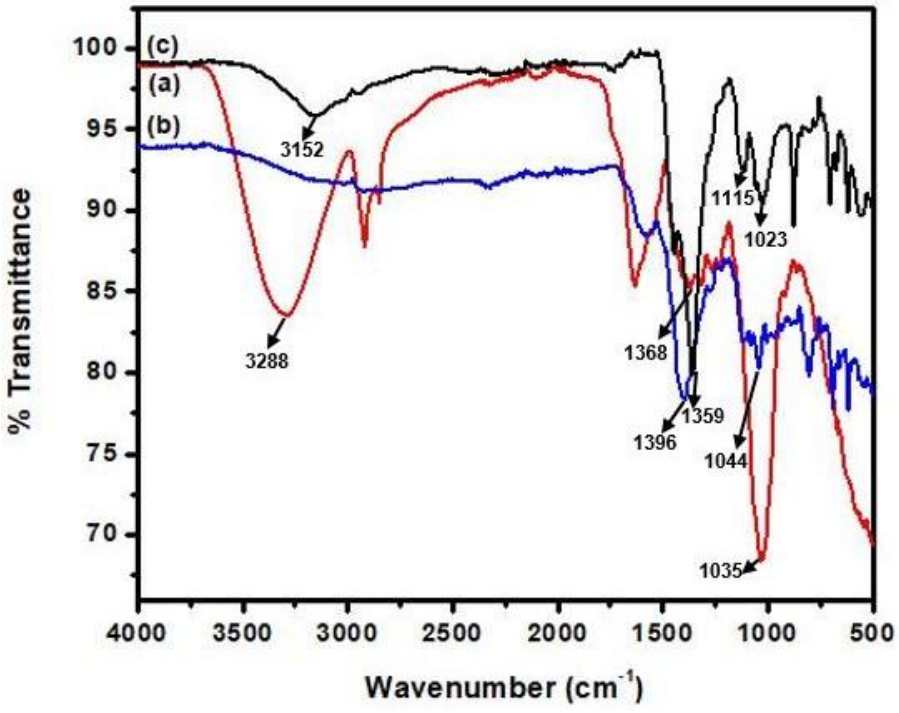

Figure 4.10: FTIR of (a) raw ECPH, (b) open air burnt ECPH and (c) CECPHA at 600 °C

Figure 4.10 displays the FTIR spectra of raw ECPH, open air burnt ECPH and CECPHA, which show various absorption bands. The peaks observed in raw ECPH and CECPHA located at 3288 cm^{-1} and 3152 cm^{-1} respectively are attributed to H−OH stretch or Si−OH (Firdaus et al., 2015). The peaks detected at around 1400-1000 cm^{-1} in all three spectra are accredited to carbonate C−O stretching and bending vibrations, which suggest the existence of carbonates (Sharma et al., 2012). The sharp peak situated at 1359 cm^{-1} in the CECPHA spectrum is distinctive for K_2CO_3 (Betiku et al., 2017; Rachmat et al.,2018).The K_2CO_3 peak appears

broader and sharper at 1396 cm^{-1} in the open air burnt spectrum. Subsequently to calcination at 600 °C, the ECPH loses carbonate due to the decomposition of K_2CO_3 into K_2O, resulting in a decrease in intensity of K_2CO_3 peak in the CECPHA sample (Genge et al., 1995; Sharma et al., 2012; Tan et al., 2015).

4.4.1.4 X-ray diffraction (XRD)

4.4.1.4.1 Biomass catalyst derived from BP

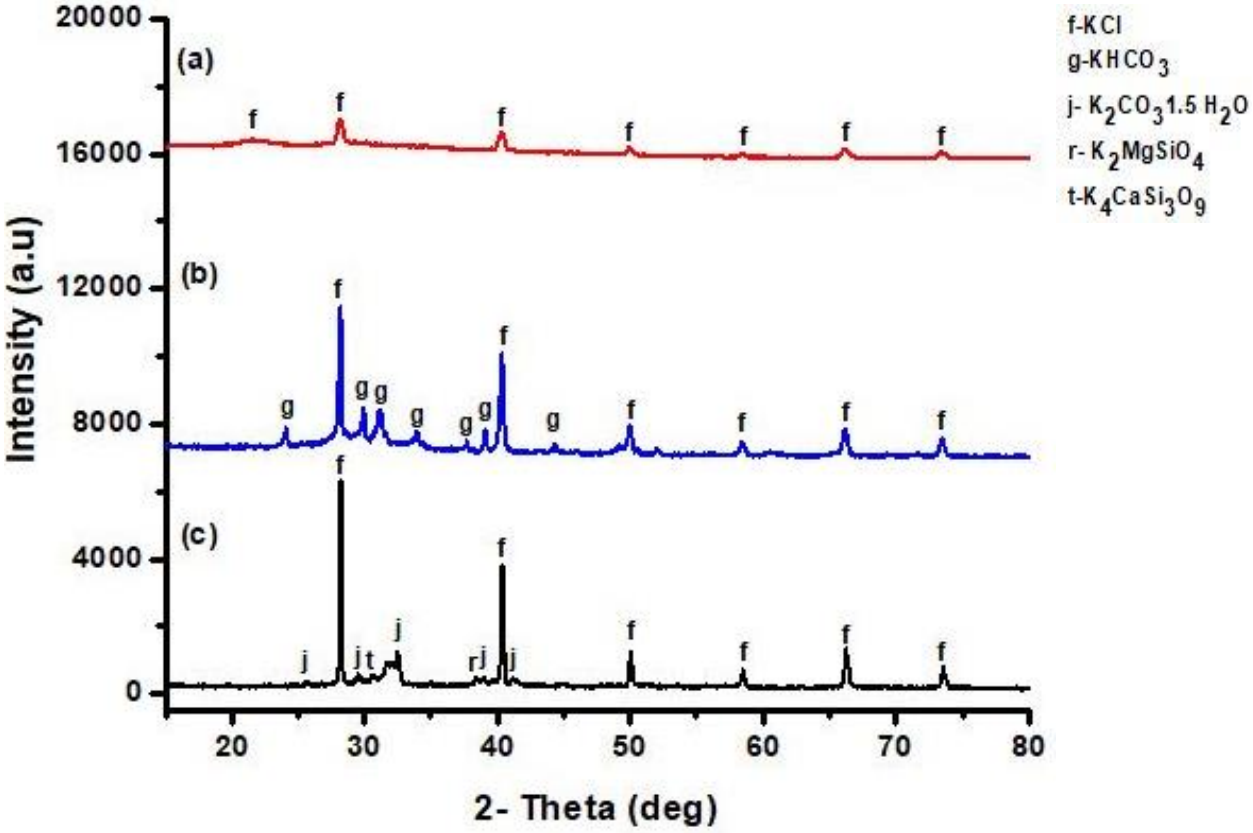

Figure 4.11: XRD of (a) raw BP, (b) open air burnt BP and (c) CBPA at 600 °C

The crystalline phases in raw BP, open air burnt BP and CBPA samples were identified by XRD analysis (Fig. 4.11), wherein a complex mixture of potassium compounds in the form of carbonates, silicates and chlorides was observed. These results were revised along with FTIR results of the detected functional groups in the samples. The raw BP (Fig.4.11(a)) sample displays the XRD pattern with small peaks corresponding to amorphous potassium chloride (KCl) phase (JCPDS card no. 00-041-1476). The open air burnt BP (Fig.4.11(b)) sample shows XRD patterns with sharp peaks indexed to KCl as a major phase and several small broad peaks corresponding to potassium hydrogen carbonate ($KHCO_3$) (JCPDS card no.00-012-0292) as a minor phase. The $KHCO_3$ phase is not detected in the CBPA sample because

$KHCO_3$ starts to decompose at 364 K (120°C) (Hartman et al., 2019). An increase in potassium compounds can be observed after heat treatment at 600°C (Fig. 4.11(c)). Other studies have also reported this trend in catalytic calcined biomass materials (Betiku et al., 2017; Etim et al., 2018). The prominent peaks appearing at 2θ = 28.4˚, 40.5˚, 50.1˚, 58.6˚, 66.2˚ and 73.5˚ in the CBPA sample correspond to KCl phase. The increase in intensity of the peaks is indicative of an increase in the degree of crystallinity of the KCl phase in CBPA sample (Qiu et al.,2010). The CBPA diffractogram also shows small broad peaks appearing at 2θ = 26.1˚, 29.9˚, 32.5˚, 39.9˚ and 41.3˚ corresponding to potassium carbonate sesquihydrate (K_2CO_3.1.5 H_2O) phase (JCPDS card no. 00-011-0655). This corroborates the conspicuous peak at 1362 cm^{-1} (Fig. 4.7(c)) corresponding to K_2CO_3 in $K_2CO_3$1.5H_2O. Due to the high hygroscopicity of K_2CO_3, the carbonate almost immediately changes to sesquihydrate $K_2CO_3$1.5H_2O at contact with air (Gavryushkin et al., 2015). Other small peaks which can be indexed to potassium magnesium silicate (K_2MgSiO_4) (JCPDS card no. 00-039-1426) and potassium calcium silicate ($K_4CaSi_3O_9$) (JCPDS card no. 00-039-1427) as minor phases are also seen in the CBPA diffractogram.

4.4.1.4.2 Biomass catalyst derived from CES

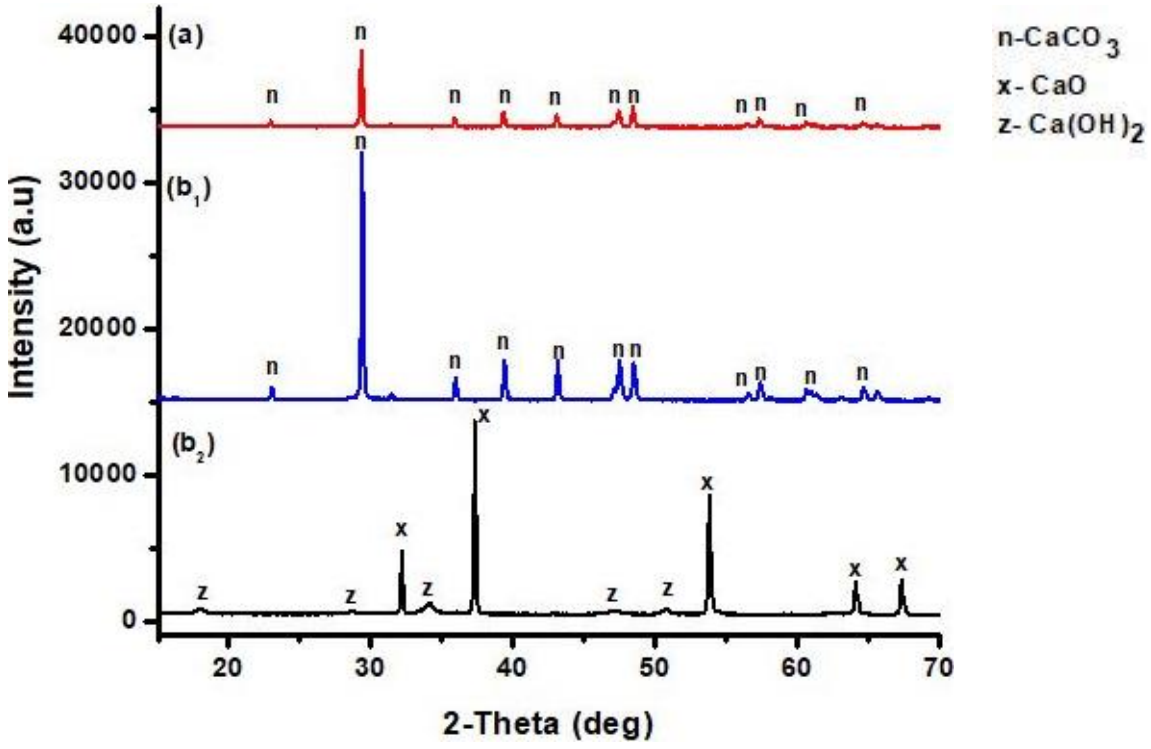

Figure 4.12: XRD of (a) raw CES and (b_1) CCESP at 600 °C and (b_2) CCESP at 800 °C

The x-ray diffraction profile of raw CES, CCESP at 600 °C and CCESP at 800 °C samples is illustrated in Figure 4.12. These results were revised along with FTIR results of the detected functional groups in the samples. Pattern (b_1) is displayed to validate the choice of 800 °C as the optimum calcination temperature for CES. The raw CES (Fig. 4.12 (a)) and CCESP at

600°C (Fig. 4.12 (b_1)), display the XRD pattern that can be indexed to calcium carbonate ($CaCO_3$) phase (JCPDS card no.00-005-0586). The plausible reason for no change in XRD pattern of these samples is the considerably low calcination temperature of 600 °C used, which was not sufficiently high to transform $CaCO_3$ phase into CaO. This can be corroborated by the FTIR spectra of raw CES and CCESP at 600 °C (Fig 4.8 (a) and (b_1)), which show identical peaks in both samples. Viriya-empikul et al. (2010) reported that a high temperature range above 700°C is a requisite to transform $CaCO_3$ to CaO. Wei et al. (2009) also reported that the diffraction patterns of chicken eggshells calcined at temperatures lower than 700 °C were characteristic of $CaCO_3$, while samples calcined at temperatures higher than 700 °C displayed diffraction patterns characteristic of CaO. The CCESP at 800 °C (Fig. 4.12 (b_2)), on the other hand, displays the XRD pattern corresponding to calcium oxide (CaO) (JCPDS card no. 00-037-1497) as a major phase with sharp peaks appearing at 2θ = 32.1˚, 37.5 ˚, 53.9 ˚, 64.1 ˚ and 67.3 ˚. The change in XRD pattern from pattern (a) to pattern (b_2) is caused by the calcination process at such high temperature, which resulted in the total removal of carbon dioxide (CO_2) (Tan et al.,2015). The $CaCO_3$ phase could not be detected in the CCESP at 800°C. Thus, implying that the calcined chicken eggshells were fully crystallized during heat treatment at 800 °C. The CCESP at 800 °C also displays the XRD pattern that can be indexed to calcium hydroxide ($Ca(OH)_2$) (JCPDS card no. 00-004-0733) as a minor phase with small peaks appearing at 2θ = 18.1 ˚, 28.8 ˚, 34.1 ˚,47.3 ˚ and 50.8 ˚. The presence of the $Ca(OH)_2$ phase in CCESP at 800 °C sample corroborates the existence of the peak appearing at 3642 cm^{-1} (Fig. 4.8(b_2)).

4.4.1.4.3 Biomass catalyst derived from CPH

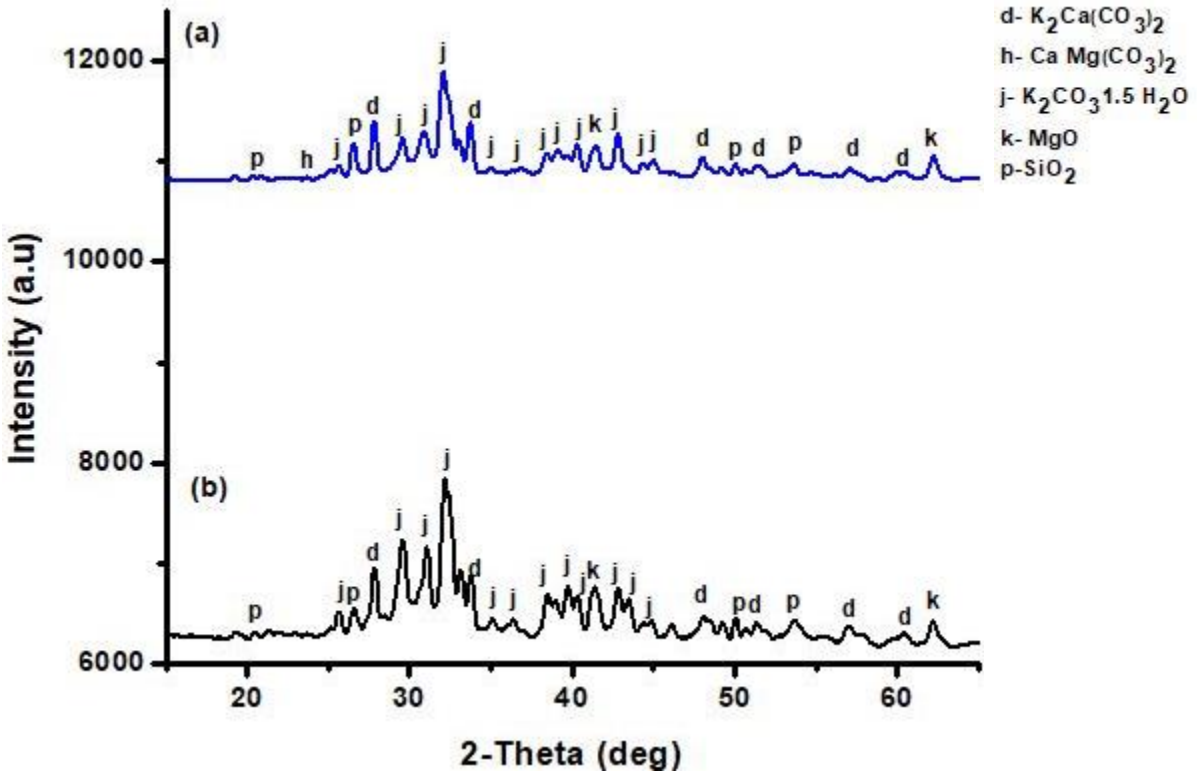

Figure 4.13: XRD of (a) open air burnt CPH and (b) CCPHA at 600 °C

The diffractograms of open air burnt CPH and CCPHA, which show the crystalline compounds present in both samples, are illustrated in Figure 4.13. These results were revised along with FTIR results of the detected functional groups in the samples. The XRD pattern of open air burnt CPH (Fig.4.13(a)) shows several sharp peaks corresponding to potassium carbonate sesquihydrate ($K_2CO_3 \cdot 1.5H_2O$) (JCPDS card no. 00-011-0655) and potassium calcium carbonate ($K_2Ca(CO_3)_2$) (JCPDS card no. 00-021-1287) as major phases and smaller peaks corresponding to magnesium oxide (MgO) (JCPDS card no. 00-045-0946), silicon dioxide (SiO_2) (JCPDS card no. 00-083-0539) and calcium magnesium carbonate ($CaMg(CO_3)_2$) (JCPDS card no. 00-036-0426) as minor phases. The XRD pattern of CCPHA (Fig.4.13(b)) displays peaks appearing at 2θ = 25.1˚, 29.9˚, 32˚, 32.5˚, 35˚, 36.1˚, 38.5˚, 40.2˚, 41.4˚, 43.3˚, 44.5˚ and 45˚ corresponding to $K_2CO_3 \cdot 1.5H_2O$ as a major phase. The increase in intensity of the peaks, which occurs due to heat treatment at 600°C, is indicative of an increase in the degree of crystallinity of the $K_2CO_3 \cdot 1.5H_2O$ phase in CCPHA sample (Qiu et al.,2010).The presence of $K_2CO_3 \cdot 1.5H_2O$ phase validates the predominant peak located at 1358 cm^{-1} corresponding to K_2CO_3 in the spectrum of CCPHA (Fig. 4.9 (b)). A similar observation has also been reported by Betiku et al. (2017). The CCPHA diffractogram also shows small broad peaks appearing at 2θ = 27.9˚, 33.8˚, 48˚, 53.8˚, 56.9˚ and 60.8˚ corresponding to $K_2Ca\ (CO_3)_2$

phase. Other small peaks which can be indexed to MgO and SiO_2 as minor phases are also seen in the CCPHA diffractogram. The presence of SiO_2 phase in CCPHA sample is due to residue of ashes of CPH (Rachmat et al., 2018).

4.4.1.4.4 Biomass catalyst derived from ECPH

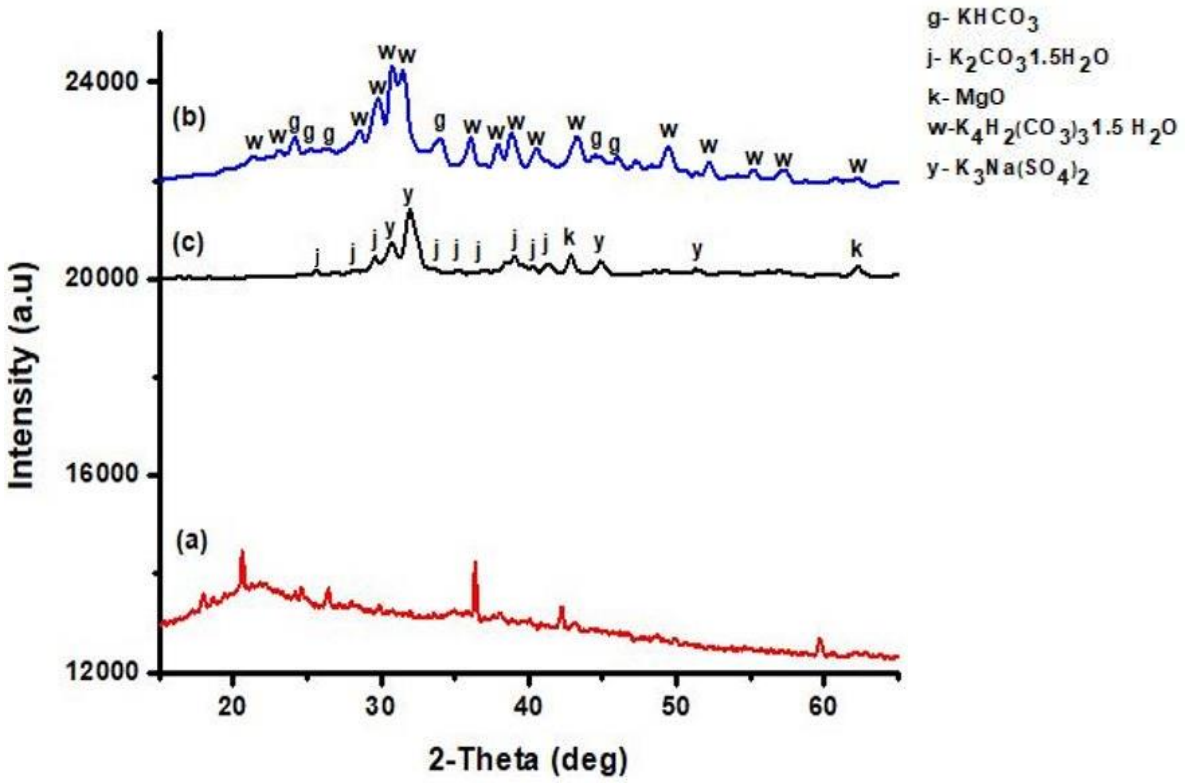

Figure 4.14: XRD of (a) raw ECPH, (b) open air burnt ECPH and (c) CECPHA at 600 °C

The XRD patterns of raw ECPH, open air burnt ECPH and CECPHA, which display the crystalline compounds existent in the samples, are shown in Figure 4.14. These results were revised along with FTIR results of the detected functional groups. The open air burnt ECPH (Fig. 4.14(b)) shows a number of sharp peaks corresponding to potassium hydrogen carbonate hydrate ($K_4H_2(CO_3)_3 1.5H_2O$) (JCPDS card no. 00-020-0886) as a major phase and smaller peaks corresponding to potassium hydrogen carbonate ($KHCO_3$) (JCPDS card no.01-073-2155) as a minor phase. The XRD pattern of CECPHA (Fig. 4.14(c)) displays peaks appearing at 2θ = 25.8˚, 28.2˚, 29.8˚, 33.9˚, 35˚, 38.5˚, 39.8˚, 40˚ and 41.1˚corresponding to potassium carbonate sesquihydrate ($K_2CO_3 \cdot 1.5H_2O$) (JCPDS card no. 00-011-0655) and peaks appearing at 2θ = 30.9˚, 31.9˚, 44.9˚ and 53.2˚corresponding to tripotassium sodium disulfate ($K_3Na(SO_4)_2$) (JCPDS card no. 00-020-0928) as major phases. Other small peaks which can be indexed to magnesium oxide (MgO) (JCPDS card no. 00-045-0946) as minor phase are also observed in the CECPHA diffractogram. The existence of $K_2CO_3 \cdot 1.5H_2O$ phase in XRD pattern of CECPHA corroborates the predominant peak located at 1359 cm^{-1} corresponding to

K_2CO_3 in the FTIR spectrum of CECPHA (Fig. 4.10 (c)). A similar observation was also reported by Betiku et al. (2017).

4.4.2 Performance of biomass-derived solid base catalysts in the batch reactor

The performance of the biomass-derived solid base catalysts in the batch reactor was assessed based on the yield and quality of the produced WSFME.

4.4.2.1 WSFME yield

Table 4.7: Yield of WSFME using the biomass-derived solid base catalysts

Catalyst type (solid base)	Catalyst loading (wt. %)	Methanol to oil ratio (v/v)	Reaction temperature (°C)	Reaction time (min)	WSFME yield (wt. %)
CBPA	4	0.8	65	65	78.51± 2.59
CCESP	4	0.8	65	65	52.37± 2.39
CCPHA	4	0.8	65	65	86.37± 0.98
CECPHA	4	0.8	65	65	77.90± 2.43

Table 4.7 presents the yield of waste sunflower methyl esters (WSFME) produced in phase 1 of this study using CBPA, CCESP, CCPHA and CECPHA as biomass-derived solid base catalysts. The set of conditions used to perform all phase 1 catalyzed-transesterifications was chosen based on a previous study performed by Odude et al. (2017), which optimized the transesterification of palm kernel oil (PKO) into palm kernel methyl esters (PKME) using two of the four catalysts being used in this study, namely CBPA and CCPHA.

The WSFME yield was found to be 78.51 ± 2.59 wt. % when CBPA was used as catalyst, 52.37 ± 2.39 wt. % when CCESP was used as catalyst, 86.37 ± 0.98 wt. % and 77.90 ± 2.43 wt. % respectively when CCPHA and CECPHA were used as catalysts. The low yield of CCESP-WSFME was due to unreacted methanol being the main layer of the product rather than WSFME. Also, the separation by gravity was rendered ineffective since the product layers were not as clearly distinguished as in the case of WSFME produced when the other three catalyst were used. The plausible reason for such occurrence, is that the set of reaction conditions

chosen, with emphasis on catalyst amount, might have been considerably low to breakdown the triglyceride molecule completely thus producing an acceptable WSFME yield.

4.4.2.2 WSFME quality

Table 4.8: Properties of WSFME produced in phase 1

Properties	WSFME				ASTM D6751	EN 14214
	CBPA	CCESP	CCPHA	CECPHA		
Kinematic viscosity (mm^2/s) at 40 °C	3.59	32.32	4.28	4.13	1.9-6.0	3.5-5.0
Specific gravity at 25 °C	0.881	0.917	0.881	0.878	0.88	0.86-0.90
Acid value (mg KOH/g)	0.59 ±0.06	0.51 ±0.06	0.43 ±0.05	0.29 ±0.03	0.5 max	0.5 max
American Petroleum index (API)	29.10	22.22	29.14	29.25	36.95	---

The physicochemical and fuel properties of WSFME produced in phase 1 of this study which include kinematic viscosity at 40 °C, specific gravity (SG) at 25 °C, acid value (AV) and API are shown in Table 4.8. Based on the investigated physicochemical and fuel properties, the obtained values for CCPHA-WSFME and CECPHA-WSFME show that these WSFME were within ASTM D6751 and EN 14214 standard specifications. The CBPA-WSFME also met ASTM D6751 and EN 14214 standard specifications except from the acid value result which was slightly above the specified limit. The CCESP-WSFME, on the other hand, did not meet ASTM D6751 and EN 14214 standard specifications. The low quality CCESP-WSFME was due to the layers in the product being undistinguishable. This indicates that the set of reaction conditions chosen, with emphasis on catalyst amount, was not appropriate to produce high quality WSFME when CCESP was used as catalyst. The kinematic viscosity of 3.59 mm^2/s, 4.28 mm^2/s and 4.13 mm^2/s were observed for the CBPA-WSFME, CCPHA-WSFME and CECPHA-WSFME respectively. These values are marginal to the values reported by Odude et al. (2017) which were 4.7 mm^2/s for CBPA-PKME and 4.3 mm^2/s for CCPHA-PKME and 5.93 mm^2/s value reported by Falowo et al. (2019) for FAME produced via microwave-assisted transesterification of an oil blend when CECPHA as used as catalyst. The acid values of 0.59

± 0.06 mg of KOH/g of the CBPA-WSFME, 0.51 ± 0.06 mg of KOH/g CCESP-WSFME as catalyst, 0.43 ± 0.05 mg of KOH/g of the WSFME using CCPHA as catalysts and 0.29 ± 0.03 mg of KOH/g of the WSFME using CECPHA, agree with values 0.5 and 0.4 mg of KOH/g reported by Odude et al. (2017) when CBPA and CCPHA were employed as catalysts.

Based on the WSFME yield and the selected physicochemical and fuel properties of WSFME (used to check the biodiesel quality), the biomass-derived solid base catalysts which performed the best under the chosen set of conditions were CCPHA and CECPHA. Apart from their respective acid values, these two catalysts showed marginal values of the physicochemical and fuel properties as well as yield of WSFME. As result, the choice of the best catalyst between these two was guided by the potential for novelty that each could present. There are quite a few reported studies on CCPHA as a solid base catalyst, with its catalytic properties clearly defined. On the other hand, CECPHA is still a considerably novel catalyst, requiring more investigation and understanding of its catalytic properties and activity. Thus, CECPHA was chosen to be the best performance biomass-derived solid base catalyst.

4.5 Phase 2 results and discussion

4.5.1 Supported biomass-derived solid base catalyst (CECPHA-pumice)

4.5.1.1 Scanning electron microscopy (SEM) and energy dispersive x-ray spectroscopy (EDS)

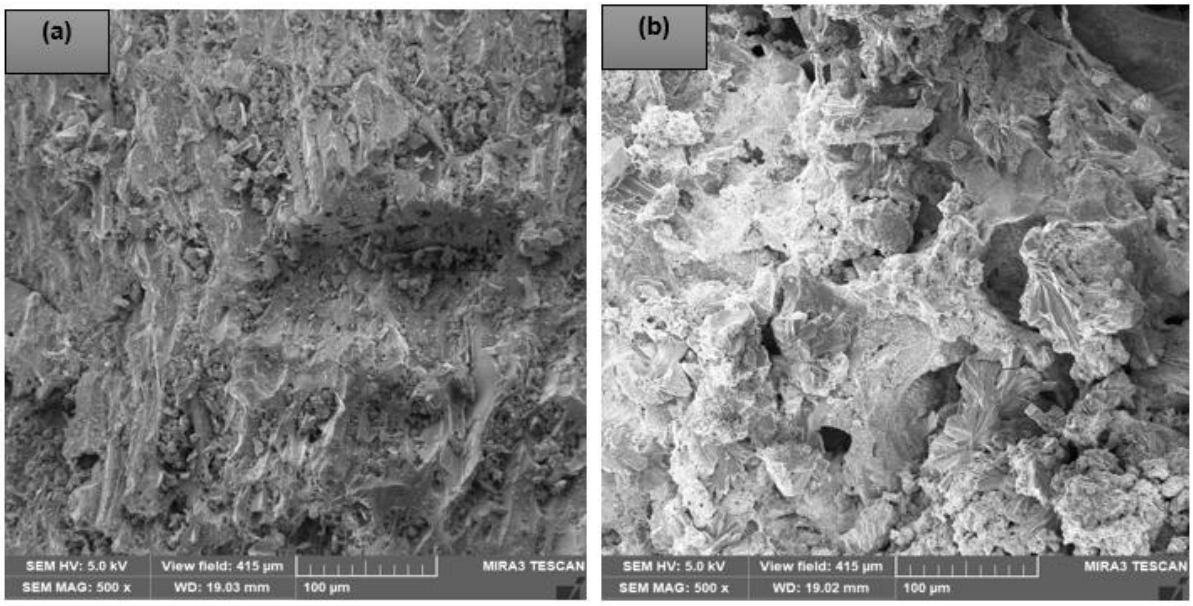

Figure 4.15: SEM images of (a) Pumice and (b) CECPHA-Pumice

The morphologies of the pumice and CECPHA-Pumice samples are shown in Figure 4.15. The pumice (Fig. 4.15(a)) has mostly granular surfaces and cavities which are suitable for metal catalyst impregnation. On the other hand, the surface of CECPHA-Pumice (Fig. 4.15(b)) is constituted by wavy-like nature microstructures which represent the impregnated CECPHA particles that were attached to the pumice. Analogous observations were reported by Cercado et al. (2017).

Table 4.9: Elemental composition of Pumice and CECPHA-Pumice

Elements	Composition (wt. %)	
	Pumice	**CECPHA-Pumice**
K	3.11 ± 0.35	19.71 ± 3.49
Mg	---	3.38 ± 0.80
Ca	0.47 ± 0.08	2.78 ± 0.81
Al	4.78 ± 0.15	1.20 ± 0.15
Fe	0.72 ± 0.17	0.84 ± 0.61
Na	2.35 ± 0.12	0.57 ± 0.10
O	61.57 ± 1.74	63.06 ± 2.25
Si	26.99 ± 1.18	6.73 ± 1.04
P	---	1.43 ± 0.35
S	---	0.29 ± 0.33

Table 4.9, illustrates the elemental composition of pumice and CECPHA-Pumice. The results showed that the key components present in pumice were silicon (Si= 26.99 ± 1.17 wt. %) and oxygen (O = 61.57 ± 1.74 wt. %), as it is a volcanic rock mainly made of silica and alumina (Cercado et al., 2017). Whereas, K, Mg and Ca, were the main metallic components present in the impregnated pumice, i.e. CECPHA-Pumice. From the EDS analysis, it can be seen that there is an increase in the weight percentage of the key metallic components present in the pumice, with emphasis on potassium, which indicates that the pumice was indeed impregnated by CECPHA.

4.5.1.2 Fourier transform infrared (FTIR) spectroscopy

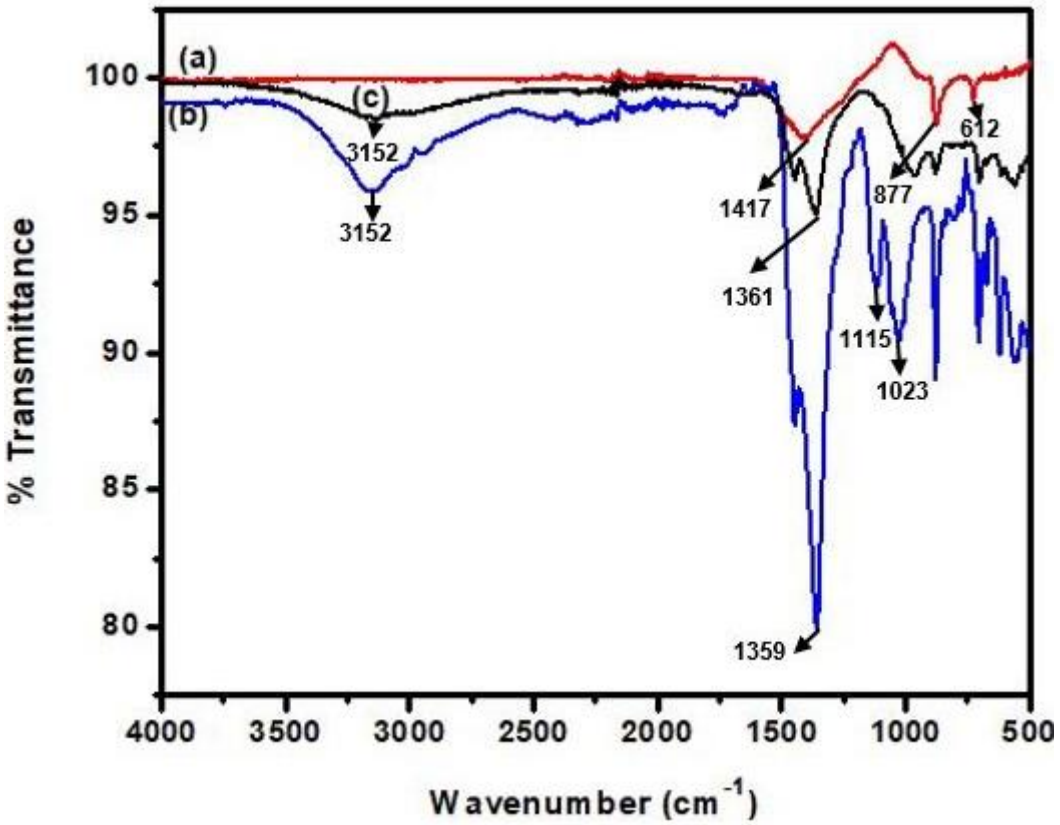

Figure 4.16: FTIR spectra of (a) Pumice; (b) CECPHA and (c) CECPHA-Pumice

Figure 4.16 illustrates the FTIR spectra of pumice, CECPHA and CECPHA-Pumice samples, with view to demonstrate the differences in the infrared spectrum of transmittance of the CECPHA-Pumice and pumice. The IR spectrum of CECPHA (Fig. 4.16 (b)) is displayed for validation purposes, to further corroborate that the pumice was indeed impregnated with CECPHA. This spectrum was discussed in section 4.4.1.3.4 of this study. The broad peak located at 1417 cm^{-1} detected in pumice sample (Fig 4.16 (a)) is ascribed to carbonate C-O stretching and bending vibrations and is indicative of the presence of carbonates (Sharma et al., 2012). The sharp peaks located at 877 cm^{-1} and 612 cm^{-1} observed in the pumice sample are attributed to the Si–O bending strength vibrations of the amorphous quartz (SiO_2) (Cercado et al., 2017). The prominent peaks detected in CECPHA-pumice (Fig 4.16 (c)) were located at 3152 cm^{-1} and 1361 cm^{-1}. The peak at 3152 cm^{-1} is allocated to H−OH stretch or Si−OH, while the peak at 1361 cm^{-1} is attributed to C-O stretching and bending vibrations, particularly K_2CO_3 (Firdaus et al., 2015; Betiku et al., 2017).

4.5.1.3 X-ray diffraction (XRD)

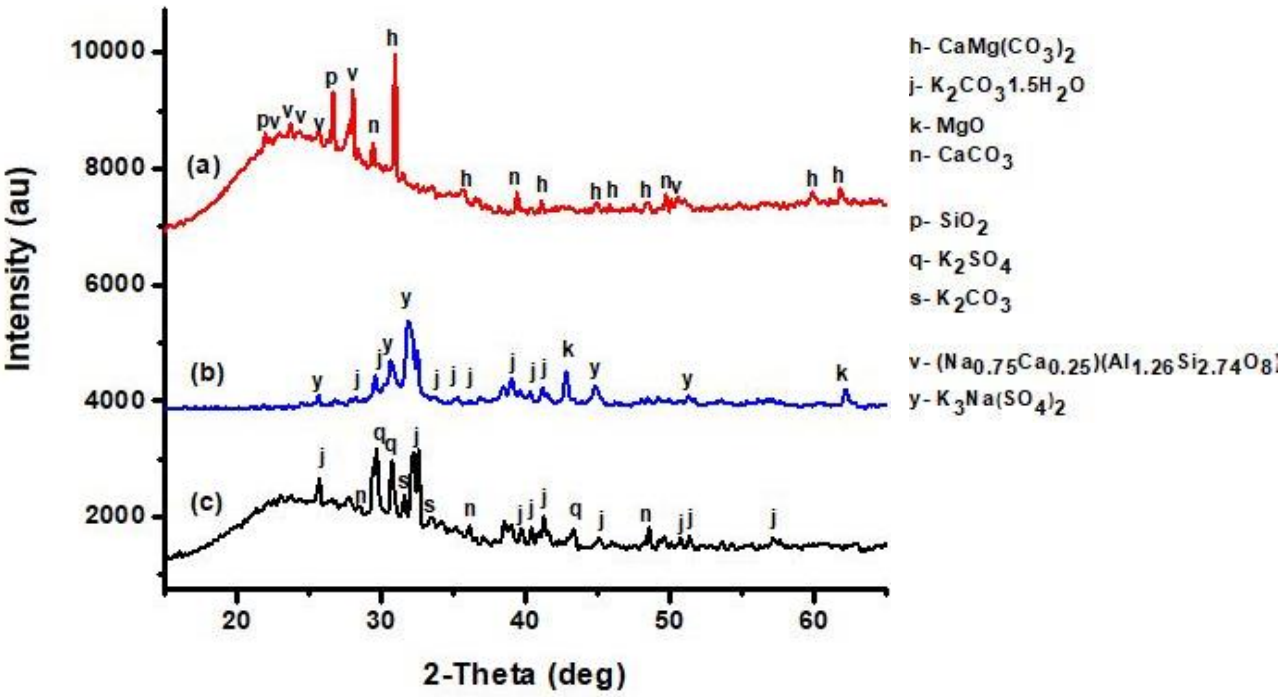

Figure 4.17: XRD pattern of (a) Pumice, (b) CECPHA and (c) CECPHA-Pumice

The XRD patterns of pumice, CECPHA and CECPHA-Pumice, which display the crystalline compounds existent in the samples, are shown in Figure 4.17. These results were considered along with FTIR results of the detected functional groups in the samples. The XRD pattern of CECPHA (Fig. 4.17(b)) is displayed for validation purposes, to further corroborate the impregnation of pumice with CECPHA. This pattern was discussed in section 4.4.1.4.4 of this study. The pumice (Fig.4.17(a)) presents a number of sharp peaks appearing at 2θ = 30.9˚, 37.5˚, 41.2˚, 45˚, 45.1˚, 49.2˚, 60˚ and 62˚ corresponding to calcium magnesium carbonate ($CaMg(CO_3)_2$) (JCPDS card no. 00-036-0426) as the major phase and smaller peaks corresponding to calcium carbonate ($CaCO_3$) (JCPDS card no.00-005-0586), silicon dioxide (SiO_2) (JCPDS card no. 00-083-0539) and sodium calcium aluminium silicate [$(Na_{0.75}Ca_{0.25})(Al_{1.26}Si_{2.74}O_8)$] (JCPDS card no.01-076-0926) as the minor phases. The XRD pattern of CECPHA-Pumice (Fig.4.17(c)), displays various peaks appearing at 2θ = 25.9˚, 32.7˚, 39.9 ˚, 40.5˚, 41.2˚, 45˚, 50.9˚, 51.7˚ and 57.1˚ corresponding to potassium carbonate sesquihydrate (K_2CO_3.1.5 H_2O phase) (JCPDS card no. 00-011-0655) as the major phase. The presence of K_2CO_3 1.5H_2O phase in XRD pattern of CECPHA-Pumice is corroborated by the predominant peak at 1361 cm^{-1} (Fig. 4.16 (c)) corresponding to K_2CO_3 in K_2CO_3 1.5H_2O. Other smaller peaks are also observed in the XRD pattern of CECPHA-Pumice corresponding to calcium carbonate ($CaCO_3$) (JCPDS card no.00-005-0586), potassium carbonate (K_2CO_3)

(JCPDS card no. 00-016-0820) and potassium sulfate (K_2SO_4) (JCPDS card no.00-005-0613) as the minor phases.

4.5.1.4 Brunauer-Emmett-Teller (BET) and Barrett-Joyner-Halenda (BJH)

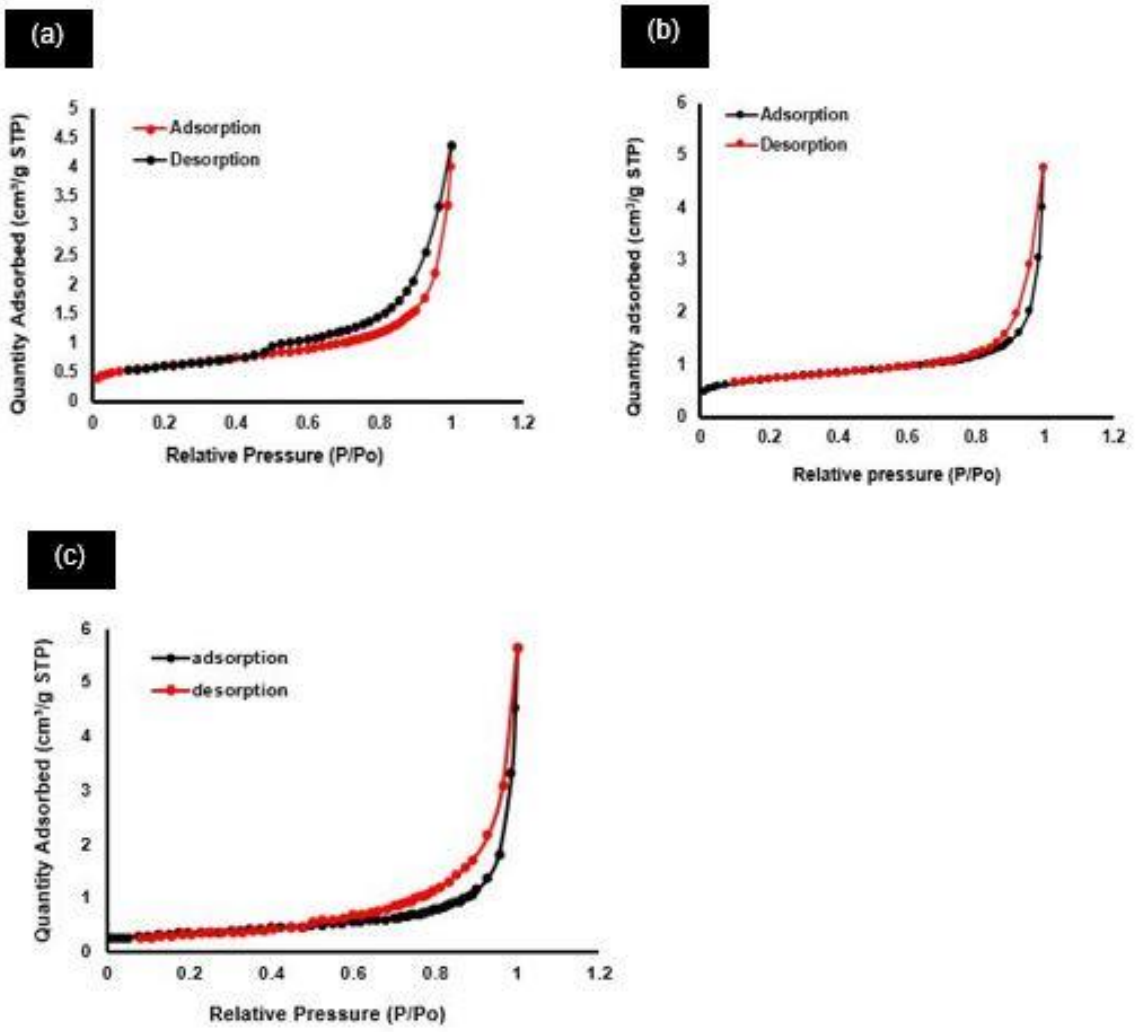

Figure 4.18: N_2 sorption isotherms of (a) Pumice, (b) CECPHA and (c) CECPHA-Pumice

The nitrogen (N_2) adsorption–desorption isotherms of pumice, CECPHA and CECPHA-Pumice samples are displayed in Figure 4.18 (a), (b) and (c) respectively. The shape of N_2 sorption isotherm of all three samples matches typical type IV isotherms as per IUPAC'S classification, with distinctive H_3 hysteresis loop and large adsorption of N_2 at P/Po>0.8 (Betiku et al., 2019; Falowo et.al, 2019). According to IUPAC'S classification, the type IV isotherm represents finite multilayer adsorption corresponding to complete filling of the capillaries and is characteristic of mesoporous materials, i.e. materials with pore sizes in the range of 2-50 nm (Alothman, 2012; Manique et al., 2017). The H_3 hysteresis loop signifies that the samples may have slit-shaped

pores, which is commonly noticed with non-rigid aggregates of plate-like particles (Alothman, 2012).

Table 4.10: Textural properties of Pumice, CECPHA and CECPHA-pumice

Sample	BET surface area (S_{BET}) (m^2/g)	Pore volume (at width range of 1.7 nm to 300 nm) (cm^3/g)	Pore size (nm)
Pumice	2.1736	0.006152	13.4051
CECPHA	2.6222	0.005931	13.3486
CECPHA-Pumice	1.2754	0.007109	22.8291

Table 4.10 summarizes the textural properties of pumice, CECPHA and CECPHA-pumice. The textural parameters for the samples included in this table are: values for the BET specific surface area (S_{BET}), mean pore volume and the pore size. A considerable reduction of the S_{BET} of pumice can be observed, when pumice is impregnated with CECPHA. This is due to the blocking of pores when the CECPHA is introduced. Borges et al. (2011) reported a similar observation when pumice was impregnated with KOH. The pore size for all three samples is within the 2-50 nm range indicating that all samples are mesoporous (Manique et al., 2017). The mesoporous characteristic of pumice (support) may allow access of large molecules (i.e. triglycerides) to the catalyst active sites in CECPHA-pumice, resulting in a significant increase of catalytic activity (Islam et al., 2014; Pan et al., 2018).

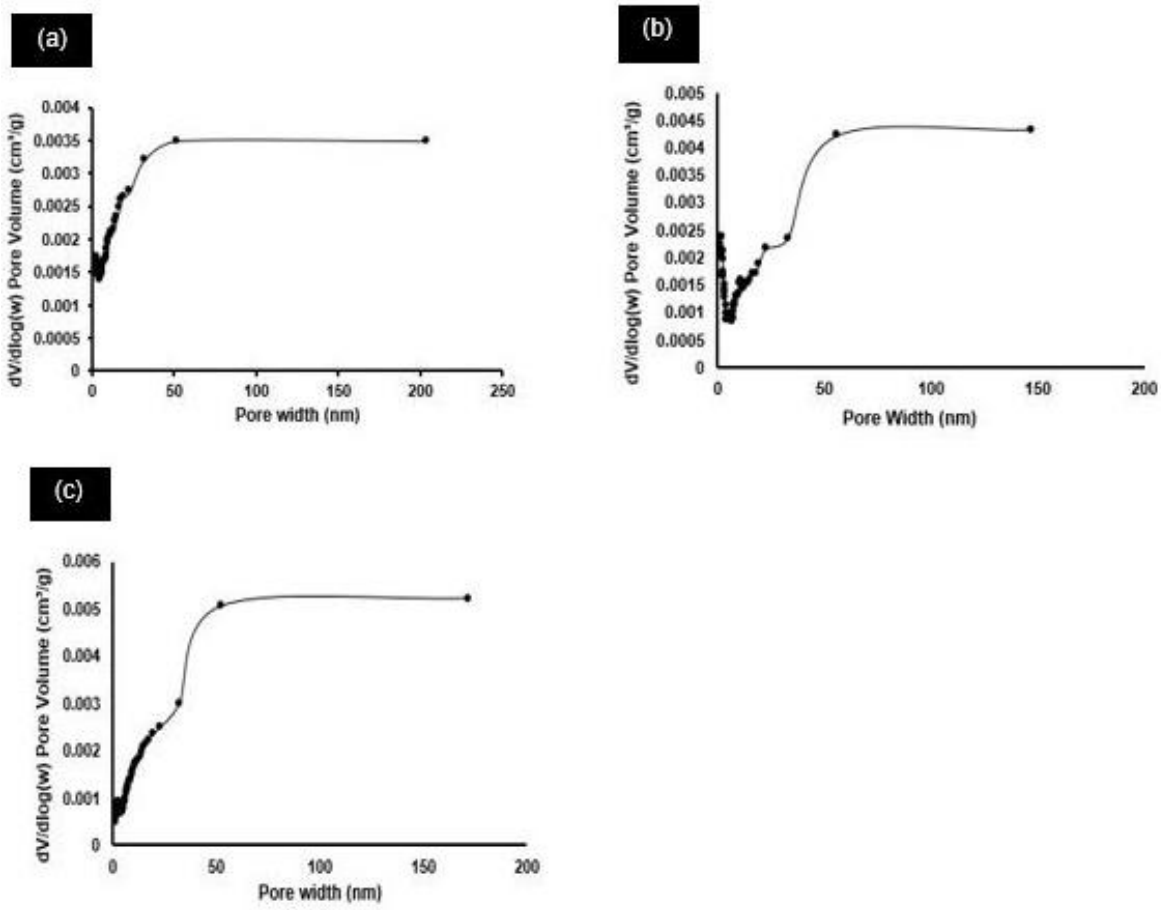

Figure 4.19: Pore-size distribution for (a) Pumice, (b) CECPHA and (c) CECPHA-Pumice

Figure 4.19 (a)-(c) portrays the plot of BJH pore-size distribution of pumice, CECPHA and CECPHA-Pumice respectively. Most of the pores in the CECPHA-Pumice were abundantly distributed within the 10-40 nm pore width region and only a few pores were distributed slightly above the 40 nm pore width region. This shows that the CECPHA-Pumice catalyst is mesoporous (Alothman, 2012; Manique et al., 2017).

4.5.2 WSFME quality (phase 2)

Table 4.11: Properties of WSFME produced in phase 2

Properties	Test Method	Result	ASTM D6751	EN 14214
Kinematic Viscosity at 40 ℃ (mm^2/s)	ASTM D445	18.4	1.9 - 6.0	3.5 - 5.0
Density at 20 ℃ (g/cm^3)	ASTM D4052	0.899	0.88	0.86-0.9
Acid value (mg KOH/g)	ASTM D664	0.44	0.5 max	---
Calorific Value, MJ/kg	ASTM D240	38.786	42-46	35-46
Moisture content (%)	ASTM D6304	0.079	0.05	0.05
Sulphur content, mg/kg (ppm)	ASTM D7039	104.2	50	10

The physicochemical and fuel properties of WSFME produced in phase 2 of this study which include kinematic viscosity at 40 °C, density at 20 °C, acid value (AV), calorific value, moisture content and sulphur content are illustrated in Table 4.11. The value of the kinematic viscosity at 40°C was above the specified standard limits. This could be due to a prolonged storage period which causes the viscosity to increase over time. Kassem et al. (2018) reported a similar observation. The calorific value was within the EN14214 specified limits towards the lower limit. This showed that the thermal energy release per unity quantity of fuel when burned completely is lower which favours a lower power generation to run an engine. The moisture content result was found to be higher than the standard limits, with a difference of 29 ppm. This might have been due to the absorption of atmospheric moisture during storage. He et al. (2007) reported that as the temperature of biodiesel increased, the moisture content increased at a rate of 22.2 ppm/°C. This occurs because during storage biodiesel may absorb atmospheric moisture when exposed to high temperatures and precipitate when temperature decreases. The repetition of this process causes water to accumulate at the bottom of the container. The sulphur content was also found to be higher than the standard limits, this might have been due to excess sodium sulphate left in the biodiesel after the drying step.

CHAPTER 5
KINETIC STUDIES OF CONTINUOUS BIODIESEL PRODUCTION

5.1 Introduction

This chapter is concerned with the presentation of the results of the kinetic experiments performed on the continuous biodiesel production using CECPHA-Pumice as solid base catalyst. Firstly, an overview on kinetics of heterogeneous catalyzed transesterification reaction (section 5.2) is provided and the well-known reaction mechanisms (section 5.3) are reviewed in this chapter. This chapter also highlights the intrinsic kinetic model of transesterification reaction used in this study as well as the relevant assumptions taken to simplify it. Finally, the appropriate kinetic data which includes rate equation, initial rate of reaction, kinetic parameters and Arrhenius parameters, is presented (sections 5.7-5.9). The kinetic results presented in this chapter stem from the experimental procedure described in chapter 3 of this study (sections 3.4.6.4).

5.2 Overview on kinetics of heterogeneous catalyzed transesterification

The kinetics of the transesterification reaction of fats and oils by heterogeneous catalysis is not as surely comprehended as is the kinetics of the transesterification reaction of fats and oils by homogeneous catalysis (Jamal et al., 2014). Most studies on heterogeneous catalyzed transesterification of oils and fats focus more on their production and application (Sewal et al., 2011; Mohamed et al., 2020; Basumatary et al., 2021), with only a few studies focusing on the kinetic modelling of this reaction (Xiao et al., 2010; Li et al., 2013; Nambo et al., 2015; Purwanto et al., 2020). In these studies, extensive research has been done in using small heterogeneous particles to find reaction conditions under an intrinsic kinetics and in which both, the intraparticle mass transfer and external mass transfer phenomena are negligible. As a result, most heterogeneous catalyzed vegetable oil transesterifications have been found to obey a pseudo- first-order rate law (Trejo-Zárraga et al., 2018). More attention has been shifted to the development of reaction kinetic models which can calculate the reaction kinetics data for biodiesel production. The first kinetic model was developed in the 1980s by Freedman and colleagues at USDA (Freedman et al., 1986), after that various kinetic models have been developed. In this study, the kinetics under investigation involve the determination of reaction rate equation, reaction rate constants and activation energy.

5.3 Reaction mechanisms

The transesterification reaction of vegetable oils by heterogeneous catalysis occurs in several steps and in a three-phase arrangement comprising of two immiscible liquid phases (oil and alcohol) and a solid phase (heterogeneous catalyst) (Trejo-Zárraga et al., 2018). In order to define the rate-limiting step, the rates of the different elementary steps ought to be compared (Trejo-Zárraga et al., 2018). This has been attempted by a few researchers by utilizing either the Eley-Rideal (ER) or the Langmuir-Hinshelwood-Hougen-Watson (LHHW) techniques (Gholipour Zanjani et al., 2020). These techniques take into account the adsorption and desorption of the reactants and products on the surface and the active sites of the heterogeneous catalysts (Trejo-Zárraga et al., 2018; Gholipour Zanjani et al., 2020).

5.3.1 Langmuir-Hinshelwood (LHHW) model

The LHHW technique considers reactions at the interface of a catalyst and a liquid phase, i.e. between two chemisorbed molecules (Prins, 2018). This model assumes that both methanol and triglyceride are adsorbed on the neighbouring active sites of the catalyst (Gholipour Zanjani et al., 2020). Thereafter, the adsorbed methanol and triglyceride yield FAME and adsorbed diglyceride. This reaction could be between adsorbed methanol and adsorbed di- or mono- glyceride to produce FAME and glycerol (Gholipour Zanjani et al., 2020).

5.3.2 Eley-Rideal (ER) model

The ER technique considers reactions between a chemisorbed molecule and a physisorbed molecule (Prins, 2018). This model considers the adsorption of methanol on the available sites of the catalyst. The adsorbed methanol consequently interacts with tri-, di-, and monoglycerides (which are in the bulk fluid) resulting in adsorbed diglyceride, monoglyceride, and glycerol, respectively, along with FAME in each step (Gholipour Zanjani et al., 2020).

5.4 Intrinsic Kinetic Model used

The transesterification reaction of this study can be represented as Equation (5.1)

$$\mathbf{WSFO + 3MeOH \leftrightarrow 3WSFME + Glycerol} \quad (5.1)$$

Based on experimental data, calculating the rate of reaction for the transesterification of EWSFO with methanol in the presence of CECPHA-Pumice in the designed PBR encompasses the weight of catalyst (ΔW), volumetric feed flow rate of reactant (v_o), and concentration of reaction product (C_{WSFME}). EWSFO, represented by W, is taken as basis to calculate the rate of reaction, since EWSFO is the limiting reactant in the transesterification reaction. The rate of reaction per unit mass of catalyst (r_{TG}') at steady state is derived in the steps below and described by Equation (5.11)

$$\mathbf{F_{Wi} - F_{Wo} + (r'_{TG})(\Delta W) = 0} \quad (5.2)$$

Where F_{Wi} is the input flow rate of EWSFO, F_{Wo} is the output flow rate of EWSFO, r'_{TG} is the rate of reaction per unit mass of catalyst and ΔW is the catalyst weight.

Solving for$(-r'_{TG})$, it becomes:

$$-r'_{TG} = \frac{F_{Wi} - F_{Wo}}{\Delta W} \quad (5.3)$$

$$\mathbf{F_{Wi} = C_{Wi} \times v_o} \quad (5.4)$$

$$\mathbf{F_{Wo} = C_{Wo} \times v_o} \quad (5.5)$$

Expressing Equation (5.3) in terms of concentration, Eq. (5.6) is obtained

$$-r'_{TG} = \frac{C_{Wi}v_o - C_{Wo}v_o}{\Delta W} \quad (5.6)$$

For a constant feed volumetric flow rate, Eq. (5.6) is simplified to:

$$-r'_{TG} = \frac{v_o (C_{Wi} - C_{Wo})}{\Delta W} \tag{5.7}$$

From stoichiometry:

$$C_{Wo} = C_{Wi} (1 - x) \tag{5.8}$$

$$-r'_{TG} = \frac{v_o \times C_{Wi} \times x}{\Delta W} \tag{5.9}$$

The rate of disappearing of triglycerides (present in the EWSFO) is equal to the rate of appearance of WSFME.

$$-r'_{TG} = r'_{WSFME} \tag{5.10}$$

$$\boxed{r'_{WSFME} = \frac{v_o \times C_{Wi} \times x}{\Delta W} = \frac{v_o \times C_{WSFME} \times x}{\Delta W}} \tag{5.11}$$

Where:

r'_{WSFME} – Rate of formation or of appearance of WSFME (mol/min.g).

C_{Wi} - Initial concentration of triglyceride in the EWSFO (mol/L).

C_{Wo} - Final concentration of triglyceride in the EWSFO (mol/L).

x- Conversion (%).

v_o- Volumetric feed flow rate (L/min).

5.5 Assumptions

For the purpose of modelling the kinetics of the pre-treated waste sunflower oil methanolysis reaction performed over CECPHA-pumice catalyst in the designed PBR, a few assumptions were made regarding the reaction stoichiometry, reaction kinetics and catalyst characteristics.

a) The overall methanolysis reaction is represented by the following stoichiometric equation:

$$\mathrm{W} + 3\mathrm{M} \leftrightarrow 3\mathrm{F} + \mathrm{G}$$

b) The overall reaction occurs essentially via three successive reversible reactions where monoglycerides, diglycerides and glycerol, besides WSFME, are formed. Owing to the fast consumption of the intermediate products, i.e. diglycerides (DG) and monoglycerides (MG) their concentrations are very small compared to the concentration of triglycerides (TG) and therefore negligible (Lukić et al., 2014).

c) Due to the negligible content of FFA in the EWSFO, the neutralization of FFA is ignorable.

d) The saponification reaction is also insignificant due to negligible content of FFA in the EWSFO. Therefore, the catalyst amount remains constant throughout the methanolysis.

5.6 Mechanism used in this study

In this study, the ER mechanism model was used to derive a rate equation for the transesterification reaction of EWSFO with methanol in the presence of CECPHA-Pumice.

According to this model, the reaction comprised of three steps: the adsorption of methanol, a sequence of surface reactions of adsorbed methanol with glyceride from the liquid phase, and the desorption of glycerol. Equation (5.12) describes the overall reaction of triglyceride (W) and methanol (M) to form three WSFME (F) and glycerol (G). The elemental steps of the transesterification are suggested in Equations (5.13)-(5.17). It was assumed that only methanol and glycerol adsorbed on active sites of the solid base catalyst. Firstly, methanol (M) adsorbed on the active sites of the catalyst. Thereafter, triglyceride from the liquid phase reacted with one molecule of adsorbed methanol to produce one WSFME (F) and diglyceride (DG). The diglyceride further reacted with adsorbed methanol to produce one monoglyceride (MG) and one more WSFME (F). Lastly, the monoglyceride reacted with adsorbed methanol to produce the last WSFME (F) and adsorbed glycerol (G). Glycerol (G) ultimately desorbed from the active sites of the catalyst.

$$\mathbf{W} + \mathbf{3M} \leftrightarrow \mathbf{3F} + \mathbf{G} \quad (5.12)$$

$$\mathbf{M} + \boldsymbol{\sigma} \leftrightarrow \mathbf{M}\boldsymbol{\sigma} \quad (5.13)$$

$$\mathbf{M}\boldsymbol{\sigma} + \mathbf{W} \leftrightarrow \mathbf{F} + \mathbf{DG} + \boldsymbol{\sigma} \quad (5.14)$$

$$\mathbf{M}\boldsymbol{\sigma} + \mathbf{DG} \leftrightarrow \mathbf{F} + \mathbf{MG} + \boldsymbol{\sigma} \quad (5.15)$$

$$\mathbf{M}\boldsymbol{\sigma} + \mathbf{MG} \leftrightarrow \mathbf{F} + \mathbf{G}\boldsymbol{\sigma} \quad (5.16)$$

$$\mathbf{G}\boldsymbol{\sigma} \leftrightarrow \mathbf{G} + \boldsymbol{\sigma} \quad (5.17)$$

Where W is EWSFO (i.e. source of triglyceride), M is methanol, F is WSFME, G is glycerol, DG is diglyceride, and MG is monoglyceride. The symbol, σ represents active site of catalyst.

Xiao et al. (2010) reported that the surface reaction should be presumed to be the rate-limiting step, when solid base catalysts are used to catalyse the transesterification reaction. Thus, Equation (5.14) was considered to be the rate-determining elementary step. The other elementary steps were assumed to be equilibrium states. Equation (5.18) as proposed by Xiao et al. (2010) was taken as the rate equation of the overall transesterification reaction in this study.

$$r'_{FAME} = \frac{k(C_w C_M - \frac{1}{K}\frac{C_F^3 C_G}{C_M^2})}{1 + K_M C_M + K_G C_G} \quad (5.18)$$

Where:

k- Rate constant of the transesterification reaction (L^2/mol.g.min)
C_w- Final concentration of triglycerides in EWSFO (mol/L)
C_M- Final concentration of methanol (mol/L)
K- Equilibrium constant of the reaction
C_F- Final concentration of WSFME (mol/L)
C_G- Final concentration of glycerol (mol/L)
K_M- Methanol adsorption equilibrium constant (L/mol)
K_G- Glycerol adsorption equilibrium constant (L/mol)

5.7 Steady-State

Table 5.1: Steady-state verification

Steady-steady samples (SS)	x (%)	Average	Standard deviation
WSFME withdrawn at t_1= 30 min	62.13	62.48	0.26
WSFME withdrawn at t_2= 60 min	62.75		
WSFME withdrawn at t_3= 90 min	62.55		

To verify that the fixed PBR reached steady-state after three residence times, three WSFME samples were taken from the accumulation tank at times t_1= 30 min, t_2= 60 min and t_3= 90 min. Table 5.1 presents the conversion values obtained at the aforementioned reaction times. It can be seen that the system reached steady-state after the three residence times as assumed, since a standard deviation of 0.26 was obtained. After, the system reached steady-state sampling began.

5.8 Determining the initial rates of reaction (r_o)

Table 5.2: Experimental data used to calculate the initial rates of reaction (Initial concentration of TG in EWSFO (C_{wi})= 0.951 mol/L; Catalyst weight (ΔW)= 253g)

v (L/min)	x (%)	r_O (mol/min.g)
0.004	52.74	7.93×10^{-6}
0.003	59.82	6.75×10^{-6}
0.0021	67.06	5.29×10^{-6}
0.0016	77.90	4.69×10^{-6}

Table 5.2 presents the initial rates of reaction at their corresponding feed volumetric flow rates. The initial rates of reaction were calculated using Equation (5.11). It was observed that the highest conversion (x) (77.90%) was obtained at the lowest flow rate (v) (0.0016 L/min). A low feed flow rate allows for more surface interaction between the reactants and the catalyst. This is because at a low feed flow rate the reactants spend more time in the reactor, i.e. longer residence time, resulting in a higher conversion. Conversely, a high feed flow rate implies that the reactants spend less time in the reactor, i.e. shorter residence time, resulting in a lower conversion. This trend has been reported by Agarwal et al. (2013). The obtained values of the initial rates of reaction (r_o) were further used to determine the kinetic parameters of the rate equation, i.e. Equation (5.18).

5.9 Estimating the model parameters

Table 5.3: Model parameters

T (°C)	T (K)	k (L^2/mol.g.min)	K	K_M (L/mol)	K_G (L/mol)	x (%)
60	333.15	3.40E-05	3.0175×10^{-3}	2.42	2.5015	74.06
55	328.15	3.00E-05	3.0176×10^{-3}	2.49	2.5084	77.90
50	323.15	2.50E-05	3.0179×10^{-3}	2.57	2.5126	64.03
40	313.15	2.00E-05	3.0181×10^{-3}	2.62	2.5143	59.33

The four model parameters (k, K, K_M, and K_G) are presented in Table 5.3 and were estimated using the method of multiple nonlinear regressions. Polymath 5.1 software was used for this purpose. In Table 5.3, it can be observed that the increase in temperature (T) resulted in the decrease of the values of glycerol adsorption equilibrium constant (K_G). This is indicative of an exothermic adsorption process. In addition, most adsorption equilibrium constants of methanol under different temperatures were lower than that of glycerol. This could be due to the hydroxyl value of methanol being smaller. It is also worth noting that TG conversion increased (x) significantly with the increase of the reaction temperature. This indicates that the reaction temperature was a determining factor on the kinetics of the transesterification as well as on the TG conversion. At lower temperatures, the kinetic energy is reduced and it is more difficult to overcome diffusion resistance (Wendi et al., 2014), as a three-phase system (oil-methanol-catalyst) is formed by the heterogeneous catalyst. Higher temperatures close to the boiling point of methanol were avoided due to vaporization.

5.10 Arrhenius rate law

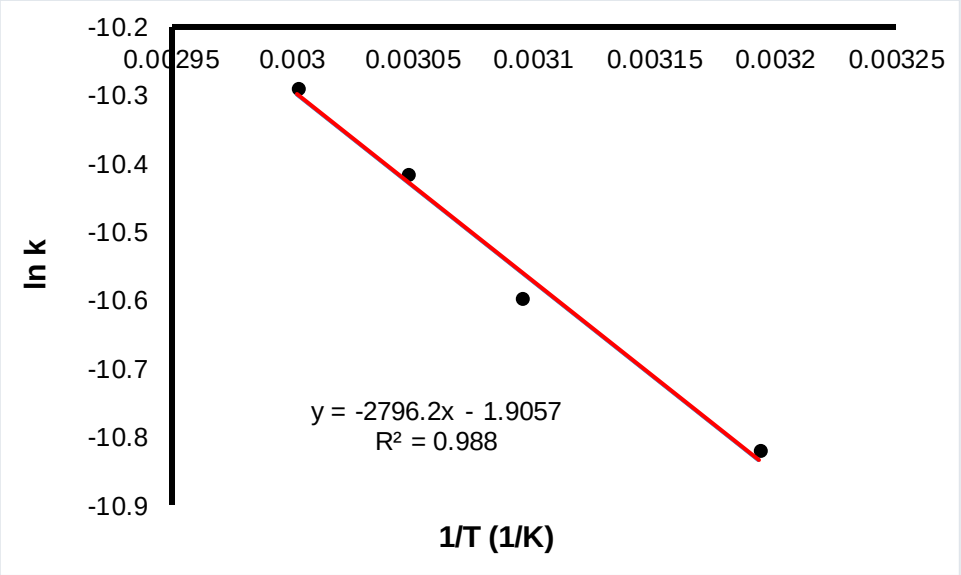

Figure 5.1: Arrhenius plot

Figure 5.1 displays the Arrhenius plot. The reaction activation energy (E_a), which was estimated from the slope of the plot of ln (k) versus 1/T, was found to be 23.25 kJ/mol. A decreased rate of reaction yields a higher activation energy, in this case, a lower activation energy showed that less energy was required for the transesterification reaction to occur.

Similar activation energies of 21.88 and 25.51 kJ/mol were also observed in biodiesel transesterification reactions in the presence of co-solvents (Encinar et al., 2016 and Encinar et al., 2018). The frequency factor (A) was found to be 0.149 mol/ L·min. The regression coefficient (R^2) of the graph was found to be 0.988. This indicates that the experimental data fitted the Arrhenius model in the temperature range investigated.

The rate constant (k) and temperature (T) values displayed in Table 5.2 were used to estimate the parameters of the Arrhenius law using the linear regression method. Table 5.2 shows that rate constants increased with the increase of the temperature, which obeyed the Van't Hoff law. The Arrhenius rate law is described by Equation (5.15). Equation (5.16) is obtained by applying the natural logarithm to Equation (5.15).

$$\mathbf{k = Ae^{-E_a/RT}} \tag{5.15}$$

$$\mathbf{\ln k = \ln A + \left(-\frac{E_a}{R}\right)\frac{1}{T}} \tag{5.16}$$

Where:
k - Rate constant (L/mol·min).
E_a- Activation energy (kJ/mol).
T- Thermodynamic temperature (K).
R- Universal gas constant (J/mol.K).
A- Frequency factor (mol/L.min).

The Arrhenius rate law for the transesterification reaction of WSFO with methanol in the presence of CECPHA-Pumice as catalyst can be expressed as Equation (5.17):

$$\mathbf{k = 0.149e^{-23.25/RT}} \tag{5.17}$$

CHAPTER 6
CONCLUSION & RECOMMENDATIONS

6.1 Conclusion

Solid base catalysts were synthesized from the calcination of selected biomass wastes specifically banana peels (BP), chicken eggshells (CES), cocoa pod husks (CPH) and enterolobium cyclocarpum pods husk (ECPH), respectively. From the characterization of the biomass-derived solid base catalysts (CBPA, CCESP, CCPHA and CECPHA), it was depicted that the active metallic element present in CBPA, CCPHA and CECPHA was found to be potassium (K). While the active metallic element present in the CCESP was found to be calcium (Ca). Also, the active compound or active catalytic phase in the CBPA, CCPHA and CECPHA catalysts was found to be potassium carbonate (K_2CO_3). Whereas the active catalytic phase in the CCESP catalyst was found to be calcium oxide (CaO). The solid base catalyzed-transesterification of WSFO in the batch reactor under the following operating reaction conditions: 65 °C, a methanol to EWSFO ratio of 0.8 (v/v), 4 wt. % catalyst loading and 65 min of reaction, demonstrated that CECPHA was found to have a better performance compared to the other three biomass-derived solid base catalysts. The supported catalyst was prepared having CECPHA as the active catalytic phase. Upon impregnation a significant reduction in surface area was observed in CECPHA. Nonetheless, the CECPHA-Pumice catalyst was found to be effective in converting WSFO to WSFME in the design PBR under the following operating reaction conditions: methanol to EWSFO of 0.9 (v/v), co-solvent (n-hexane) to EWSFO ratio of 0.5 (w/w), 253 g catalyst amount, 55 °C and 1.6 mL/min feed flow rate. N-hexane was a suitable co-solvent added to the EWSFO-methanol mixture to achieve a homogeneous reactant mixture, thus preventing liquid-liquid mass-transfer limitations. The proposed Eley-Rideal mechanism model was suitable to describe the transesterification reaction of EWSFO with methanol in the designed PBR. The rate-limiting step was assumed to be the surface reaction between triglyceride molecule and methanol. The model parameters were regressed according to the experimental data. The regression coefficient (R^2) of the Arrhenius plot graph in this study was found to be 0.988, indicating that the experimental data fitted the Arrhenius model in the investigated temperatures. Overall the objectives of this study were accomplished. More insight into the kinetics of the transesterification of WSFO in a packed bed reactor in the presence of supported biomass-derived solid base catalyst was provided.

6.2 Future work and recommendations

This study made use of CECPHA-Pumice catalyst, the extent of the reusability of this catalyst is an area that can be further investigated. The most feasible and easily available feedstocks with higher oil content and less cost are waste oils, however more research needs to be done to maintain the balance between the availability of raw materials and their usage for biodiesel production.

The flow rate was a significant parameter influencing the kinetics of transesterification of WSFO in presence of CECPHA-pumice in the designed PBR. Therefore, optimization studies with focus on flow rate optimization should be performed in order to realize the full potential of this catalyst in the PBR. Optimization studies of other key parameters influencing the biodiesel yield in the designed PBR continuous such ratio of methanol-to-oil, ratio of co-solvent-to-oil, reaction temperature and catalyst amount or bed height should also be investigated to gain in-depth understanding of the effect of these parameters on the kinetics of the transesterification reaction in the PBR. The storage conditions had a major influence on the physical properties of the biodiesel produced in phase 2, as such, methods to improve biodiesel stability under varying environmental conditions should be further explored.

BIBLIOGRAPHY

Abdullah, S.H.Y.S., Hanapi, N.H.M., Azid, A., Umar, R., Juahir, H., Khatoon, H. & Endut, A. 2017. A review of biomass-derived heterogeneous catalyst for a sustainable biodiesel production. *Renewable and Sustainable Energy Reviews*, 70: 1040–1051, July.

Agarwal, M., Soni, S., Singh, K., Chaurasia, S.P. & Dohare, R.K. 2013. Biodiesel yield assessment in continuous-flow reactors using batch reactor conditions. *International Journal of Green Energy*, 10(1): 28–40.

Ahmad, R., Rohim, R. & Ibrahim, N. 2015. Properties of Waste Eggshell as Calcium Oxide Catalyst. *Applied Mechanics and Materials*, 754–755: 171–175.

Alothman, Z. A. 2012. A review: Fundamental aspects of silicate mesoporous materials. *Materials*, 5(12): 2874–2902.

Alptekin, E. & Canakci, M. 2008. Determination of the density and the viscosities of biodiesel-diesel fuel blends. *Renewable Energy*, 33(12): 2623–2630.

Alptekin, E. & Canakci, M. 2009. Characterization of the key fuel properties of methyl ester-diesel fuel blends. *Fuel*, 88(1): 75–80.

Ambat, I., Srivastava, V. & Sillanpää, M. 2018. Recent advancement in biodiesel production methodologies using various feedstock: A review. *Renewable and Sustainable Energy Reviews*, 90: 356-369.

.

Amos, O., Ogunniyi, D.S. & Odetoye, T.E. 2016. Production of biodiesel from Parinari polyandra B. seed oil using bio-based catalysts. *Nigerian Journal of Technological Development*, 13(1): 26.

Andherson, T., Rachmat, D. & Risanti, D.D. 2018. Potential use of chicken egg shells and cacao pod husk as catalyst for biodiesel production. *AIP Conference Proceedings*, 1945.

Anuar, M.R. & Abdullah, A.Z. 2016. Challenges in biodiesel industry with regards to feedstock, environmental, social and sustainability issues: A critical review. *Renewable and Sustainable Energy Reviews*, 58: 208–223.

AOAC.1990. Official Methods of Analysis (volume 1). *Association of Official Analytical Chemists*. 15th ed. Arlington:Virginia.

Aransiola, E.F., Ojumu, T. V., Oyekola, O.O., Madzimbamuto, T.F. & Ikhu-Omoregbe, D.I.O. 2014. A review of current technology for biodiesel production: State of the art. *Biomass and Bioenergy*, 61: 276–297.

Ashraful, A.M., Masjuki, H.H., Kalam, M.A., Rizwanul Fattah, I.M., Imtenan, S., Shahir, S.A. & Mobarak, H.M. 2014. Production and comparison of fuel properties, engine performance, and emission characteristics of biodiesel from various non-edible vegetable oils: A review. *Energy Conversion and Management*, 80: 202–228.

Atabani, A.E., Silitonga, A.S., Ong, H.C., Mahlia, T.M.I., Masjuki, H.H., Badruddin, I.A. & Fayaz, H. 2013. Non-edible vegetable oils: A critical evaluation of oil extraction, fatty acid compositions, biodiesel production, characteristics, engine performance and emissions production. *Renewable and Sustainable Energy Reviews*, 18: 211–245.

Avhad, M.R. & Marchetti, J.M. 2015. A review on recent advancement in catalytic materials for biodiesel production. *Renewable and Sustainable Energy Reviews*, 50: 696–718.

Awogbemi, O., Onuh, E.I. & Inambao, F.L. 2019. Comparative study of properties and fatty acid composition of some neat vegetable oils and waste cooking oils. *International Journal of Low-Carbon Technologies*, 14(3): 417–425.

Azad, K., Rasul, M.G., Khan, M.M.K. & Sharma, S.C. 2019. Introduction to sustainable and alternative ecofuels. In Azad, K. (ed). *Advances in Eco-Fuels for a Sustainable Environment*. Elsevier Ltd:1-14.

Balat, M. & Balat, H. 2010. Progress in biodiesel processing. *Applied Energy*, 87(6): 1815–1835.

Bamgboye, A.I. & Hansen, A.C. 2008. Prediction of cetane number of biodiesel fuel from fatty acid methyl ester (FAME) composition. *International Agrophysics*, 22(1): 21–29.

Bart, J.C.J., Palmeri, N. & Cavallaro, S. 2010. Emerging new energy crops for biodiesel production. *Biodiesel Science and Technology*: 226–284.

Baskar, G. & Aiswarya, R. 2016. Trends in catalytic production of biodiesel from various feedstocks. *Renewable and Sustainable Energy Reviews*, 57: 496–504.

Basumatary, B., Das, B., Nath, B. & Basumatary, S. 2021. Synthesis and characterization of heterogeneous catalyst from sugarcane bagasse: Production of jatropha seed oil methyl esters. *Current Research in Green and Sustainable Chemistry*, 4(January): 100082.

Berg, J.M., Tymoczko, J.L. & Stryer, L. 2002. *Biochemistry*. 5th ed. New York: W H Freeman.

Betiku, E., Akintunde, A.M. & Ojumu, T.V. 2016. Banana peels as a biobase catalyst for fatty acid methyl esters production using Napoleon's plume (Bauhinia monandra) seed oil: A process parameters optimization study. *Energy*, 103: 797–806.

Betiku, E., Etim, A.O., Pereao, O. & Ojumu, T.V. 2017. Two-Step Conversion of Neem (Azadirachta indica) Seed Oil into Fatty Methyl Esters Using a Heterogeneous Biomass-Based Catalyst: An Example of Cocoa Pod Husk. *Energy and Fuels*, 31(6).

Betiku, E., Okeleye, A.A., Ishola, N.B., Osunleke, A.S. & Ojumu, T. V. 2019. Development of a Novel Mesoporous Biocatalyst Derived from Kola Nut Pod Husk for Conversion of Kariya Seed Oil to Methyl Esters: A Case of Synthesis, Modeling and Optimization Studies. *Catalysis Letters*, 149(7): 1772–1787.

Borges, M.E., Díaz, L., Alvarez-Galván, M.C. & Brito, A. 2011. High performance heterogeneous catalyst for biodiesel production from vegetal and waste oil at low temperature. *Applied Catalysis B: Environmental*, 102(1–2): 310–315.

Borges, M.E. & Díaz, L. 2012. Recent developments on heterogeneous catalysts for biodiesel production by oil esterification and transesterification reactions: A review. *Renewable and Sustainable Energy Reviews*, 16(5): 2839–2849.

Borges, M.E. & Díaz, L. 2013. Catalytic Packed-Bed Reactor Configuration for Biodiesel Production Using Waste Oil as Feedstock. *Bioenergy Research*, 6(1): 222–228.

Buasri, A., Chaiyut, N., Loryuenyong, V., Wongweang, C. & Khamsrisuk, S. 2013. Application of eggshell wastes as a heterogeneous catalyst for biodiesel production.*Sustainable Energy*, 1(2): 7–13.

Campanati, M., Fornasari, G. & Vaccari, A. 2003. Fundamentals in the preparation of heterogeneous catalysts. *Catalysis Today*, 77(4): 299–314.

Canakci, M. & Van Gerpen, J. 1999. Biodiesel Production via acid catalysis. *Transactions of the ASAE-American Society of Agricultural Engineers*, 42(5): 1203–1210.

Carareto, N.D.D., Kimura, C.Y.C.S., Oliveira, E.C., Costa, M.C. & Meirelles, A.J.A. 2012. Flash points of mixtures containing ethyl esters or ethylic biodiesel and ethanol. *Fuel*, 96: 319–326.

Cercado, A.P.I., Ballesteros, F.C. & Capareda, S.C. 2017. Biodiesel from microalgae using synthesized novel alkali catalyst. *Applied Ecology and Environmental Research*, 15(4): 1859–1870.

Chacko, K.C. & Pillai, P.K.C. 1997. Storage and Hot-Water Treatments Enhance Germination of Guanacaste (Enterolobium Cyclocarpum) Seeds . *International Tree Crops Journal*, 9(2): 103–107.

Chakraborty, R., Bepari, S. & Banerjee, A. 2010. Transesterification of soybean oil catalyzed by fly ash and egg shell derived solid catalysts. *Chemical Engineering Journal*, 165(3): 798–805.

Chatterjee, A.K. 2001. X-Ray Diffraction. In Ramachandran, V.S. & Beaudoin, J.J.(eds). *Handbook of Analytical Techniques in Concrete Science and Technology - Principles, Techniques and Application*. Norwich, NY: Elsevier Inc: 275-332.

Chiaramonti, D., Prussi, M., Buffi, M. & Tacconi, D. 2014. Sustainable bio kerosene: Process routes and industrial demonstration activities in aviation biofuels. *Applied Energy*, 136: 767–774.

Chincholkar, S.P., Srivastava, S. & Rehman, A. 2005. Biodiesel as an Alternative Fuel for Pollution Control in Diesel Engine Introduction. *Asian Journal Experimental Sciences*, 19(2): 13–22.

Chong, M.F.,Chen, J.,Oh, P.P.& Chen, Z.S. 2013.Modeling analysis of membrane reactor for biodiesel production. *AIChE Journal*, 59 (1): 258-271.

Chouhan, A.P.S. & Sarma, A.K. 2011. Modern heterogeneous catalysts for biodiesel production: A comprehensive review. *Renewable and Sustainable Energy Reviews*, 15(9): 4378–4399.

Crudo, D., Bosco, V., Cavaglià, G., Grillo, G., Mantegna, S. & Cravotto, G. 2016. Biodiesel production process intensification using a rotor-stator type generator of hydrodynamic cavitation. *Ultrasonics Sonochemistry*, 33: 220–225.

Demirbas, A. 1998. Fuel properties and calculation of higher heating values of vegetable oils. *Fuel*, 77(9–10): 1117–1120.

Demirbas, A. 2006. Biodiesel production via non-catalytic SCF method and biodiesel fuel characteristics. *Energy Conversion and Management*, 47(15–16): 2271–2282.

Demirbas, A. 2008. *Biodiesel- A Realistic Fuel Alternative for Diesel Engines*. London:Spring.

Demirbas, A. 2009. Progress and recent trends in biodiesel fuels. *Energy Conversion and Management*, 50(1): 14–34.

Demirbas, A., Bafail, A., Ahmad, W. & Sheikh, M. 2016. Biodiesel production from non-edible plant oils. *Energy Exploration and Exploitation*, 34(2): 290–318.

Eckey, E.W. 1956. Esterification and interesterification. *Journal of the American Oil Chemists Society*, 33(11): 575–579.

El Zanati, E., Abdallah, H. & Elnahas, G. 2017. Micro-reactor for Non-catalyzed Esterification Reaction: Performance and Modeling. *International Journal of Chemical Reactor Engineering*, 15(2).

Encinar, J.M., Pardal, A. & Sánchez, N. 2016. An improvement to the transesterification process by the use of co-solvents to produce biodiesel. *Fuel*, 166(November): 51–58.

Encinar, J.M., Pardal, A., Sánchez, N. & Nogales, S. 2018. Biodiesel by transesterification of rapeseed oil using ultrasound: A kinetic study of base-catalysed reactions. *Energies*, 11(9).

EPA. 2010. Economics of Biofuels.
https://www.epa.gov/environmental-economics/economics-biofuels [22 August 2019]

Etim, A.O., Betiku, E., Ajala, S.O., Olaniyi, P.J. & Ojumu, T.V. 2018. Potential of ripe plantain fruit peels as an ecofriendly catalyst for biodiesel synthesis. Optimization by artificial neural network integrated with genetic algorithm. *Sustainability (Switzerland),* 10(3).

Falowo, O.A., Oloko-Oba, M.I. & Betiku, E. 2019. Biodiesel production intensification via microwave irradiation-assisted transesterification of oil blend using nanoparticles from elephant-ear tree pod husk as a base heterogeneous catalyst. *Chemical Engineering and Processing - Process Intensification*, 140(April): 157–170.

FAO. 2008. Energy supply and demand: trends and prospects.
http://www.fao.org/3/i0139e/i0139e03.pdf [20 August 2019]

Firdaus, M.Y.N., Osman, H., Metselaar, H.S.C. & Rozyanty, A.R. 2015. Cymbopogon citratus Ash Calcined at Different Temperature. *Bioresources* , 11(1): 2839–2849.

Flores, J.S., Bautista, F. 2012. Knowledge of the Yucatec Maya in seasonal tropical forest management: the forage plants.Rev. Mex. *Biodivers* , 83(2): 503–518.

Freedman, B., Pryde, E.H. & Mounts, T.L. 1984. Variables affecting the yields of fatty esters from transesterified vegetable oils. *Journal of the American Oil Chemists Society*, 61(10): 1638–1643.

Freedman, B., Butterfield, R.O. & Pryde, E.H. 1986. Transesterification kinetics of soybean oil. *Journal of the American Oil Chemists' Society*, 63(10): 1375–1380.

Gan, S., Kiat, H., Weng, C., Osman, N., Anas, M. & Ismail, F. 2010. Ferric sulphate catalysed esterification of free fatty acids in waste cooking oil. *Bioresource Technology*, 101(19): 7338–7343.

Gavryushkin, P., Likhacheva, A., Popov, Z., Bakakin, V., Litasov, K., Shatskiy, A., Ancharov, A. & Gavryushkin, A. 2015. Potassium carbonate under pressure: common structural trend for alkaline carbonates and binary compounds.1-10.

Genge, M.J., Jones, A.P. & Price, G.D. 1995. An infrared and Raman study of carbonate glasses: implications for the structure of carbonatite magmas. *Geochimica et Cosmochimica Acta*, 59(5): 927–937.

Gerpen, J.V., Shanks, B., Pruszko, R. & Clements, D. 2004. Biodiesel Analytical Methods. National Renewable Energy Laboratory. 1-97, (July).

Ghadge, S.V. & Raheman, H. 2005. Biodiesel production from mahua (Madhuca indica) oil having high free fatty acids. *Biomass and Bioenergy*, 28(6): 601–605.

Gheewala, S.H., Damen, B. & Shi, X. 2013. Biofuels: Economic, environmental and social benefits and costs for developing countries in Asia. *Wiley Interdisciplinary Reviews: Climate Change*, 4(6): 497–511.

Gholipour Zanjani, N., Kamran Pirzaman, A. & Yazdanian, E. 2020. Biodiesel production in the presence of heterogeneous catalyst of alumina: Study of kinetics and thermodynamics. *International Journal of Chemical Kinetics*, 52(7): 472–484.

Gohain, M., Devi, A. & Deka, D. 2017. Musa balbisiana Colla peel as highly effective renewable heterogeneous base catalyst for biodiesel production. *Industrial Crops and Products*, 109: 8–18, August.

Gouveia, L., Oliveira, A.C., Congestri, R., Bruno, L., Soares, A.T., Menezes, R.S., Filho, N.R.A. & Tzovenis, I. 2017. *Biodiesel from microalgae*. Elsevier Ltd.

Gumus,R.H., Wauton, I. & Efeonah, I.E.O. 2013. Simulation model for biodiesel production using non-isothermal (CSTR) mode: Membrane reactor. *Chemical and Process Engineering Research*, (2013): 21-34.

Gupta, A.R. & Rathod, V.K. 2018. Waste cooking oil and waste chicken eggshells derived solid base catalyst for the biodiesel production: Optimization and kinetics. *Waste Management*, 79: 169–178.

Haldar, S.K., Ghosh, B.B. & Nag, A. 2009. Utilization of unattended Putranjiva roxburghii non-edible oil as fuel in diesel engine. *Renewable Energy*, 34(1): 343–347.

Hama, S., Yoshida, A., Tamadani, N., Noda, H. & Kondo, A. 2013. Enzymatic production of biodiesel from waste cooking oil in a packed-bed reactor: An engineering approach to separation of hydrophilic impurities. *Bioresource Technology*, 135: 417–421.

Harrington, K.J. 1986. Chemical and physical properties of vegetable oil esters and their effect on diesel fuel performance. *Biomass*, 9(1): 1–17.

Hartman, M., Svoboda, K., Čech, B., Pohořelý, M. & Šyc, M. 2019. Decomposition of Potassium Hydrogen Carbonate: Thermochemistry, Kinetics, and Textural Changes in Solids. *Industrial and Engineering Chemistry Research*, 58(8): 2868–2881.

Hassan, A.B. & Ayodeji, O.V. 2019. Benefits and challenges of biodiesel production in West Africa. *Nigerian Journal of Technology*, 38(3): 621.

He, B.B., Thompson, J.C., Routt, D.W. & Van Gerpen, J.H. 2007. Moisture absorption in biodiesel and its petro-diesel blends. *Applied Engineering in Agriculture*, 23(1): 71–76.

Hellier, P., Ladommatos, N. & Yusaf, T. 2015. The influence of straight vegetable oil fatty acid composition on compression ignition combustion and emissions. *Fuel*, 143: 131–143.

Hossain, A.B.M.S. & Boyce, A.N. 2009. Biodiesel production from waste sunflower cooking oil as an environmental recycling process and renewable energy. *Bulgarian Journal of Agricultural Science*, 15(4): 312–317.

Hossain, A.B.M.S. & Mazen, M.A. 2010. Effects of catalyst types and concentrations on biodiesel production from waste soybean oil biomass as renewable energy and environmental recycling process. *Australian Journal of Crop Science*, 4(7): 550–555.

IEA. 2018. Renewables 2018 - Analysis and forecasts to 2023. https://www.iea.org/reports/renewables-2018/transport#abstract. [20 August 2019]

IEO. 2016. International Energy Outlook. 2016. Chapter 1: World energy demand and economic outlook. https://www.eia.gov/forecasts/ ieo/world.cfm>. [24 August 2019].

Islam, A., Taufiq-Yap, Y.H., Chan, E.S., Moniruzzaman, M., Islam, S. & Nabi, M.N. 2014. Advances in solid-catalytic and non-catalytic technologies for biodiesel production. *Energy Conversion and Management*, 88: 1200–1218.

Jamal, Y., Rabie, A. & Boulanger, B.O. 2014. Determination of methanolysis rate constants for low and high fatty acid oils using heterogeneous surface reaction kinetic models. *Reaction Kinetics, Mechanisms and Catalysis*, 114(1): 63–74.

Johnson, S., Saikia, N., Mathur, H.B. & Agarwal, H.C. 2009. Fatty acids profile of Edible Oils and Fats in India. Centre for Science and Environment, 3-31.

Kassem, Y. & Çamur, H. 2017. A Laboratory Study of the Effects of Wide Range Temperature on the Properties of Biodiesel Produced from Various Waste Vegetable Oils. *Waste and Biomass Valorization*, 8(6): 1995–2007.

Kassem, Y., Aktuğ, B., Özgenç, E., Dib, M.S., Ghisheer, M.M.M., Cole, O.A. & Çamur, H. 2018. Effects of storage period on kinematic viscosity and density of biodiesel and its blends with ultra-low-sulfur diesel fuel at constant storage temperature. *International Journal of Smart Grid and Clean Energy*, 7(2): 130–144.

Kinast, J.A. 2003. Production of biodiesels from multiple feedstocks and properties of biodiesels and biodiesel/diesel blends. Final report. Report 1 in a series of 6. Subcontractor report. *National Renewable Energy Laboratory*, (March): 57.

Knothe, G. 2002. Structure indices in FA chemistry. How relevant is the iodine value? *JAOCS, Journal of the American Oil Chemists' Society*, 79(9): 847–854.

Knothe, G., Matheaus, A.C. & Ryan, T.W. 2003. Cetane numbers of branched and straight-chain fatty esters determined in an ignition quality tester. *Fuel*, 82(8): 971–975.

Knothe, G. 2016. Biodiesel and Its Properties 16-17. In McKeon, T.A., Hayes, D.G., Hildebrand, D.F. & Weselake, R.J. (eds). *Industrial Oil Crops.* Elsevier Inc.: 16-17.

Krisnangkura, K. 1986. A simple method for estimation of cetane index of vegetable oil methyl esters. *Journal of the American Oil Chemists Society*, 63(4): 552–553.

Kyriakidis, N.B. & Katsiloulis, T. 2000. Calculation of iodine Value from Measurements of Fatty Acid Methyl esters of Some Oils: Comparison with the Relevant American Oil Chemists Society Method. *Journal of the American Oil Chemists Society*, 77(12): 1235–1238.

Laca, A., Laca, A. & Díaz, M. 2017. Eggshell waste as catalyst: A review. *Journal of Environmental Management*, 197: 351–359.

Lee, I., Johnson, L.A. & Hammond, E.G. 1995. Use of branched-chain esters to reduce the crystallization temperature of biodiesel. *Journal of the American Oil Chemists' Society*, 72(10): 1155–1160.

Leung, D.Y.C. & Guo, Y. 2006. Transesterification of neat and used frying oil: Optimization for biodiesel production. *Fuel Processing Technology*, 87(10): 883–890.

Li, S., Wang, Y., Dong, S., Chen, Y., Cao, F., Chai, F. & Wang, X. 2009. Biodiesel production from Eruca Sativa Gars vegetable oil and motor, emissions properties. *Renewable Energy*, 34(7): 1871–1876.

Li, Z.H., Lin, P.H., Wu, J.C.S., Huang, Y.T., Lin, K.S. & Wu, K.C.W. 2013. A stirring packed-bed reactor to enhance the esterification-transesterification in biodiesel production by lowering mass-transfer resistance. *Chemical Engineering Journal*, 234: 9–15.

Lukić, I., Kesić, Ž. & Skala, D. 2014. Kinetics of heterogeneous biodiesel synthesis using supported ZnO as catalyst. *Chemical Engineering and Technology*, 37(11): 1879–1884.

Ma, F., Clements, L.D. & Hanna, M.A. 1998. The effects of catalyst, free fatty acids, and water on Transesterification of beef tallow. *Transactions of the ASAE*, 41 (5): 1261-1264.

Ma, F. & Hanna, M.A. 1999. Biodiesel production: A review. *Bioresource Technology*, 70(1): 1–15.

Madhawan, A., Arora, A., Das, J., Kuila, A. & Sharma, V. 2018. Microreactor technology for

biodiesel production: a review. *Biomass Conversion and Biorefinery*, 8(2): 485–496.

Madras, G., Kolluru, C. & Kumar, R. 2004. Synthesis of biodiesel in supercritical fluids. *Fuel*, 83(14): 2029–2033.

Mahajan, S., Konar, S.K. & Boocock, D.G.B. 2006. Determining the acid number of biodiesel. *JAOCS, Journal of the American Oil Chemists' Society*, 83(6): 567–570.

Mahmudul, H.M., Hagos, F.Y., Mamat, R., Adam, A.A., Ishak, W.F.W. & Alenezi, R. 2017. Production, characterization and performance of biodiesel as an alternative fuel in diesel engines – A review. *Renewable and Sustainable Energy Reviews*, 72.

Manique, M.C., Lacerda, L.V., Alves, A.K. & Bergmann, C.P. 2017. Biodiesel production using coal fly ash-derived sodalite as a heterogeneous catalyst. *Fuel*, 190: 268–273.

Mansir, N., Teo, S.H., Rashid, U., Saiman, M.I., Tan, Y.P., Alsultan, G.A. & Taufiq-Yap, Y.H. 2018. Modified waste egg shell derived bifunctional catalyst for biodiesel production from high FFA waste cooking oil. A review. *Renewable and Sustainable Energy Reviews*, 82(November 2016): 3645–3655.

Mardhiah, H.H., Ong, H.C., Masjuki, H.H., Lim, S. & Lee, H. V. 2017. A review on latest developments and future prospects of heterogeneous catalyst in biodiesel production from non-edible oils. *Renewable and Sustainable Energy Reviews*, 67: 1225–1236.

Margaretha, Y.Y., Prastyo, H.S., Ayucitra, A. & Ismadji, S. 2012. Calcium oxide from pomacea sp. shell as a catalyst for biodiesel production. *International Journal of Energy and Environmental Engineering*, 3(1): 1–9.

Marinkovic, D.M., Stankovic, M. V., Velickovic, A. V., Avramovic, J.M., Miladinovic, M.R., Stamenkovic, O.O., Veljkovic, V.B. & Jovanovic, D.M. 2016. Calcium oxide as a promising heterogeneous catalyst for biodiesel production: Current state and perspectives. *Renewable and Sustainable Energy Reviews*, 56: 1387–1408.

Marwaha, A., Rosha, P., Mohapatra, S.K., Mahla, S.K. & Dhir, A. 2018. Waste materials as potential catalysts for biodiesel production: Current state and future scope. *Fuel Processing Technology*, 181(June): 175–186.

May, C.Y. 2004. Transesterification of Palm Oil : Effect of Reaction Parameters. *Journal of Oil Palm Research*, 16(2): 1–11.

Mehboob, A., Nisar, S., Rashid, U., Shean, T., Choong, Y., Khalid, T. & Qadeer, H.A. 2016. Reactor designs for the production of biodiesel. *Ijcbs*, 10(January 2016): 87–94.

Memon, J.R., Memon, S.Q., Bhanger, M.I., Memon, G.Z., El-Turki, A. & Allen, G.C. 2008. Characterization of banana peel by scanning electron microscopy and FT-IR spectroscopy and its use for cadmium removal. *Colloids and Surfaces B:*

Biointerfaces, 66(2): 260–265.

Meneghetti, S.M.P., Meneghetti, M.R., Wolf, C.R., Silva, E.C., Lima, G.E.S., De Coimbra, M.A., Soletti, J.I. & Carvalho, S.H.V. 2006. Ethanolysis of castor and cottonseed oil: A systematic study using classical catalysts. *JAOCS, Journal of the American Oil Chemists' Society*, 83(9): 819–822.

Mishra, V.K. & Goswami, R. 2018. A review of production, properties and advantages of biodiesel. *Biofuels*, 9(2): 273–289.

Mittelbach, M. 1996. Diesel fuel derived from vegetable oils, VI: Specifications and quality control of biodiesel. *Bioresource Technology*, 56(1): 7–11.

Mohadi, R., Anggraini, K., Riyanti, F. & Lesbani, A. 2016. Preparation Calcium Oxide From Chicken Eggshells. *Sriwijaya Journal of Environment*, 1(2): 32–35.

Mohamed, R.M., Kadry, G.A., Abdel-Samad, H.A. & Awad, M.E. 2020. High operative heterogeneous catalyst in biodiesel production from waste cooking oil. *Egyptian Journal of Petroleum*, 29(1): 59–65.

Mohammadi, M., Lahijani, P. & Mohamed, A.R. 2014. Refractory dopant-incorporated CaO from waste eggshell as sustainable sorbent for CO_2 capture: Experimental and kinetic studies. *Chemical Engineering Journal*, 243: 455–464.

Musa, I.A. 2016. The effects of alcohol to oil molar ratios and the type of alcohol on biodiesel production using transesterification process. *Egyptian Journal of Petroleum*, 25(1).

Nambo, A., Miralda, C.M., Jasinski, J.B. & Carreon, M.A. 2015. Methanolysis of olive oil for biodiesel synthesis over ZnO nanorods. *Reaction Kinetics, Mechanisms and Catalysis*, 114(2): 583–595.

Noureddini, H., Harkey, D. & Medikonduru, V. 1998. A continuous process for the conversion of vegetable oils into methyl esters of fatty acids. *JAOCS, Journal of the American Oil Chemists' Society*, 75(12): 1775–1783.

Nyquist, R.A. & Kagel, R.O. 1971. Infrared Spectra of Inorganic Compounds. *Handbook of Infrared and Raman Spectra of Inorganic Compounds and Organic Salts*. Elsevier Inc: 1–18.

Odude, V.O., Adesina, A.J., Oyetunde, O.O., Adeyemi, O.O., Ishola, N.B., Etim, A.O. & Betiku, E. 2017. Application of Agricultural Waste-Based Catalysts to Transesterification of Esterified Palm Kernel Oil into Biodiesel: A Case of Banana Fruit Peel Versus Cocoa Pod Husk. *Waste and Biomass Valorization*, 10(4): 1–12.

Ofori-Boateng, C. & Lee, K.T. 2013. The potential of using cocoa pod husks as green solid base catalysts for the transesterification of soybean oil into biodiesel: Effects of biodiesel on engine performance. *Chemical Engineering Journal*, 220: 395–401.

Ogaga Ighose, B., Adeleke, I.A., Damos, M., Adeola Junaid, H., Ernest Okpalaeke, K. & Betiku, E. 2017. Optimization of biodiesel production from Thevetia peruviana seed oil by adaptive neuro-fuzzy inference system coupled with genetic algorithm and response surface methodology. *Energy Conversion and Management*, 132: 231–240.

Pacific Biodiesel. 2019. History of Biodiesel Fuel.
https://www.biodiesel.com/history-of-biodiesel-fuel/.[22 September 2019]

Pan, D., Liu, T., Yu, F., Chen, S., Yan, X., Shi, X., Fan, B. & Li, R. 2018. Synthesis of ordered mesoporous Mg–Al composite oxide-supported potassium catalysts for biodiesel production. *Catalysis Communications*, 116: 76–80.

Patade, V.Y., Meher, L.C., Grover, A., Gupta, S.M. & Nasim, M. 2018. Omics approaches in biofuel technologies: Toward cost effective, eco-friendly, and renewable energy. In Barh, D. & Azevedo, V. (eds). *Omics Technologies and Bio-Engineering: Towards Improving Quality of Life*. Elsevier Inc:337-351.

Patil, P., Deng, S., Rhodes, J.I. & Lammers, P.J. 2010. Conversion of waste cooking oil to biodiesel using ferric sulfate and supercritical methanol processes. *Fuel*, 89(2): 360–364.

Pavani, A., Hebale, A., Poojary, V., Parulekar, S., Kiran, C. & Neeta, K. 2015. Waste sunflower oil as an alternative fuel for diesel engines. *2015 International Conference on Nascent Technologies in the Engineering Field, ICNTE 2015 - Proceedings*: 0–5.

Perego, C. & Villa, P. 1997. Catalyst preparation methods. *Catalysis Today*, 34: 281–305.

Piñeiro-Vázquez, A.T., Ayala-Burgos, A. J., Chay-Canul, A. J., Ku-Vera, J.C. 2013. Dry matter intake and digestibility of rations replacing concentrates with graded levels of Enterolobium cyclocarpum in Pelibuey lambs. Trop. Anim. *Health Prod*., 45(2): 577–583.

Pinzi, S., Garcia, I.L., Lopez-Gimenez, F.J., DeCastro, M.D.L., Dorado, G. & Dorado, M.P. 2009. The ideal vegetable oil-based biodiesel composition: A review of social, economical and technical implications. *Energy and Fuels*, 23(5): 2325–2341.

Pinzi, S., Lopez-Gimenez, F.J., Ruiz, J.J. & Dorado, M.P. 2010. Response surface modeling to predict biodiesel yield in a multi-feedstock biodiesel production plant. *Bioresource Technology*, 101(24): 9587–9593.

Poddar, T., Jagannath, A. & Almansoori, A. 2015. Biodiesel Production using Reactive Distillation: A Comparative Simulation Study. *Energy Procedia*, 75: 17–22.

Prins, R. 2018. Eley–Rideal, the Other Mechanism. *Topics in Catalysis*, 61(9–11): 714–

721.

Purwanto, P., Buchori, L. & Istadi, I. 2020. Reaction rate law model and reaction mechanism covering effect of plasma role on the transesterification of triglyceride and methanol to biodiesel over a continuous flow hybrid catalytic-plasma reactor. *Heliyon*, 6(10): e05164.

Qiu, P., Yang, B., Yi, C. & Qi, S. 2010. Characterization of KF/γ-Al_2O_3 catalyst for the synthesis of diethyl carbonate by transesterification of ethylene carbonate. *Catalysis Letters*, 137(3–4): 232–238.

Rachmat, D., Mawarani, L.J. & Risanti, D.D. 2018. Utilization of Cacao Pod Husk (Theobroma cacao l.) as Activated Carbon and Catalyst in Biodiesel Production Process from Waste Cooking Oil. *IOP Conference Series: Materials Science and Engineering*, 299(1).

Ramadhas, A.S., Jayaraj, S. & Muraleedharan, C. 2004. Biodiesel production from high FFA rubber seed oil. *Fuel*, 84(4): 335–340.

Raslavičius, L., Semenov, V.G., Chernova, N.I., Keršys, A. & Kopeyka, A.K. 2014. Producing transportation fuels from algae: In search of synergy. *Renewable and Sustainable Energy Reviews*, 40: 133–142.

Refaat, A.A. & Refaat, A.A. 2010. Different techniques for the production of biodiesel from waste vegetable oil. , 7(1): 183–213.

REN21. 2016. Renewable 2016: Global Status Report. http://www.ren21.net/status-of-renewables/global-status-report/>. [24 August 2019]

Ren, Y., He, B., Yan, F., Wang, H., Cheng, Y., Lin, L., Feng, Y. & Li, J. 2012. Continuous biodiesel production in a fixed bed reactor packed with anion-exchange resin as heterogeneous catalyst. *Bioresource Technology*, 113: 19–22.

Rental Center Crete. N.d. Bio Diesel/ Bio Fuel. https://www.rental-center-crete.com/biodiesel-facts-history-performance.html [22 September 2019]

Roschat, W., Kacha, M., Yoosuk, B., Sudyoadsuk, T. & Promarak, V. 2012. Biodiesel production based on heterogeneous process catalyzed by solid waste coral fragment. *Fuel*, 98: 194–202.

Sahoo, P.K., Das, L.M., Babu, M.K.G. & Naik, S.N. 2007. Biodiesel development from high acid value polanga seed oil and performance evaluation in a CI engine. *Fuel*, 86(3): 448–454.

Sani, Y.M., Daud, W.M.A.W. & Abdul Aziz, A.R. 2014. Activity of solid acid catalysts for biodiesel production: A critical review. *Applied Catalysis A: General*, 470: 140–161.

Selvan, T. & Nagarajan, G. 2013. Combustion and emission characteristics of a diesel

engine fuelled with biodiesel having varying saturated fatty acid composition. *International Journal of Green Energy*, 10(9): 952–965.

Semwal, S., Arora, A.K., Badoni, R.P. & Tuli, D.K. 2011. Bioresource Technology Biodiesel production using heterogeneous catalysts. *Bioresource Technology*, 102(3): 2151–2161.

Shafiee, S. & Topal, E. 2009. When will fossil fuel reserves be diminished? *Energy Policy*, 37(1): 181–189.

Sharma, Y.C., Singh, B. & Korstad, J. 2010. Application of an Efficient Nonconventional Heterogeneous Catalyst for Biodiesel Synthesis from Pongamia pinnata Oil. , (19): 3223–3231.

Sharma, M., Khan, A.A., Puri, S.K. & Tuli, D.K. 2012. Wood ash as a potential heterogeneous catalyst for biodiesel synthesis. *Biomass and Bioenergy*, 41: 94–106.

Sharma, P. & Mishra, A.A. 2015. Biofuel Production From Banana Peel By Using Micro Wave. *International Journal of Science, Engineering and Technology*, 3(4): 1015–1018.

Son, S.M. & Kusakabe, K. 2011. Transesterification of sunflower oil in a countercurrent trickle-bed reactor packed with a CaO catalyst. *Chemical Engineering and Processing: Process Intensification*, 50(7): 650–654.

Sootchiewcharn, N., Attanatho, L. & Reubroycharoen, P. 2015. Biodiesel production from refined palm oil using supercritical ethyl acetate in a microreactor. *Energy Procedia*, 79 (2015): 697-703.

Stavarache, C., Vinatoru, M., Nishimura, R. & Maeda, Y. 2005. Fatty acids methyl esters from vegetable oil by means of ultrasonic energy. *Ultrasonics Sonochemistry*, 12(5): 367–372.

Szybist, J.P., Song, J., Alam, M. & Boehman, A.L. 2007. Biodiesel combustion, emissions and emission control. *Fuel Processing Technology*, 88(7): 679–691.

Tan, Y.H., Abdullah, M.O., Nolasco-Hipolito, C. & Taufiq-Yap, Y.H. 2015. Waste ostrich- and chicken-eggshells as heterogeneous base catalyst for biodiesel production from used cooking oil: Catalyst characterization and biodiesel yield performance. *Applied Energy*, 160: 58–70.

Tang, Z.E., Lim, S., Pang, Y.L., Ong, H.C. & Lee, K.T. 2018. Synthesis of biomass as heterogeneous catalyst for application in biodiesel production: State of the art and fundamental review. *Renewable and Sustainable Energy Reviews*, 92(April): 235–253.

Tate, R.E., Watts, K.C., Allen, C.A.W. & Wilkie, K.I. 2006. The densities of three biodiesel fuels at temperatures up to 300 °C. *Fuel*, 85(7–8): 1004–1009.

The South African Bureau of standards, 2011. *South African National Standard (SANS) 1935: Automotive biodiesel — Fatty Acid Methyl Esters (FAME) for diesel engines — Requirements and test methods*. 2nd ed. Pretoria: SABS Standard Division.

Trejo-Zárraga, F., Hernández-Loyo, F. de J., Chavarría-Hernández, J.C. & Sotelo-Boyás, R. 2018. Kinetics of Transesterification Processes for Biodiesel Production. *Biofuels - State of Development*.

Udeh, B.A. 2017. Biodiesel production from waste vegetable oil (Sunflower) obtained from fried chicken and plantain. *Journal of Petroleum & Environmental Biotechnology*, 08(02): 8–11.

Ullah, F., Dong, L., Bano, A., Peng, Q. & Huang, J. 2016. Current advances in catalysis toward sustainable biodiesel production. *Journal of the Energy Institute*, 89(2): 282–292.

Vázquez Yanes, C., Batis Muñoz, A., Alcocer Silva, S., Gual Díaz, M. & Sánchez Dirzo, C. 1999. Native trees and shrubs potentially valuable for ecological restoration and reforestation. Project J-084. Institute of Ecology. Mexico: Autonomous University.

Verma, P., Sharma, M.P. & Dwivedi, G. 2016. Impact of alcohol on biodiesel production and properties. *Renewable and Sustainable Energy Reviews*, 56: 319–333.

Viriya-empikul, N., Krasae, P., Puttasawat, B., Yoosuk, B., Chollacoop, N. & Faungnawakij, K. 2010. Waste shells of mollusk and egg as biodiesel production catalysts. *Bioresource Technology*, 101(10): 3765–3767.

Vyas, A.P., Verma, J.L. & Subrahmanyam, N. 2011. Effects of Molar Ratio, Alkali Catalyst Concentration and Temperature on Transesterification of Jatropha Oil with Methanol under Ultrasonic Irradiation. *Advances in Chemical Engineering and Science*, 01(02): 45–50.

Wan Ghazali, W.N.M., Mamat, R., Masjuki, H.H. & Najafi, G. 2015. Effects of biodiesel from different feedstocks on engine performance and emissions: A review. *Renewable and Sustainable Energy Reviews*, 51: 585–602.

Wang, Y., Ou, S., Liu, P., Xue, F. & Tang, S. 2006. Comparison of two different processes to synthesize biodiesel by waste cooking oil. , 252: 107–112.

Wang, Y., Ou, S., Liu, P. & Zhang, Z. 2007. Preparation of biodiesel from waste cooking oil via two-step catalyzed process. , 48: 184–188.

Wei, Z., Xu, C. & Li, B. 2009. Application of waste eggshell as low-cost solid catalyst for biodiesel production. *Bioresource Technology*, 100(11): 2883–2885.

Wendi, Cuaca, V. & Taslim. 2014. Effect of Reaction Temprature and Catalyst Concentration for Producing Biodiesel from Waste Beef Tallow Using Heterogeneous Catalyst CaO from Waste Eggshell. *Proceedings of The 5th Sriwijaya International Seminar on Energy and Environmental Science & Technology*: 32–37.

Witoon, T. 2011. Characterization of calcium oxide derived from waste eggshell and its application as CO_2 sorbent. *Ceramics International*, 37(8): 3291–3298.

World Bank. n.d . The World Bank – Total population data. http://data.worldbank.org/indicator/SP.POP.TOTL?end=2015&start=1960&view=chart%3E [24 August 2019]

Wright, H.J., Segur, J.B., Clark, H. V., Coburn, S.K., Langdon, E.E. & DuPuis, R.N. 1944. A report on ester interchange. *Oil & Soap*, 21(5): 145–148.

Xiao, Y., Gao, L., Xiao, G. & Lv, J. 2010. Kinetics of the transesterification reaction catalyzed by solid base in a fixed-bed reactor. *Energy and Fuels*, 24(11): 5829–5833.

Xu, J., Liu, C., Wang, M., Shao, L., Deng, L., Nie, K. & Wang, F. 2016. Rotating packed bed reactor for enzymatic synthesis of biodiesel. *Bioresour Technol*, 224: 292–297.

Yohana, E., Yulianto, M.E., Ikhsan, D., Nanta, A.M. & Puspitasari, R. 2016. The development of the super-biodiesel production continuously from Sunan pecan oil through the process of reactive distillation. *AIP Conference Proceedings*, 1737(1).

Zabeti, M., Wan Daud, W.M.A. & Aroua, M.K. 2009. Activity of solid catalysts for biodiesel production: A review. *Fuel Processing Technology*, 90(6): 770–777.

Zahan, K.A. & Kano, M. 2019. Technological Progress in Biodiesel Production: An Overview on Different Types of Reactors. *Energy Procedia*, 156 (2019): 452-457.

APPENDICES

Appendix A: Raw data

Table A1: Potentiometric titration data used to estimate acid value and %FFA of WSFO

Category	Variable	Quantity	Sample #1	Sample #2	Sample#3
Sample size	W	Net Sample size (g)	2.50	2.50	2.50
Titrant volume	V_{in}	Starting vol. (mL)	0.0	0.0	0.0
	V_{en}	Ending vol. (mL)	2.5	2.2	2.2
	V	Net volume (mL)	2.5	2.2	2.2

Table A2: Potentiometric titration data used to estimate saponification value of WSFO

Category	Variable	Quantity	Sample #1	Sample #2	Blank
Sample size	W	Net Sample size (g)	2.00	2.00	0.00
Titrant volume	V_{in}	Starting vol. (mL)	0.0	7.9	15.7
	V_{en}	Ending vol. (mL)	7.9	15.7	34.7
	V	Net volume (mL)	7.9	7.8	19.0

Table A3: Potentiometric titration data used to estimate iodine value of WSFO

Category	Variable	Quantity	Sample #1	Sample #2	Blank
Sample size	W	Net Sample size (g)	0.26	0.26	0.00
Titrant volume	V_{in}	Starting vol. (mL)	0.0	0.0	0.0
	V_{en}	Ending vol. (mL)	19.5	19.4	38.7
	V	Net volume (mL)	19.5	19.4	38.7

Table A4: Potentiometric titration data used to estimate peroxide value of WSFO

Category	Variable	Quantity	Sample #1	Sample #2
Sample size	W	Net Sample size (g)	2.00	2.00
Titrant volume	V_{in}	Starting vol. (mL)	0.0	0.0
	V_{en}	Ending vol. (mL)	53.2	45.2
	V	Net volume (mL)	53.2	45.2

Table A5: Moisture content data of WSFO

Category	Variable	Quantity	Sample#1	Sample#2	Sample #3
Wet Sample size	W_{in}	Weight of petri dish (g)	97.0623	96.1771	96.1319
	W_{final}	Weight of petri dish+ oil (g)	102.2524	101.2871	101.1494
	W	Net Sample size (g)	5.1901	5.1101	5.0175
Dry sample size	W_{in}	Weight of petri dish (g)	97.0623	96.1771	96.1319
	W_{final}	Weight of petri dish+ oil (g)	102.2339	101.2702	101.1336
	W	Net sample size(g)	5.1716	5.0931	5.0017

Table A6: Molar mass and actual density of WSFO

Composition	Formula	% Fatty acid (FA)	Molecular weight (g/mol)	Density (g/cm^3)	% FA/100	Molar mass = Molecular weight ×FA/100	Actual density= Density ×FA/100
Palmitic acid	C16	6.99	256.40	0.8816	0.0699	17.9224	0.06162
Stearic acid	C18	4.16	284.50	0.8817	0.0416	11.8352	0.03668
Arachidic acid	C20	0.33	312.54	0.8240	0.0033	1.0310	0.00272
Behenic acid	C22	0.96	340.60	0.8220	0.0096	3.2698	0.00789
Lignoceric acid	C24	0.35	368.63	0.8660	0.0035	1.2902	0.00303
Oleic acid	C18:1(n-9)	34.51	282.50	0.8950	0.3451	97.4908	0.30886
Eicosenoic acid	C20:1 (n-9)	0.32	310.51	0.8830	0.0032	0.9936	0.00283
Linolenic acid	C18:2 (n-6)	52.38	278.43	0.9140	0.5238	145.8416	0.47875
		100		6.9674		**279.6749**	**0.9024**

Table A7: Data used for pre-treatment of WSFO (esterification) using ferric sulfate as solid acid catalyst

Volume of WSFO (mL)	Theoretical weight of WSFO (g)	Actual weight of WSFO (g)	Volume of MeOH (mL)	Theoretical weight of MeOH (g)	Actual weight of MeOH (g)	Catalyst Weight (g)	Acid value (mg KOH/g)	% Reduction
155.00	139.84	135.86	182.00	144.18	143.15	4.65	0.972 ± 0.11	81.16
155.00	139.84	135.94	182.00	144.18	143.18	4.65	0.898	82.60
155.00	139.84	135.86	182.00	144.18	143.15	4.65	0.972 ± 0.11	81.16

Table A8: Potentiometric titration data used to estimate acid value of EWSFO

EWSFO	Quantity	Sample #1	Sample #2	Sample #3
1st Esterification	Net sample size (g)	2.50	2.50	2.50
	Starting volume (mL)	0.0	0.0	0.0
	Ending volume (mL)	0.4	0.5	0.4
	Net volume (mL)	0.4	0.5	0.4
2nd Esterification	Net sample size (g)	2.50	2.50	2.50
	Starting volume (mL)	0.0	0.0	0.0
	Ending volume (mL)	0.4	0.4	0.4
	Net volume (mL)	0.4	0.4	0.4
3rd Esterification	Net sample size (g)	2.50	2.50	2.50
	Starting volume (mL)	0.0	0.0	0.0
	Ending volume (mL)	0.4	0.5	0.4
	Net volume (mL)	0.4	0.5	0.4

Table A9: Data used for transesterification reactions using CBPA as catalyst (phase 1)

Volume of EWSFO (mL)	Theoretical weight of EWSFO (g)	Actual weight of EWSFO (g)	Volume of MeOH (mL)	Theoretical weight of MeOH (g)	Actual weight of MeOH (g)	Catalyst Weight CBPA (g)	Weight of WSFME (g)	Yield of WSFME (wt.%)
77.50	69.92	69.20	62.00	49.05	45.77	3.10	56.75	82.00
77.50	69.92	69.20	62.00	49.05	45.76	3.10	53.79	77.73
77.50	69.92	69.21	62.00	49.05	45.78	3.10	52.46	75.80

Table 6: Data used for transesterification reactions using CCESP as catalyst (phase 1)

Volume of EWSFO (mL)	Theoretical weight of EWSFO (g)	Actual weight of EWSFO (g)	Volume of MeOH (mL)	Theoretical weight of MeOH (g)	Actual weight of MeOH (g)	Catalyst Weight CCESP (g)	Weight of WSFME (g)	Yield of WSFME (wt.%)
77.50	69.92	69.23	62.00	49.05	45.77	3.10	35.58	51.39
77.50	69.92	69.24	62.00	49.05	45.78	3.10	34.67	50.07
77.50	69.92	69.23	62.00	49.05	45.77	3.10	38.53	55.66

Table A11: Data used for transesterification reactions using CCPHA as catalyst (phase 1)

Volume of EWSFO (mL)	Theoretical weight of EWSFO (g)	Actual weight of EWSFO (g)	Volume of MeOH (mL)	Theoretical weight of MeOH (g)	Actual weight of MeOH (g)	Catalyst Weight CCPHA (g)	Weight of WSFME (g)	Yield of WSFME (wt.%)
77.50	69.92	69.20	62.00	49.05	45.76	3.10	59.54	85.99
77.50	69.92	69.24	62.00	49.05	45.82	3.10	59.13	85.40
77.50	69.92	69.24	62.00	49.05	45.77	3.10	60.73	87.71

Table A12: Data used for transesterification reactions using CECPHA as catalyst (phase 1)

Volume of EWSFO (mL)	Theoretical weight of EWSFO (g)	Actual weight of EWSFO (g)	Volume of MeOH (mL)	Theoretical weight of MeOH (g)	Actual weight of MeOH (g)	Catalyst Weight CECPHA (g)	Weight of WSFME (g)	Yield of WSFME (wt.%)
77.50	69.92	69.22	62.00	49.05	45.81	3.10	56.09	81.02
77.50	69.92	69.23	62.00	49.05	45.81	3.10	53.72	77.60
77.50	69.92	69.23	62.00	49.05	45.82	3.10	51.98	75.08

Table A13: Potentiometric titration data used to estimate acid value of WSFME (phase 1)

WSFME	Quantity	Sample #1	Sample #2	Sample #3
CBPA	Net sample size (g)	0.92	0.92	0.92
	Starting volume (mL)	0.00	0.00	0.00
	Ending volume (mL)	0.09	0.11	0.09
	Net volume (mL)	0.09	0.11	0.09
CCESP	Net sample size (g)	0.92	0.92	0.92
	Starting volume (mL)	0.10	0.00	0.00
	Ending volume (mL)	0.19	0.09	0.07
	Net volume (mL)	0.09	0.09	0.07
CCPHA	Net sample size (g)	0.92	0.92	0.92
	Starting volume (mL)	0.00	0.00	0.00
	Ending volume (mL)	0.08	0.07	0.06
	Net volume (mL)	0.08	0.07	0.06
CECPHA	Net sample size (g)	0.92	0.92	0.92
	Starting volume (mL)	0.00	0.00	0.00
	Ending volume (mL)	0.05	0.05	0.04
	Net volume (mL)	0.05	0.05	0.04

Table A14: Data used to determine density and specific gravity of WSFO and WSFME (phase 1)

Quantity	WSFME				WSFO	Distilled Water
	CBPA	CCESP	CCPHA	CECPHA		
Mass of 50 mL pycnometer (g)	22.15	---	22.15	22.15	22.15	22.15
Mass of 10 mL pycnometer (g)	---	7.02	---	---	---	7.02
Mass of pycnometer + sample at 25 °C (g)	65.53	18.02	65.50	65.39	67.48	71.38 ; 19.02
Net mass of sample at 25 °C (g)	43.38	11.00	43.35	43.24	45.33	49.23[1] ; 12.00[2]
Mass of pycnometer + sample at 15 °C (g)	65.68	18.11	65.68	65.65	67.59	71.46 ; 19.04
Net mass of sample at 15 °C (g)	43.53	11.09	43.53	43.50	45.44	49.31[3] ; 12.02[4]

NB: A smaller size pycnometer was used for density measurements for WSFME produced using CCESP catalyst as it had a lower yield compared to the other catalysts.

[1] Mass of distilled water at 25 °C weighed in the 50 mL pycnometer
[2] Mass of distilled water at 25 °C weighed in the10 mL pycnometer
[3] Mass of distilled water at 15 °C weighed in the 50 mL pycnometer
[4] Mass of distilled water at 15 °C weighed in the 10 mL pycnometer

Table A15: Data used to determine density and kinematic viscosity at 40 °C of WSFO and WSFME (phase 1)

Quantity	WSFME				WSFO	Distilled Water
	CBPA	CCESP	CCPHA	CECPHA		
Mass of 10 mL cylinder (g)	30.75	30.75	30.75	30.75	30.75	30.75
Mass 10 mL of cylinder + sample at 40 °C (g)	39.62	40.02	39.56	39.60	39.97	40.85
Net mass of sample at 40 °C (g)	8.87	9.27	8.81	8.85	9.22	10.10
Dynamic viscosity at 40 °C with a shear rate of 50 (Pa.s)	0.003	0.029	0.004	0.004	0.032	---

Table A16: Data used to calculate the catalyst density used in phase 2.

Category		Quantities
Mass of CECPHA-Pumice (g)	Sample #1	1.01
	Sample #2	1.02
	Sample #3	1.01
	Average mass	1.013
Volume of solvent (mL)	---	3.00
Volume of solvent + CECPHA-Pumice (mL)	Sample #1	3.70
	Sample #2	3.90
	Sample #3	3.70
	Average volume	3.77
Volume of CECPHA-Pumice (mL)	---	0.77
Density of CECPHA-pumice (g/cm^3)	---	1.32

Table A17: Raw steady-state data (55°C and 1.6 mL/min).

WSFME samples Withdrawn at	Saturated Fatty acids (%)		Mono-unsaturated fatty acids (%)		Poly-unsaturated fatty acids (%)	Total FA (%)
	Palmitic acid (C16:0)	Stearic acid (C18:0)	Palmitoleic acid (C16:1)	Oleic acid (C18:1)	Linoleic acid (C18:2)	
t_1=30 min	4.98	2.50	0.48	32.28	21.89	62.13
t_2=60 min	6.69	3.08	1.74	38.92	12.32	62.75
t_3= 90 min	6.96	3.35	1.10	28.88	22.26	62.55

Table A18: Fatty acid composition of EWSFO and waste sunflower methyl esters (WSFME) as per GC-FID analysis.

Sample	Saturated Fatty acids (%)		Mono-unsaturated fatty acids (%)		Poly-unsaturated fatty acids (%)	Total FA (%)
	Palmitic acid (C16:0)	Stearic acid (C18:0)	Palmitoleic acid (C16:1)	Oleic acid (C18:1)	Linoleic acid (C18:2)	
EWSFO	5.79	2.90	0.39	36.39	30.74	76.21
A	2.53	1.45	0.35	9.36	14.01	27.70
B	5.56	2.80	0.82	19.09	19.69	47.96
C	5.33	2.52	0.93	33.06	17.49	59.33
D	4.92	2.45	0.77	30.36	16.18	54.68
E	3.38	1.56	0.40	20.71	14.18	40.23
F	6.96	3.35	1.10	22.84	22.26	56.51
G	6.76	3.15	1.70	39.77	12.65	64.03
H	7.29	3.03	2.32	37.87	6.73	57.24
I	6.09	2.79	1.74	34.63	7.50	52.75
J	5.02	2.27	0.83	29.83	21.89	59.84
K	7.39	3.41	1.57	44.96	20.59	77.92
L	5.40	2.71	0.53	34.82	23.61	67.07
M	3.53	1.64	0.52	21.26	14.45	41.40
N	4.54	2.36	0.60	29.65	15.36	52.51
O	6.43	3.22	1.08	40.94	22.39	74.06
P	6.69	3.08	1.74	38.92	12.32	62.75

Legend

A-WSFME sample withdrawn at 30 minutes (1.6 mL/min and 40°C); B- WSFME sample withdrawn at 60 minutes (1.6 mL/min and 40°C); C- WSFME sample withdrawn at 90 minutes (1.6 mL/min and 40°C); D- WSFME sample withdrawn at 120 minutes (1.6 mL/min and 40°C)

E-WSFME sample withdrawn at 30 minutes (1.6 mL/min and 50°C); F- WSFME sample withdrawn at 60 minutes (1.6 mL/min and 50°C); G- WSFME sample withdrawn at 90 minutes (1.6 mL/min and 50°C); H- WSFME sample withdrawn at 120 minutes (1.6 mL/min and 50°C)

I-WSFME sample withdrawn at 30 minutes (4 mL/min and 55°C); J- WSFME sample withdrawn at 45 minutes (3 mL/min and 55°C); K- WSFME sample withdrawn at 90 minutes (1.6 mL/min and 55°C); L- WSFME sample withdrawn at 90 minutes (2.1 mL/min and 55°C)

M-WSFME sample withdrawn at 30 minutes (1.6 mL/min and 60°C); N- WSFME sample withdrawn at 60 minutes (1.6 mL/min and 60°C); O- WSFME sample withdrawn at 90 minutes (1.6 mL/min and 60°C); P- WSFME sample withdrawn at 120 minutes (1.6 mL/min and 60°C)

Appendix B: Sample calculations

1. Estimation of the acid value(AV) and %FFA of WSFO

$$\text{Acid value (AV)} = \frac{56.1 \times \text{N} \times \text{V}}{\text{w}}$$

$$\text{AV(sample \#1)} = \frac{56.1 \times 0.1 \times 2.5}{2.5} = 5.610 \ \frac{\text{mg KOH}}{\text{g}}$$

$$\text{AV (samples \#2 and \#3)} = \frac{56.1 \times 0.1 \times 2.2}{2.5} = 4.937 \ \frac{\text{mg KOH}}{\text{g}}$$

$$\text{Average AV} = \frac{5.61 + 4.937 + 4.937}{3} = 5.161 \ \frac{\text{mg KOH}}{\text{g}}$$

- *Standard deviation of the acid value of WSFO (error)*

The formula below was used to calculate all the errors in every result in this study.

$$\sigma = \sqrt{\frac{\sum(\text{x}_\text{i} - \mu)^2}{\text{N}}}$$

Where:

σ- Standard deviation or error

x_i – Each acid value of WSFO (i.e. AV for sample 1, sample 2 and sample 3)

μ - Average AV of WSFO

N- Number of samples

$$\sigma = \sqrt{\frac{(5.61 - 5.16)^2 + (4.94 - 5.16)^2 + (4.94 - 5.16)^2}{3}}$$

$$\sigma = \sqrt{\frac{(0.2025 + 0.0484 + 0.0484)}{3}}$$

$$\sigma = 0.32$$

$$\%\text{FFA} = \frac{\text{Acid value}}{1.99}$$

$$\%\text{FFA (sample \#1)} = \frac{5.61}{1.99} = 2.82$$

$$\%\text{FFA (samples \#2 and \#3)} = \frac{4.94}{1.99} = 2.48$$

$$\text{Average \%FFA} = \frac{2.82. + 2.48 + 2.48}{3} = 2.59$$

2. Estimation of the saponification value (SV) of WSFO

$$\text{SV} = 56.1 \times \frac{(\text{vol. of HCl required by blank} - \text{vol. of HCl required by WSFO}) \times 0.5\ \text{N HCl}}{\text{weight of WSFO sample (g)}}$$

$$\text{SV (sample \# 1)} = 56.1 \times \frac{(19 - 7.9) \times 0.5}{2} = 155.68\ \frac{\text{mg KOH}}{\text{g}}$$

$$\text{SV (sample \# 2)} = 56.1 \times \frac{(19 - 7.8) \times 0.5}{2} = 157.08\ \frac{\text{mg KOH}}{\text{g}}$$

$$\text{Average SV} = \frac{155.68 + 157.08}{2} = 156.38\ \frac{\text{mg KOH}}{\text{g}}$$

3. Estimation of the iodine value (IV) of WSFO

$$\text{IV} = \frac{(\text{B} - \text{S}) \times \text{N} \times 12.69}{\text{weight of WSFO sample (g)}}$$

$$\text{IV (sample \# 1)} = \frac{(38.7 - 19.5) \times 0.1 \times 12.69}{0.26} = 93.71\ \frac{\text{g } I_2}{100\text{ g oil}}$$

$$\text{IV (sample \# 2)} = \frac{(38.7 - 19.4) \times 0.1 \times 12.69}{0.26} = 94.20\ \frac{\text{g } I_2}{100\text{ g oil}}$$

$$\text{Average IV} = \frac{93.71 + 94.20}{2} = 93.96\ \frac{\text{g } I_2}{100\text{ g oil}}$$

4. Estimation of the peroxide value (PV) of WSFO

$$\text{PV} = \frac{\text{Volume of } Na_2S_2O_3 \text{ (L)} \times \text{ Normality of } Na_2S_2O_3 \text{ } (\text{meq}\frac{O_2}{L})}{\text{weight of WSFO sample (kg)}}$$

$$\text{PV (sample \# 1)} = \frac{5.32 \times 10^{-3} \times 0.004}{0.002} = 0.11 \ \frac{\text{meq } O_2}{\text{kg oil}}$$

$$\text{PV (sample \# 2)} = \frac{4.52 \times 10^{-3} \times 0.004}{0.002} = 0.09 \ \frac{\text{meq } O_2}{\text{kg oil}}$$

$$\text{Average PV} = \frac{0.11 + 0.09}{2} = 0.1 \ \frac{\text{meq } O_2}{\text{kg oil}}$$

5. Calculating the moisture content(%) of WSFO

$$\text{Moisture content (\%)} = \frac{\text{weight of wet WSFO (g)} - \text{weight of dry WSFO(g)}}{\text{weight of wet WSFO (g)}}$$

$$\text{Moisture content (sample \#1) (\%)} = \frac{5.1901 - 5.1716}{5.1901} = 0.0036$$

$$\text{Moisture content (sample \#2) (\%)} = \frac{5.1101 - 5.0931}{5.1101} = 0.0033$$

$$\text{Moisture content (sample \#3) (\%)} = \frac{5.0175 - 5.0017}{5.0175} = 0.0031$$

$$\text{Average Moisture content (\%)} = \frac{0.0036 + 0.0033 + 0.0031}{3} = 0.0033$$

6. Calculating CN, DI, AP and HHV of WSFO

- *Cetane number (CN)*

$$\text{CN} = 46.3 + \left(\frac{5458}{\text{SV}}\right) - (0.225 \times \text{IV})$$

$$\text{CN} = 46.3 + \left(\frac{5458}{156.38}\right) - (0.225 \times 93.96)$$

$$\mathrm{CN} = 60.06$$

- *Diesel index (DI)*

$$\mathrm{DI} = (\mathrm{CN} - 10)/0.72$$

$$\mathrm{DI} = (60.06 - 10)/0.72$$

$$\mathrm{DI} = 36.04$$

- *Aniline point (AP)*

$$\mathrm{AP} = (\mathrm{DI} \times 100/\ \mathrm{API})$$

$$\mathrm{AP} = (36.04 \times 100/\ 22.40)$$

$$\mathrm{AP} = 160.89\ ^{\circ}\mathrm{F}$$

- *High heating value (HHV)*

$$\mathrm{HHV} = 49.43 - [0.041 \times (\mathrm{SV}) + 0.015 \times (\mathrm{IV})]$$

$$\mathrm{HHV} = 49.43 - [0.041 \times (156.38) + 0.015 \times (93.96)]$$

$$\mathrm{HHV} = 41.60\ \mathrm{MJ/kg}$$

7. Quantities used for WSFO pre-treatment (esterification reaction)

- Calculating the volume of WSFO to be used in the pre-treatment (esterification)

Mass of WSFO

From Stoichiometry it is known that:

$$\text{Number of moles of WSFO } (\mathrm{n_{WSFO}}) = 1 \text{ mole}$$

$$\mathrm{m_{WSFO}} = \text{number of moles of WSFO } (\mathrm{n_{WSFO}}) \times \text{molar mass of WSFO } (\mathrm{Mr_{WSFO}})$$

$$\mathrm{m_{WSFO}} = 1 \times 279.67$$

$$\mathrm{m_{WSFO}} = 279.67\ \mathrm{g}$$

Volume of WSFO

$$\text{Volume of WSFO} = \frac{\text{Mass of WSFO } (m_{WSFO})}{\text{Density of WSFO } (\rho_{WSFO})}$$

$$\text{Volume of WSFO} = \frac{279.67}{0.902}$$

$$\text{Volume of WSFO} = 309.93 \text{ cm}^3$$

- Calculating the volume of methanol (MeOH) and the catalyst amount to be used in esterification step (pre-treatment)

Given that:

$$\text{Molar mass of MeOH } (Mr_{MeOH}) = 32.04 \frac{\text{g}}{\text{mol}}$$
$$\text{Density of MeOH } (\rho_{MeoH}) = 0.791 \frac{\text{g}}{\text{cm}^3}$$

For trial 1, the following conditions were used: 9:1 MeOH-to-WSFO molar ratio and 3 wt. % of WSFO catalyst loading. These conditions where used elsewhere (Ighose et al., 2017)

$$\therefore \text{Number of moles of MeOH } (n_{MeOH}) = 9 \text{ moles}$$

Mass of methanol

$$m_{MeOH} = \text{number of moles of MeOH } (n_{MeOH}) \times \text{molar mass of MeOH } (Mr_{MeOH})$$

$$m_{MeOH} = 9 \times 32.04$$

$$m_{MeOH} = 288.36 \text{ g}$$

Volume of Methanol

$$\text{Volume of MeOH} = \frac{\text{Mass of MeOH } (m_{MeOH})}{\text{Density of MeOH } (\rho_{MeOH})}$$

$$\text{Volume of MeOH} = \frac{288.36}{0.791}$$

$$\text{Volume of MeOH} = 364.41 \text{ cm}^3$$

Catalyst loading (wt. % of WSFO)

$$m_{Fe2\,(SO4)3} = \text{Volume of WSFO} \times 3/100$$

$$m_{Fe2\,(SO4)3} = 364.41 \times 3/100$$

$$m_{Fe2\,(SO4)3} = 9.30\ \text{g}$$

NB: Due to size of the reactor used for esterification assays the quantities of WSFO, methanol and ferric sulfate catalyst were all reduced, i.e. divided, by a factor of 3.

Thus, the used quantities were as follows:

$$\text{Volume of WSFO} = 103.31\ \text{cm}^3$$
$$\text{Volume of MeOH} = 121.47\ \text{cm}^3$$
$$m_{\ Fe2\,(SO4)3} = 3.10\ \text{g}$$

8. Calculating the percentage reduction of the acid value of WSFO after pre-treatment

$$\%\ \text{reduction} = \frac{AV_{\text{initial}} - AV_{\text{final}}}{AV_{\text{initial}}} \times 100$$

$$\%\ \text{reduction (1st esterification)} = \frac{5.161 - 0.972}{5.16} \times 100 = 81.16$$

$$\%\ \text{reduction (2nd esterification)} = \frac{5.161 - 0.898}{5.161} \times 100 = 82.60$$

$$\%\ \text{reduction (3rd esterification)} = \frac{5.161 - 0.972}{5.161} \times 100 = 81.16$$

$$\text{Average \% reduction} = \frac{81.16 + 82.60 + 81.16}{3} = 81.64$$

9. Quantities used for transesterification reactions (phase 1)

- Calculating the volume of EWSFO to be used in transesterification reactions

Mass of EWSFO

From Stoichiometry it is known that:

$$\text{Number of moles of EWSFO } (n_{EWSFO}) = 1\ \text{mole}$$

$$m_{EWSFO} = \text{number of moles of EWSFO } (n_{EWSFO}) \times \text{ molar mass of EWSFO } (Mr_{EWSFO})$$

$$m_{EWSFO} = 1 \times 279.67$$

$$m_{EWSFO} = 279.67 \text{ g}$$

Volume of EWSFO

$$\text{Volume of EWSFO} = \frac{\text{Mass of EWSFO } (m_{EWSFO})}{\text{Density of EWSFO } (\rho_{EWSFO})}$$

$$\text{Volume of EWSFO} = \frac{279.67}{0.902}$$

$$\text{Volume of EWSFO} = 309.93 \text{ cm}^3$$

- Calculating the volume of methanol (MeOH) and the catalyst amount to be used in transesterification reactions

Given that:

$$\text{Density of MeOH } (\rho_{MeoH}) = 0.791 \frac{\text{g}}{\text{cm}^3}$$

The following conditions were used for all phase 1 reactions: 0.8 volume ratio of MeOH-to-EWSFO and 4 w.t% of EWSFO catalyst loading. These conditions where used elsewhere (Odude et al., 2017).

Volume of Methanol

$$\text{Volume of MeOH} = \text{volume ratio of MeOH to EWSFO} \times \text{Volume of EWSFO}$$

$$\text{Volume of MeOH} = 0.8 \times 309.93$$

$$\text{Volume of MeOH} = 247.94 \text{ cm}^3$$

Mass of methanol

$$m_{MeOH} = \text{Volume of MeOH } (v_{MeOH}) \times \text{ Density of MeOH } (\rho_{MeOH})$$

$$m_{MeOH} = 247.94 \times 0.791$$

$$m_{MeOH} = 196.20 \text{ g}$$

Catalyst loading (wt. % of EWSFO)

$$m_{(\text{CBPA,CCESP,CCPHA OR CECPHA})} = \text{Volume of EWSFO} \times 4/100$$

$$m_{(\text{CBPA,CCESP,CCPHA OR CECPHA})} = 247.94 \times 4/100$$

$$m_{(\text{CBPA,CCESP,CCPHA OR CECPHA})} = 12.40 \text{ g}$$

NB: Due to size of the reactor used for transesterification assays the quantities of EWSFO, methanol and catalysts were all reduced, i.e. divided by a factor of 4.

Thus, the used quantities were as follows:

$$\text{Volume of EWSFO} = 77.5 \text{ cm}^3$$
$$\text{Volume of MeOH} = 62.00 \text{ cm}^3$$
$$m_{(\text{CBPA,CCESP,CCPHA OR CECPHA})} = 3.10 \text{ g}$$

10. Calculating the yield of CBPA-WSFME for phase 1

$$\text{WSFME yield (wt.\%)} = \frac{\text{Weight of WSFME produced}}{\text{Weight of EWSFO used}} \times 100$$

$$\text{WSFME yield (sample \#1)} = \frac{56.75}{69.20} \times 100 = 82.00\ \%$$

$$\text{WSFME yield (sample \#2)} = \frac{53.79}{69.20} \times 100 = 77.73\ \%$$

$$\text{WSFME yield (sample \#3)} = \frac{52.46}{69.21} \times 100 = 75.79\ \%$$

$$\text{Average CBPA based WSFME} = \frac{82.00 + 77.73 + 75.79}{3} = 78.51\ \%$$

11. Calculating the SG of CBPA-WSFME for phase 1 at 25°C and at 15°C

Before use, both pycnometers (i.e. the 50 mL and 10 mL pycnometer) were calibrated with distilled water to estimate the exact volume occupied by the liquids in each pycnometer at required temperatures. Below only the 50mL pycnometer calibration is shown, but 10 mL pycnometer calibration was done similarly.

- *Calibration calculations*

$$V_{\text{distilled water (at 25 °C)}} = \frac{m_{\text{distilled water (at 25 °C)}}}{\rho_{\text{distilled water (at 25 °C)}}}$$

$$V_{\text{distilled water (at 25 °C)}} = \frac{49.23}{0.997} = 49.38 \text{ mL}$$

$$V_{\text{CBPA–WSFME (at 25 °C)}} = V_{\text{distilled water (at 25 °C)}}$$

$$V_{\text{distilled water (at 15 °C)}} = \frac{m_{\text{distilled water (at 15 °C)}}}{\rho_{\text{distilled water (at 15 °C)}}}$$

$$V_{\text{distilled water (at 15 °C)}} = \frac{49.31}{0.999} = 49.35 \text{ mL}$$

$$V_{\text{CBPA–WSFME (at 15 °C)}} = V_{\text{distilled water (at 15 °C)}}$$

- *Density of CBPA-WSFME at 25* °C

$$\rho_{\text{CBPA–WSFME (at 25 °C)}} = \frac{m_{\text{CBPA–WSFME}}}{V_{\text{CBPA–WSFME}}}$$

$$\rho_{\text{CBPA–WSFME (at 25 °C)}} = \frac{43.38}{49.38}$$

$$\rho_{\text{CBPA–WSFME (at 25 °C)}} = 0.878 \ \frac{g}{cm^3}$$

$$\rho_{\text{Water (at 25 °C)}} = 0.997 \ \frac{g}{cm^3}$$

- *Specific gravity (SG) of CBPA- WSFME at 25* °C

$$SG_{\text{CBPA–WSFME(at 25 °C)}} = \frac{\rho_{\text{CBPA–WSFME(at 25 °C)}}}{\rho_{\text{Water (at 25 °C)}}}$$

$$SG_{\text{CBPA–WSFME(at 25 °C)}} = \frac{0.878}{0.997}$$

$$SG_{\text{CBPA–WSFME(at 25 °C)}} = 0.881$$

- *Density of CBPA-WSFME at 15* °C

$$\rho_{\text{CBPA–WSFME (at 15 °C)}} = \frac{m_{\text{CBPA–WSFME}}}{V_{\text{CBPA–WSFME}}}$$

$$\rho_{\text{CBPA–WSFME (at 15 ℃)}} = \frac{43.53}{49.35}$$

$$\rho_{\text{CBPA–WSFME (at 15 ℃)}} = 0.882 \ \frac{\text{g}}{\text{cm}^3}$$

$$\rho_{\text{Water (at 15 ℃)}} = 0.999 \ \frac{\text{g}}{\text{cm}^3}$$

- *Specific gravity (SG) of CBPA- WSFME at 15* ℃

$$\text{SG}_{\text{CBPA–WSFME(at 15 ℃)}} = \frac{\rho_{\text{CBPA–WSFME(at 15 ℃)}}}{\rho_{\text{Water (at 15 ℃)}}}$$

$$\text{SG}_{\text{CBPA–WSFME(at 15 ℃)}} = \frac{0.882}{0.999}$$

$$\text{SG}_{\text{CBPA–WSFME(at 15 ℃)}} = 0.883$$

12. Calculating the API of CBPA-WSFME for phase 1

$$\text{API} = \left(\frac{141.5}{\text{specific gravity at 15℃}}\right) - 131.15$$

$$\text{SG of WSFME (CBPA)at } 15℃ = 0.883$$

$$\text{API} = \left(\frac{141.5}{0.883}\right) - 131.15$$

$$\text{API} = 29.10$$

13. Calculating the kinematic viscosity at 40°C of CBPA-WSFME for phase 1

- *Calibration calculations*

$$\text{V}_{\text{distilled water (at 40 ℃)}} = \frac{\text{m}_{\text{distilled water (at 40 ℃)}}}{\rho_{\text{distilled water (at 40 ℃)}}}$$

$$\text{V}_{\text{distilled water (at 40 ℃)}} = \frac{10.1}{0.992} = 10.18 \text{ mL}$$

$$\text{V}_{\text{CBPA–WSFME (at 40 ℃)}} = \text{V}_{\text{distilled water (at 40 ℃)}}$$

- *Density of CBPA-WSFME at 40* ℃

$$\rho_{\text{CBPA-WSFME (at 40 ℃)}} = \frac{m_{\text{CBPA-WSFME}}}{V_{\text{CBPA-WSFME}}}$$

$$\rho_{\text{CBPA-WSFME (at 40 ℃)}} = \frac{8.87}{10.18}$$

$$\rho_{\text{CBPA-WSFME (at 40 ℃)}} = 0.8714 \ \frac{g}{cm^3}$$

$$\rho_{\text{CBPA-WSFME (at 40 ℃)}} = 871.4 \ \frac{kg}{m^3}$$

$$\text{dynamic viscosity}_{\text{CBPA-WSFME (at 40 ℃)}} = 0.003 \text{ Pa.s}$$ *(Refer to Table A15)*

- *Kinematic viscosity of CBPA-WSFME at 40* ℃

$$\text{kinematic viscosity}_{\text{CBPA-WSFME (at 40 ℃)}} = \frac{\text{dynamic viscosity}_{\text{CBPA-WSFME (at 40 ℃)}}}{\rho_{\text{CBPA-WSFME (at 40 ℃)}}}$$

$$\text{kinematic viscosity}_{\text{CBPA-WSFME (at 40 ℃)}} = \frac{0.003}{871.4}$$

$$\text{kinematic viscosity}_{\text{CBPA-WSFME (at 40 ℃)}} = 3.59 \times 10^{-6} \ \frac{m^2}{s}$$

$$\text{kinematic viscosity}_{\text{CBPA-WSFME (at 40 ℃)}} = 3.59 \ \frac{mm^2}{s}$$

14. Quantities used for the continuous transesterification reaction (phase 2)

- Calculating the volume of EWSFO to be used in the continuous transesterification reaction

Mass of EWSFO

From Stoichiometry it is known that:

$$\text{Number of moles of EWSFO } (n_{EWSFO}) = 1 \text{ mole}$$

$$m_{EWSFO} = \text{number of moles of EWSFO } (n_{EWSFO}) \text{ x molar mass of EWSFO } (Mr_{EWSFO})$$

$$m_{EWSFO} = 1 \times 279.67$$

$$m_{EWSFO} = 279.67 \text{ g}$$

Volume of EWSFO

$$\text{Volume of EWSFO} = \frac{\text{Mass of EWSFO } (m_{EWSFO})}{\text{Density of EWSFO } (\rho_{EWSFO})}$$

$$\text{Volume of EWSFO} = \frac{279.67}{0.902}$$

$$\text{Volume of EWSFO} = 309.93 \text{ cm}^3$$

- Calculating the volume of methanol (MeOH) and the volume of n-hexane to be used in the continuous transesterification reaction

Given that:

$$\text{Density of MeOH } (\rho_{MeoH}) = 0.791 \frac{g}{cm^3}$$

$$\text{Density of n} - \text{hexane } (\rho_{n-hexane}) = 0.66 \frac{g}{cm^3}$$

The following conditions were used for the phase 2 reaction: 0.9 volume ratio of MeOH to EWSFO and 0.5 weight ratio of n-hexane to EWSFO (Ren et al., 2012).

Volume of Methanol

$$\text{Volume of MeOH} = \text{volume ratio of MeOH to EWSFO} \times \text{Volume of EWSFO}$$

$$\text{Volume of MeOH} = 0.9 \times 309.93$$

$$\text{Volume of MeOH} = 278.93 \text{ cm}^3$$

Mass of methanol

$$m_{MeOH} = \text{Volume of MeOH } (v_{MeOH}) \times \text{Density of MeOH } (\rho_{MeOH})$$

$$m_{MeOH} = 278.93 \times 0.791$$

$$m_{MeOH} = 220.72 \text{ g}$$

Mass of n-hexane

$$m_{n-hexane} = \text{weight ratio of n} - \text{hexane to EWSFO} \times \text{Mass of EWSFO}$$

$$m_{n-hexane} = 0.5 \times 279.67$$

$$m_{n-hexane} = 139.84 \text{ g}$$

Volume of n-hexane

$$\text{Volume of n} - \text{hexane} = \frac{\text{mass of n} - \text{hexane}}{\text{Density n} - \text{hexane}}$$

$$\text{Volume of n} - \text{hexane} = \frac{139.84}{0.66}$$

$$\text{Volume of n} - \text{hexane} = 211.87 \text{ g}$$

NB: Due to size of the feedstock tank, which had a working volume of 1.3 L, the quantities of EWSFO, methanol and n-hexane were all increased, i.e. multiplied by a factor of 1.6.

Thus, the used quantities were as follows:

$$\text{Volume of EWSFO} = 495.88 \text{ cm}^3$$
$$\text{Volume of MeOH} = 446.30 \text{ cm}^3$$
$$\text{Volume of n} - \text{hexane} = 338.99 \text{ cm}^3$$

15. Calculating the density of the CECPHA-Pumice

From Appendix A (Table A.18) it is known that:

$$\text{Mass of CECPHA} - \text{Pumice } (m_{CECPHA-Pumice}) = 1.013 \text{ g}$$
$$\text{Volume of CECPHA} - \text{Pumice } (v_{CECPHA-Pumice}) = 0.77 \text{ cm}^3$$

$$\rho_{CECPHA-Pumice} = \frac{m_{CECPHA-Pumice}}{v_{CECPHA-Pumice}}$$

$$\rho_{CECPHA-Pumice} = \frac{1.013 \text{ g}}{0.77 \text{ cm}^3}$$

$$\rho_{CECPHA-Pumice} = 1.32 \text{ g.cm}^{-3}$$

16. Calculating the flowrate

Given that:

$$\text{Mass of CECPHA} - \text{Pumice } (m_{CECPHA-Pumice}) \text{packed in the reactor} = 253 \text{ g}$$
$$\text{Density of CECPHA} - \text{Pumice } (\rho_{CECPHA-Pumice}) = 1.32 \text{ g.cm}^{-3}$$

Residence time (RT) $= 2$ hrs $= 120$ min

$$\text{Flow rate } (Q) = \frac{m_{CECPHA-Pumice}}{\rho_{CECPHA-Pumice} \times RT}$$

$$Q = \frac{253}{1.32 \times 120}$$

$$Q = 1.6 \text{ mL/min}$$

17. Calculating the initial concentration of triglycerides (C_{TGi}) in EWSFO

Mass of EWSFO in the feedstock tank (m_{EWSFO}) $= 447.29$ g
Total volume of reactants in the feedstock tank (V_{TFT}) $= 1.281$ L
Molar mass of EWSFO (Mr_{EWSFO}) $= 279.67 \text{ g.mol}^{-1}$
Initial mass fraction of TG in EWSFO(MF_{TGi}) $= 0.762$

$$\text{Initial molar concentration of TG in EWSFO } (C_{TGi}) = \left(\frac{\frac{m_{EWSFO}}{V_{TFT}}}{Mr_{EWSFO}}\right) \times MF_{TGi}$$

$$\text{Initial molar concentration of TG in EWSFO } (C_{TGi}) = \left(\frac{\frac{447.29}{1.281}}{279.67}\right) \times 0.762$$

$$\text{Initial molar concentration of TG in EWSFO } (C_{TGi}) = 0.951 \frac{\text{mol}}{\text{L}}$$

18. Calculating initial rate of reaction (r_o)

Given that:

Mass of $CECPHA - Pumice$ ($m_{CECPHA-Pumice}$)packed in the reactor $= 253$ g
feed flow rate (v_o) $= 0.0016 \text{ L.min}^{-1}$
Initial molar concentration of TG in EWSFO (C_{Wi}) $= 0.951 \text{ mol. L}^{-1}$

Data from GC graph
Conversion (x) = 0.78

$$-r'_o = \frac{v_o \times c_{Wi} \times x}{\Delta W}$$

$$-r'_o = \frac{0.0016 \times 0.951 \times 0.78}{253}$$

$$-r'_o = 4.69 \times 10^{-6} \text{ mol/min.g}$$

19. Determination of the activation energy (E_a)

From the equation of the straight line in the Arrhenius plot illustrated in Figure 5.2 the following values were obtained:

$$y = -2796.2\,x - 1.9057$$

$-\frac{E_a}{R} = -2796.2$ (Slope)

$\ln A = -1.9057$ (Intercept)

$A = e^{-1.9057} = 0.149$ mol/L.min

Given that: R= 8.314 J/mol.K

$$E_a = -\frac{E_a}{R} \times R$$

$$E_a = -2796.2 \times 8.314$$

$$E_a = 23247.61 \text{ J/mol}$$

$$E_a = 23.247 \text{ kJ/mol}$$

Appendix C: Gas Chromatography graphs

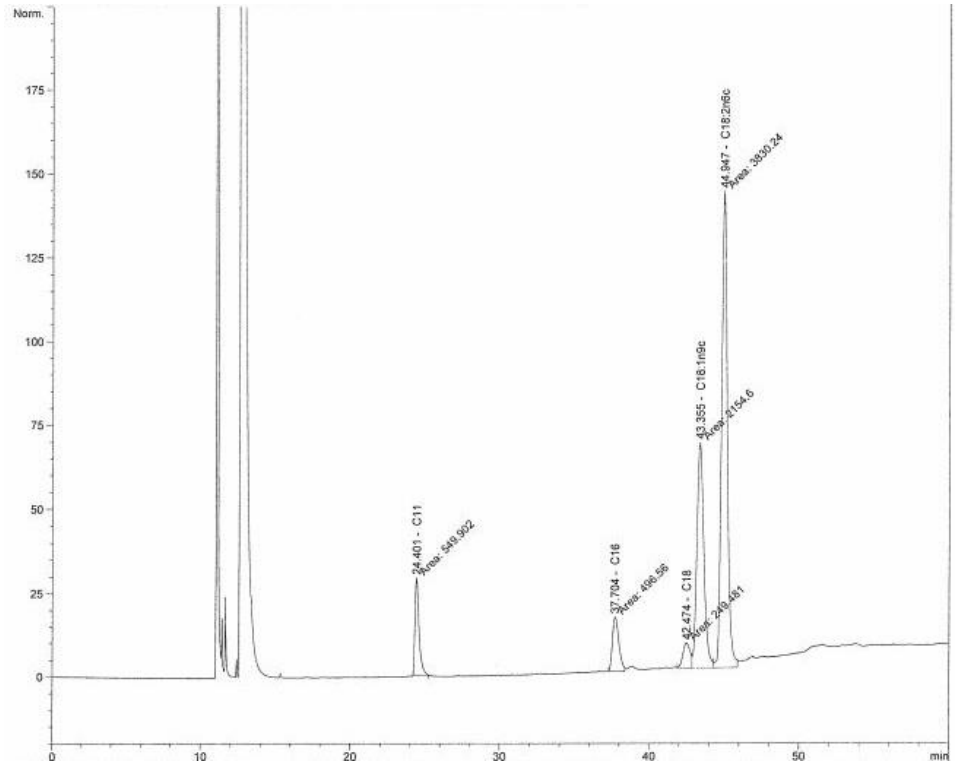

Figure C1: Chromatograph of WSFO

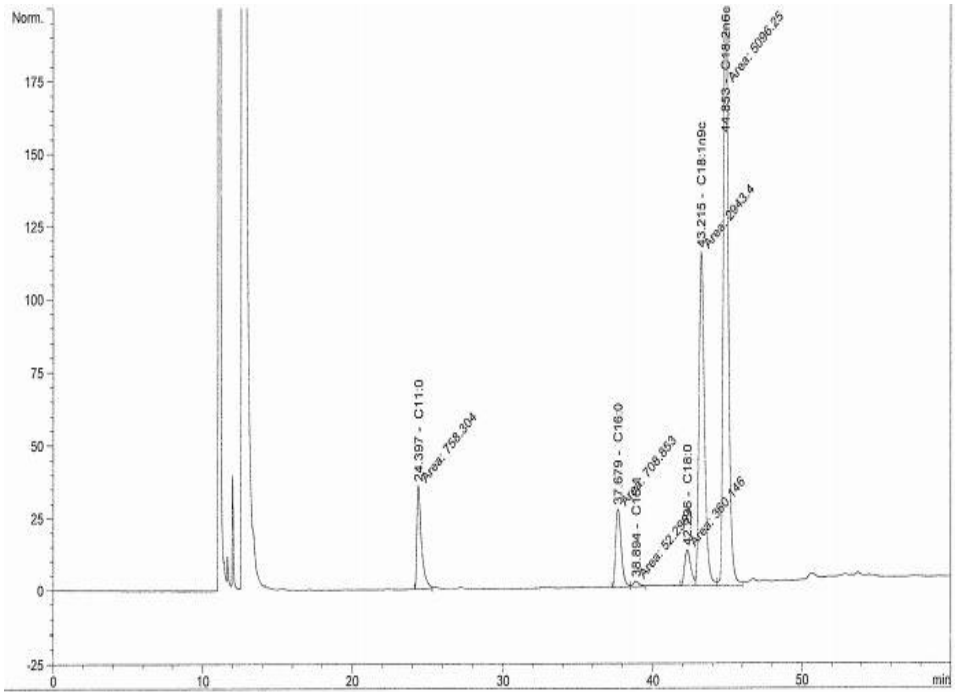

Figure C2: Chromatograph of EWSFO

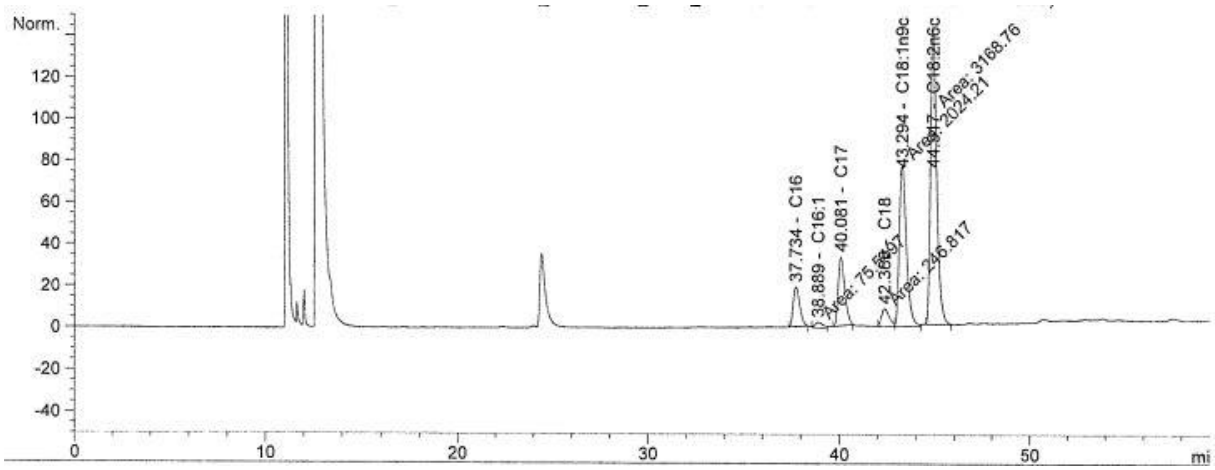

Figure C3: Chromatograph of WSFME withdrawn at 30 minutes of residence time (for 1.6 mL/min, 40°C)

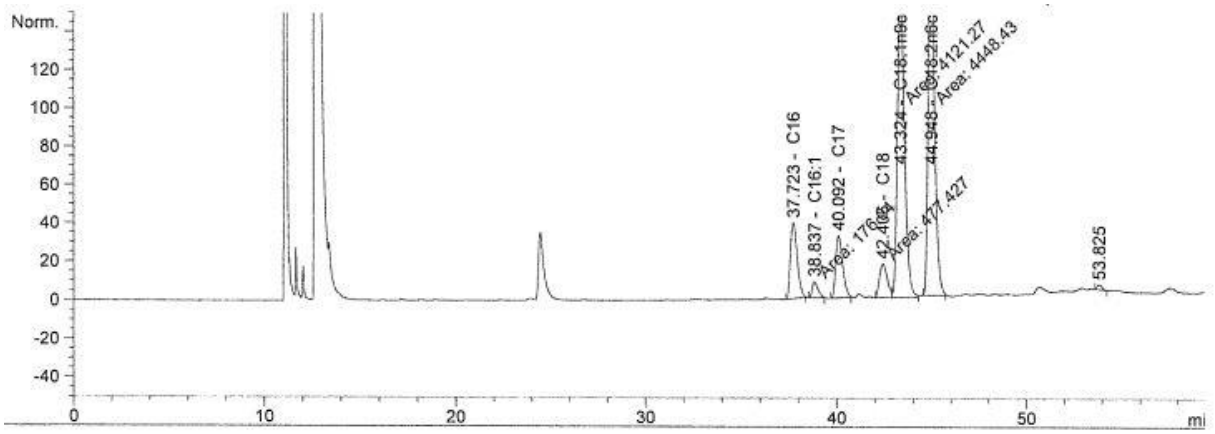

Figure C4: Chromatograph of WSFME withdrawn at 60 minutes of residence time (for 1.6 mL/min, 40°C)

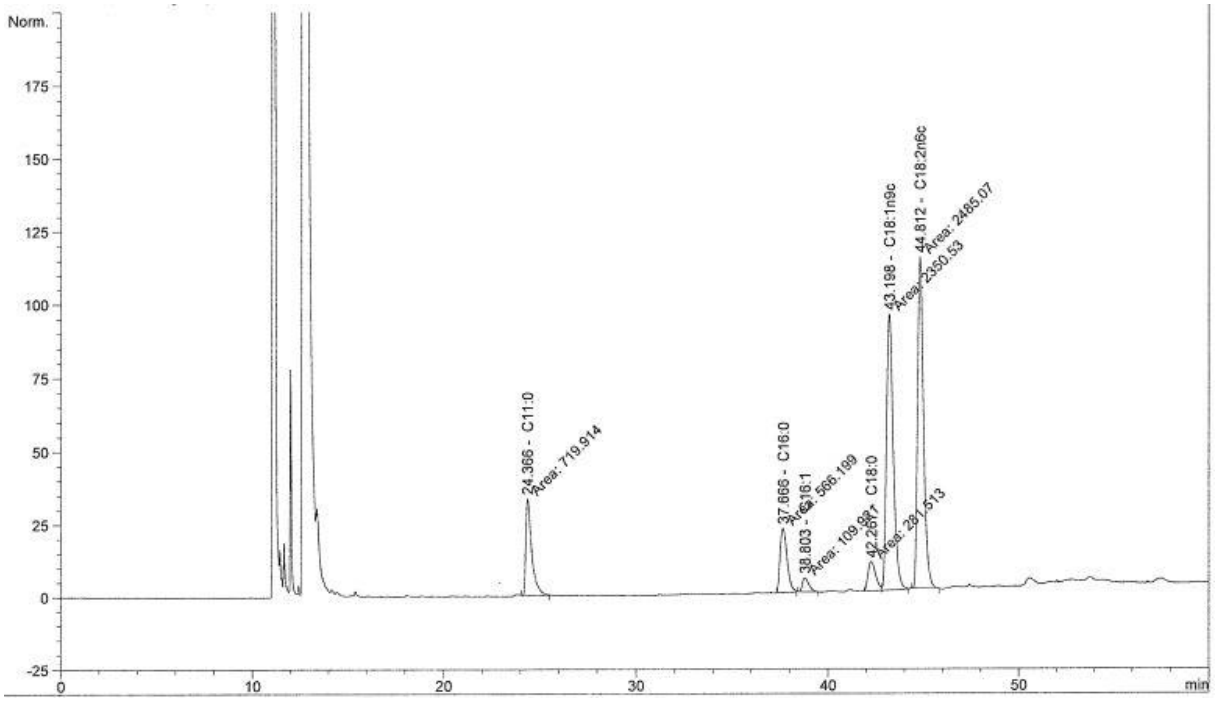

Figure C5: Chromatograph of WSFME withdrawn at 90 minutes of residence time (for 1.6 mL/min, 40°C)

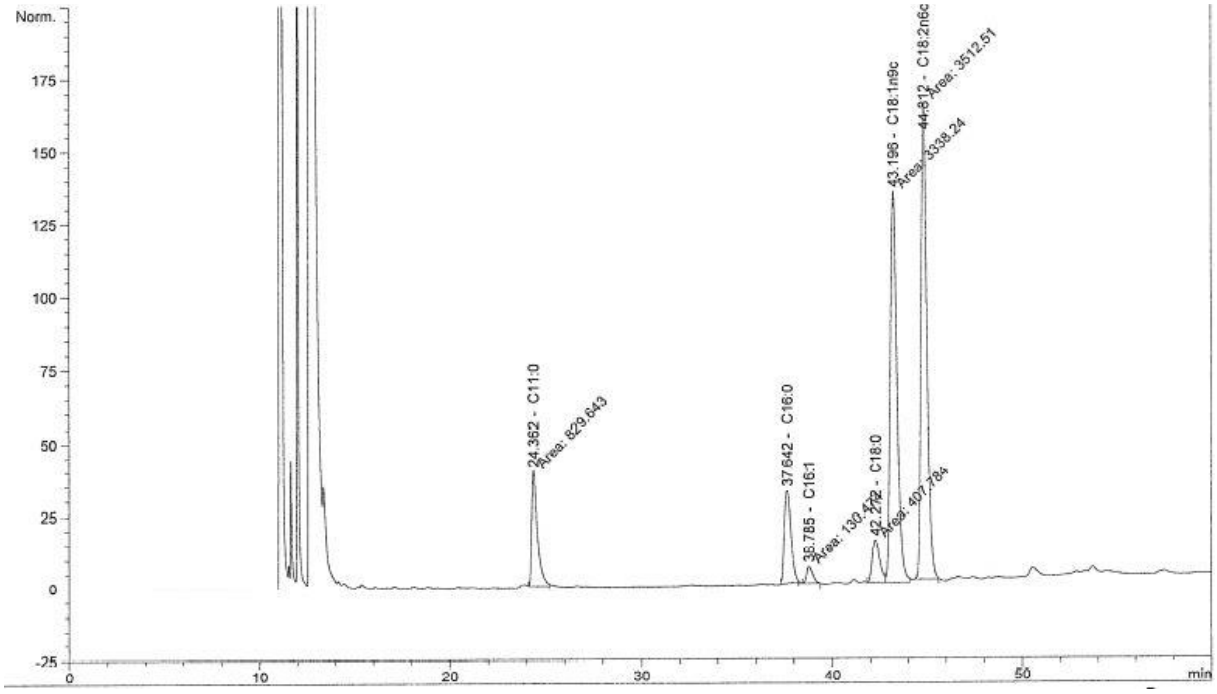

Figure C6: Chromatograph of WSFME withdrawn at 120 minutes of residence time (for 1.6 mL/min, 40°C)

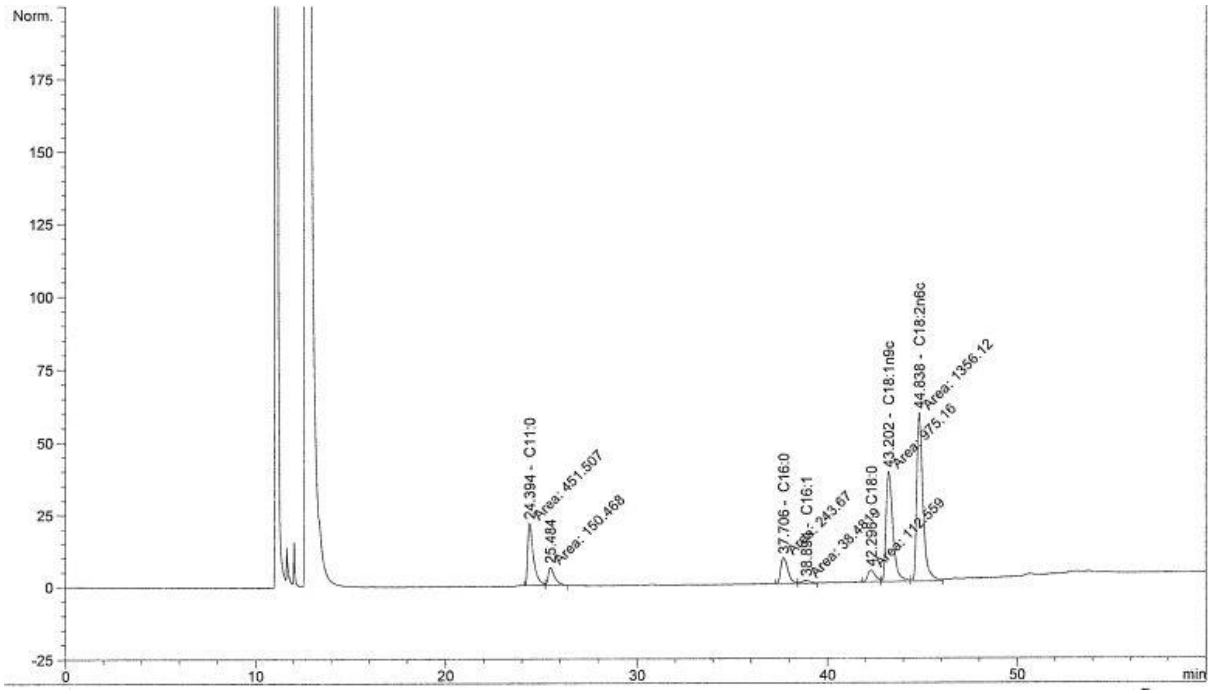

Figure C7: Chromatograph of WSFME withdrawn at 30 minutes of residence time (for 1.6 mL/min, 50°C)

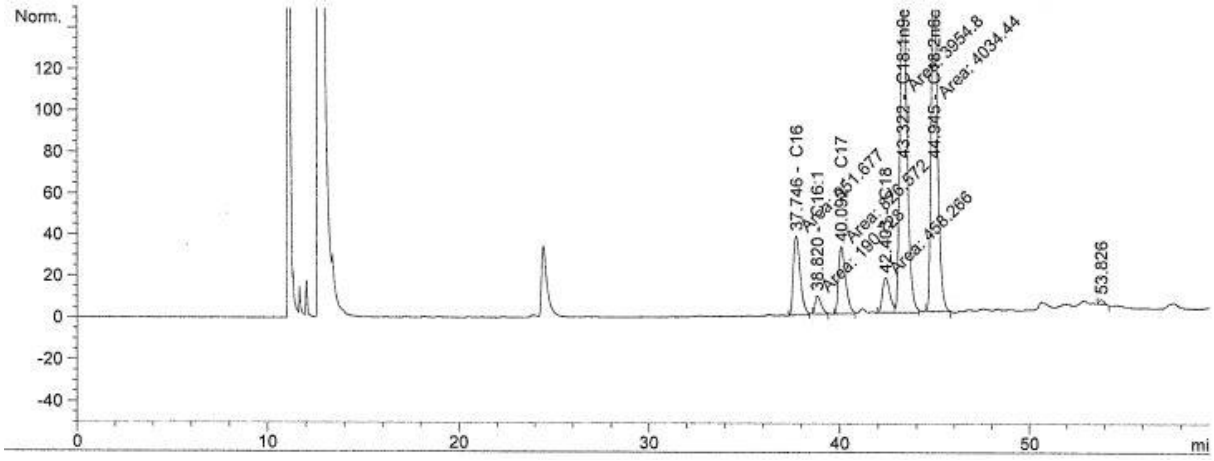

Figure C8: Chromatograph of WSFME withdrawn at 60 minutes of residence time (for 1.6 mL/min, 50°C)

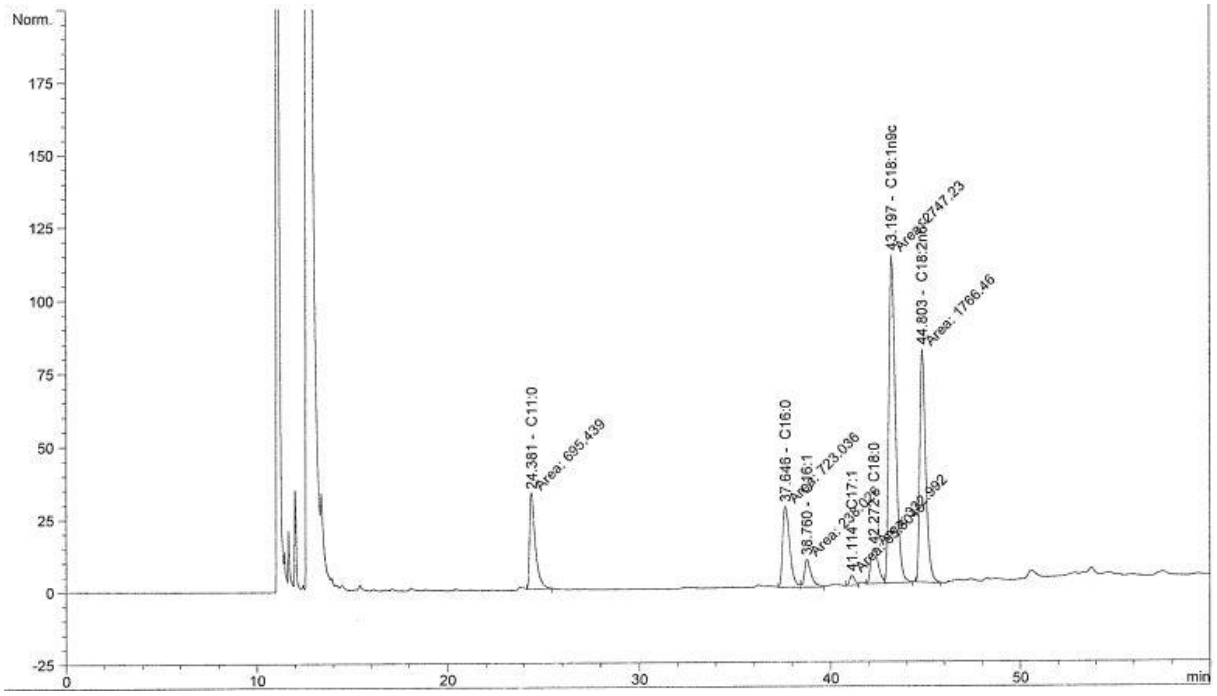

Figure C9: Chromatograph of WSFME withdrawn at 90 minutes of residence time (for 1.6 mL/min, 50°C)

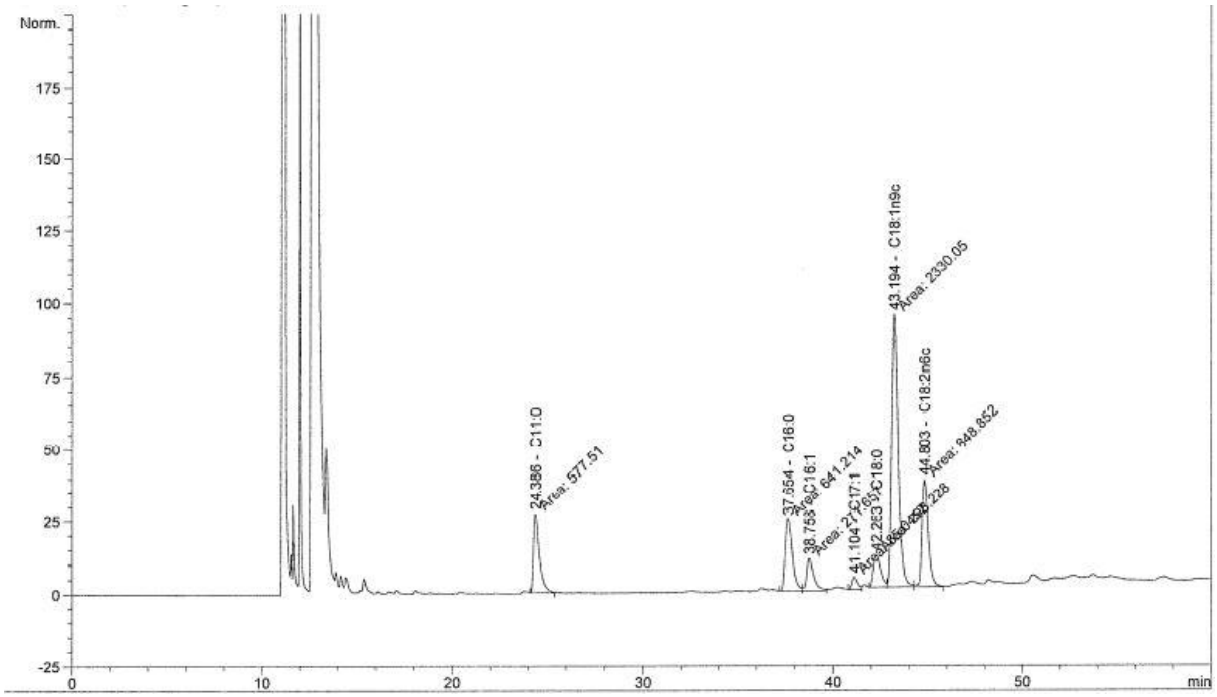

Figure C10: Chromatograph of WSFME withdrawn at 120 minutes of residence time (for 1.6 mL/min, 50°C)

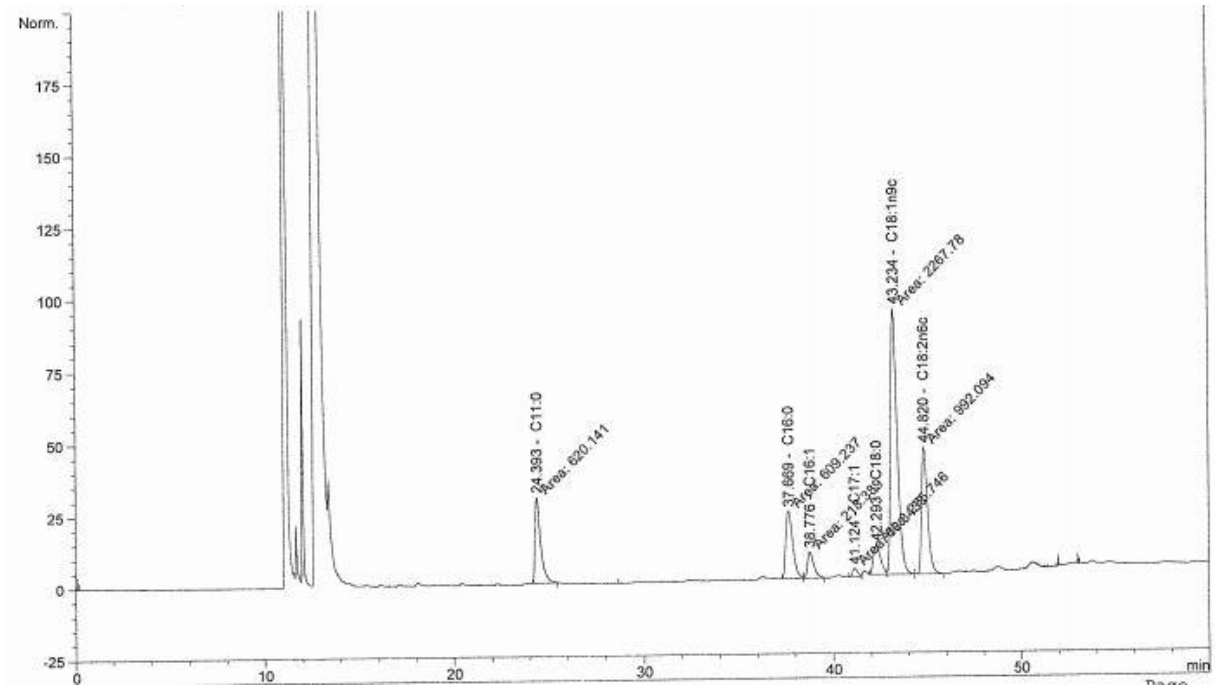

Figure C11: Chromatograph of WSFME withdrawn at 30 minutes of residence time (for 4 mL/min, 55°C)

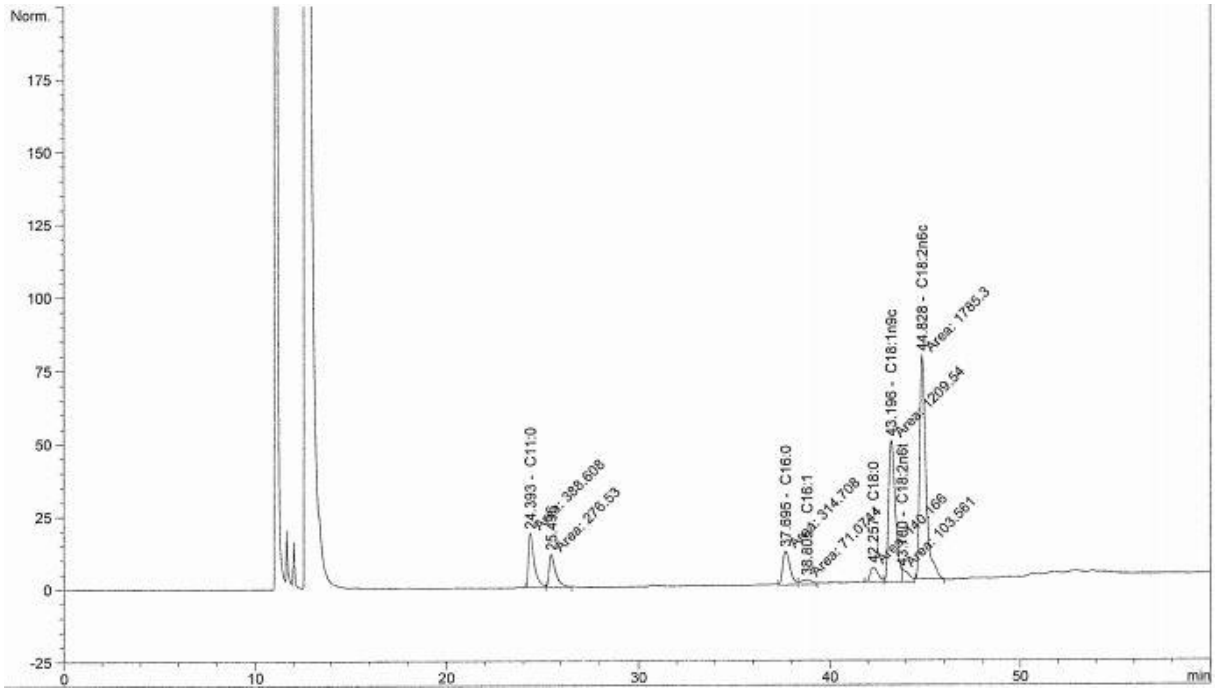

Figure C12: Chromatograph of WSFME withdrawn at 45 minutes of residence time (for 3 mL/min, 55°C)

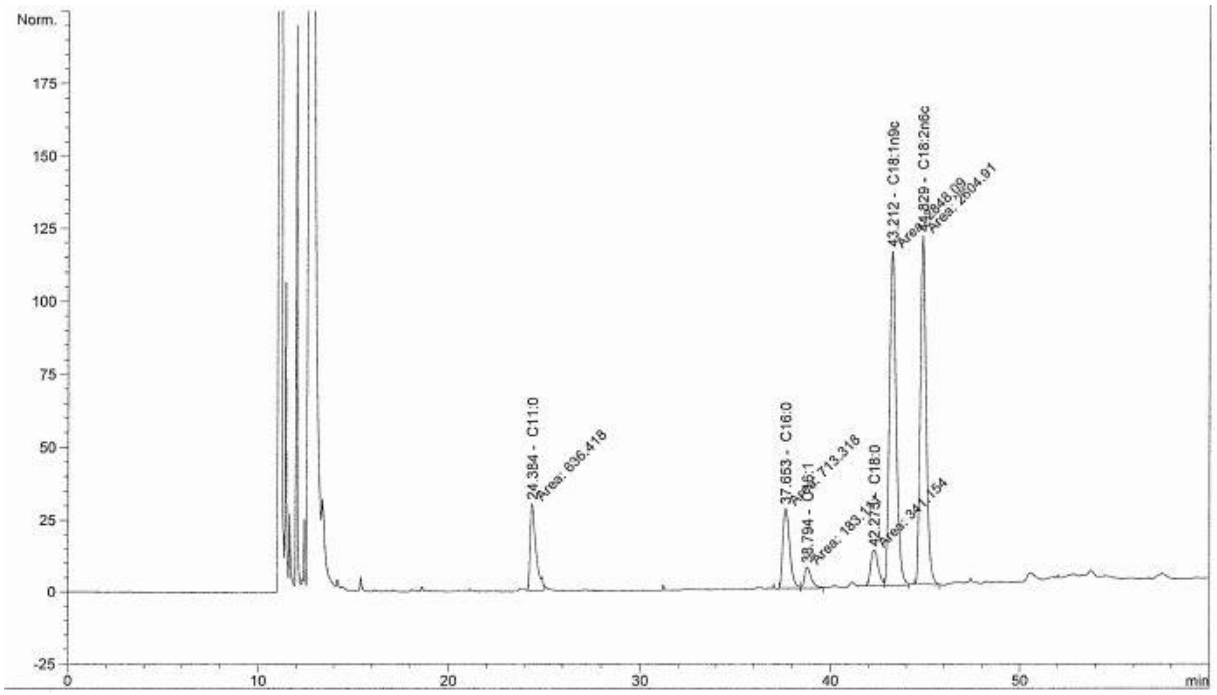

Figure C13: Chromatograph of WSFME withdrawn at 90 minutes of residence time (for 1.6 mL/min, 55°C)

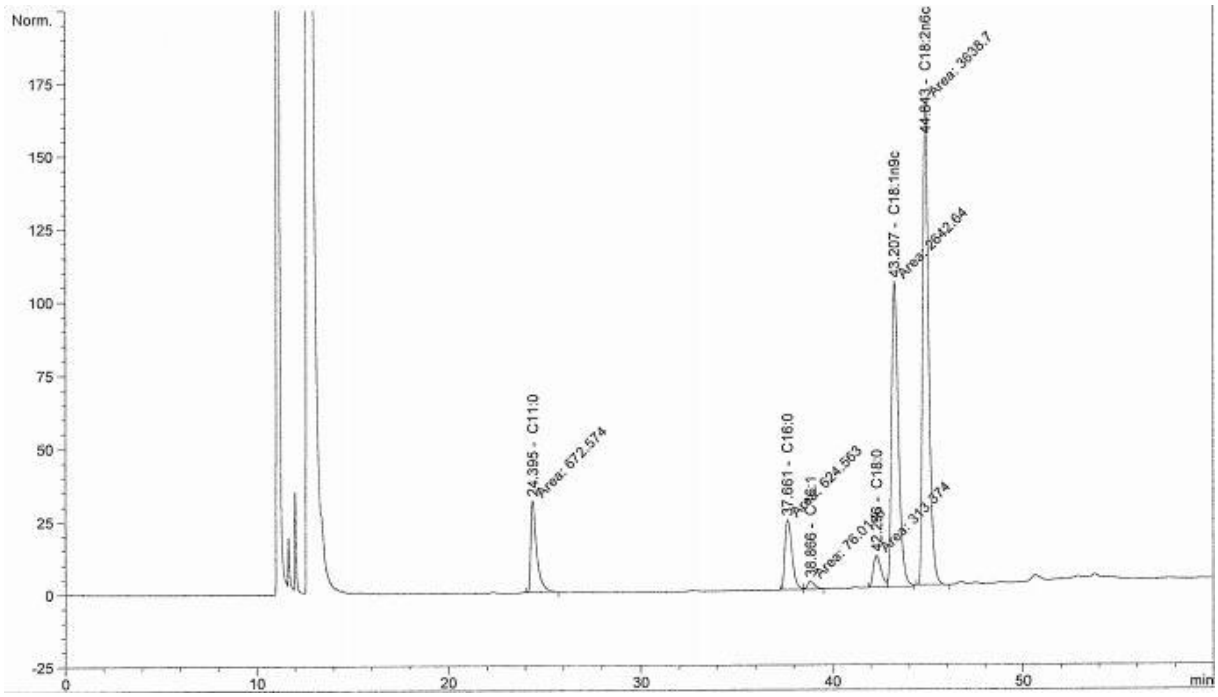

Figure C14: Chromatograph of WSFME withdrawn at 90 minutes of residence time (for 2.1 mL/min, 55°C)

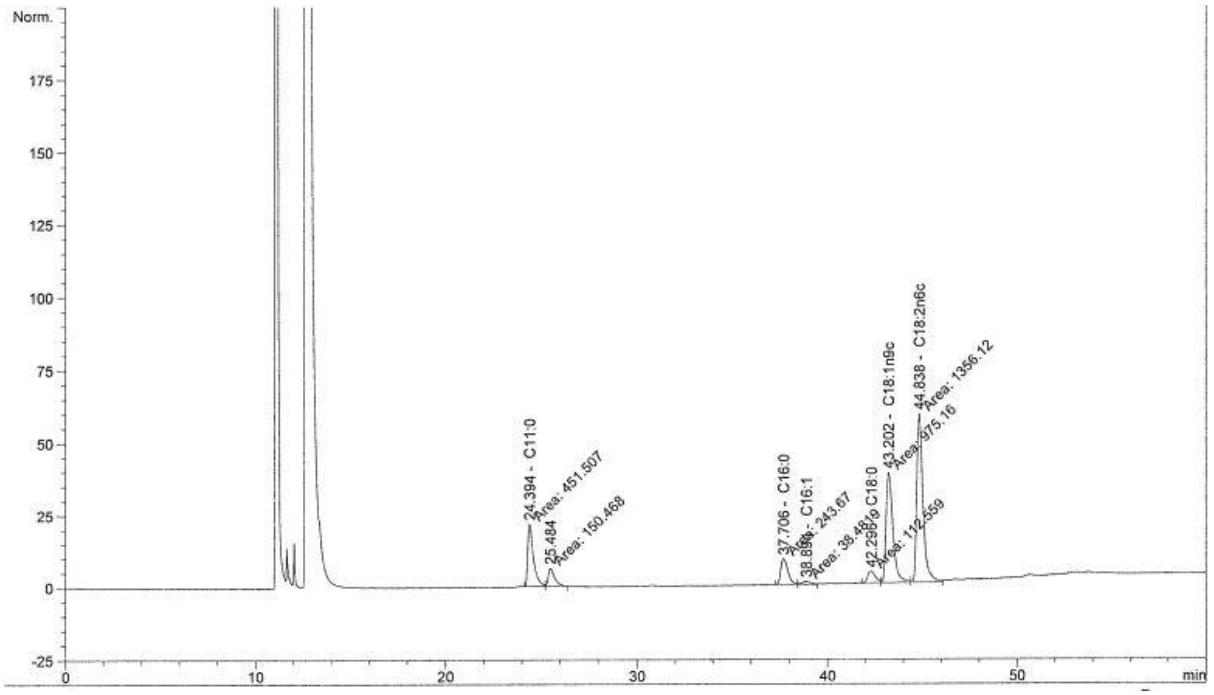

Figure C15: Chromatograph of WSFME withdrawn at 30 minutes of residence time (for 1.6 mL/min, 60°C)

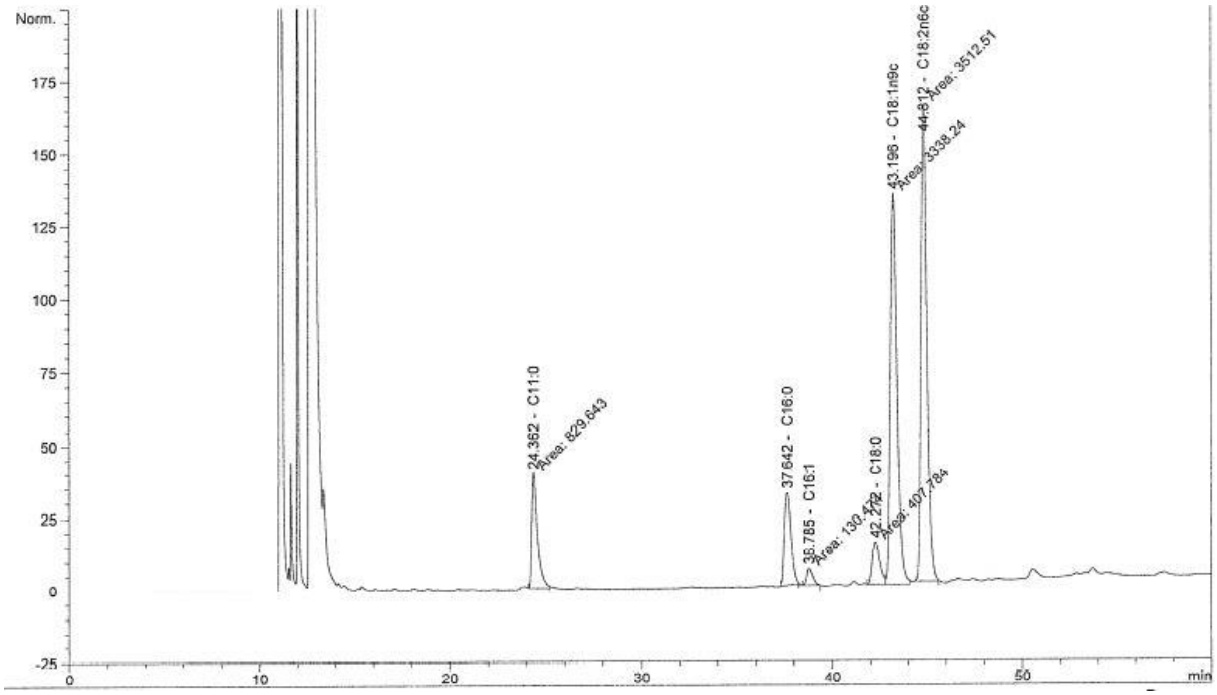

Figure C16: Chromatograph of WSFME withdrawn at 60 minutes of residence time (for 1.6 mL/min, 60°C)

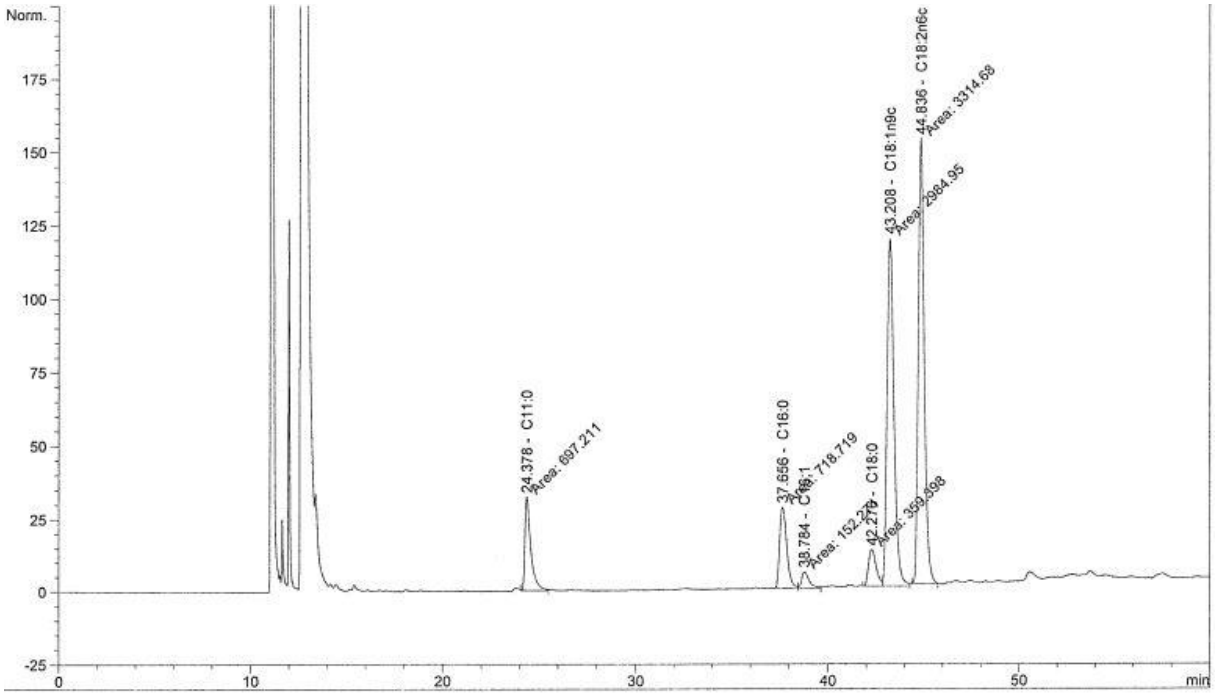

Figure C17: Chromatograph of WSFME withdrawn at 90 minutes of residence time (for 1.6 mL/min, 60°C)

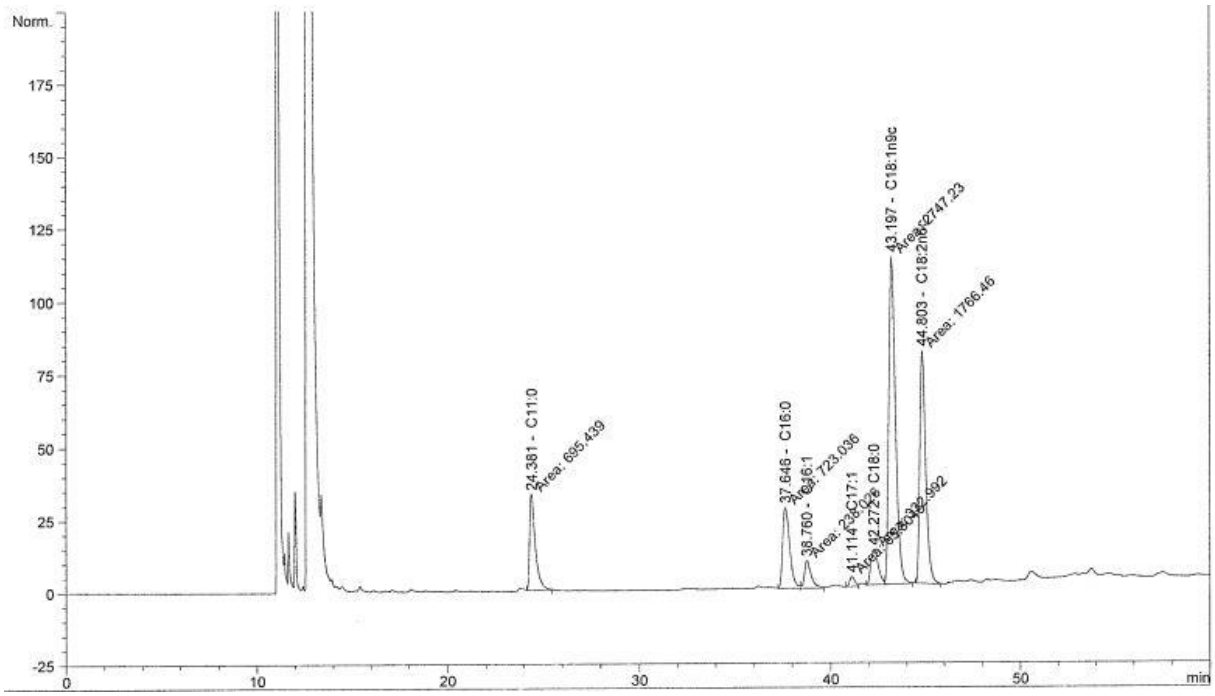

Figure C18: Chromatograph of WSFME withdrawn at 120 minutes of residence time (for 1.6 mL/min, 60°C)